INTEGRATING TRAPPED NEUTRAL ATOMS WITH NANOPHOTONIC RESONATORS FOR A NOVEL QUANTUM SIMULATOR

by

Brian Fields

A Dissertation

Submitted to the Faculty of Purdue University

In Partial Fulfillment of the Requirements for the degree of

Doctor of Philosophy

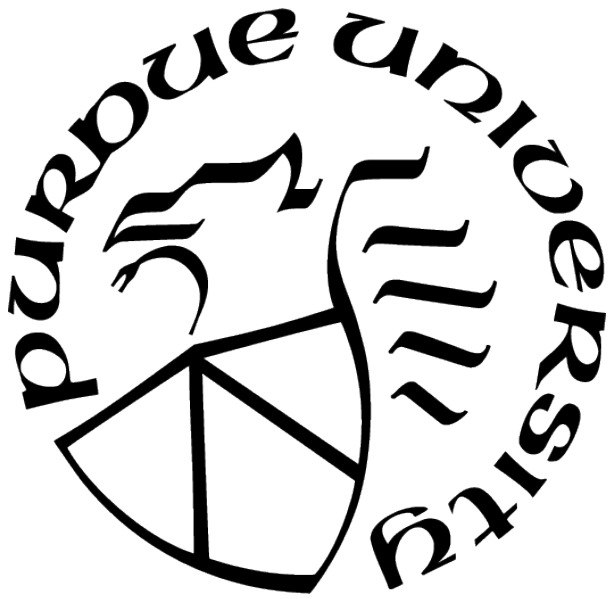

Department of Physics and Astronomy

West Lafayette, Indiana

May 2021

THE PURDUE UNIVERSITY GRADUATE SCHOOL
STATEMENT OF COMMITTEE APPROVAL

Dr. Chen-Lung Hung, Chair

School of Physics

Dr. Gabor Csathy

School of Physics

Dr. Tongcang Li

School of Physics

Dr. Qi Zhou

School of Physics

Approved by:

Dr. John Finley

To My Family

The work presented in this thesis has been a collaborative effort that could not even be imagined with out the hard work of my colleagues over the last few years, I would like to thank all of them for their contributions though out my time at Purdue. I would like to begin by thanking my advisor, Professor Chen-Lung Hung, for taking me on as a student. I joined about a year and a half after Chen-Lung had arrived at Purdue. During the first year whilst the lab was being renovated he worked day and night preparing the initial optical setups for our laser systems on breadboard to be ready to move in as soon as the lab was ready. Throughout the last few years he has challenged and pushed me to grow more than any mentor I have ever had.

I would like to thank my fellow graduate student Cheng-An Chen who helped a great deal with the initial chamber design and many others tasks as well before moving on to start his own experiment. Cheng-An is an incredibly talented experimentalist who has always made himself available to others in our lab as problems arise even when they are unrelated to his own project.

I would like to thank May E. Kim, a former postdoc on our experiment who working with Chen-Lung got our experiment off the ground, helping construct the apparatus and achieve several of our projects initial milestones. May is an excellent researcher and I learned a great amount from our time working together.

I would like to thank my fellow graduate student Tzu-Han Chang. The atom trapping machine is only half of our project, the other key element being the photonic chips which have been designed and built from the ground up by Tzu-Han Chang. It is hard to understate how essential Tzu-Han has been to this project, the high level fabrication techniques and recipes would be essentially impossible to develop in a traditional AMO lab without someone of his talent and background. He has worked tirelessly to iteratively improve our photonic chip design and fabrication processes and tackled a multitude of unforeseen problems that arose as our project advanced.

I would also like to thank my colleagues who have overtaken the project, graduate student Xinchao Zhou and our new postdoc Hikaru Tamura. Xinchao is a very smart, dedicated hard worker who has brought tremendous energy into our lab. Hikaru has a wealth of experience in atom tweezer experiments and brings many new ideas that will further our project in the days to come.

Last I would like to especially thank my high school physics instructor Chris Hahn. Chris is beyond a doubt the most talented, engaging teacher I have ever met at any level of study. As I spent time as a TA during my grad school career, whenever I felt that I gave a particularly good lecture and went to pat myself on the back, I'd remind myself that by that time of the day Chris had probably given four even better lectures, with a new one planned every day of the week, and on top of that he was working with novice students with no background knowledge to rely upon. Chris empowered his students to think as individuals and abandon any memorize then repeat strategies that might get one by in a different field of study. The greatest gift I received from Chris was not the knowledge of physics he taught us but the ability to think critically itself and challenge ideas you do not understand.

TABLE OF CONTENTS

LIST OF TABLES 9

LIST OF FIGURES 10

ABSTRACT 12

1 INTRODUCTION 13

2 BACKGROUND 16

2.1 Optical Cavity 16

2.2 Micro-Ring Resonators 18

2.3 Jaynes-Cummings Model 25

2.4 Doppler Cooling 28

2.5 Polarization Gradient Cooling 30

2.6 Magneto-Optical Trap (MOT) 31

2.7 Optical Dipole Traps 33

2.8 Raman Transitions 35

2.8.1 Raman Transitions in a Λ System 36

2.8.2 Raman Cooling 38

3 APPARATUS 40

3.1 Lasers 40

3.1.1 D1 40

3.1.2 D2 44

3.1.3 Tweezer Beam 47

3.2 Vacuum Chamber 48

3.2.1 Source Chamber 49

3.2.2 Science Chamber 50

3.2.3 Load Lock Chamber 53

3.3 Chip Transfer Procedure 53

3.3.1 Preparation . . . 54
3.3.2 Pincer Loading . . . 57
3.3.3 Chip Loading and Retrieval . . . 59
3.4 MOT . . . 61
3.5 Imaging . . . 64
3.5.1 Absorption Imaging . . . 64
3.5.2 Fluorescent Imaging . . . 65
3.6 Microwaves . . . 66
3.7 Magnetic Field Control . . . 67
3.7.1 Helmholtz Coils . . . 67
3.7.2 Coil Driver Circuit . . . 69

4 TRAPPING AND IMAGING INDIVIDUAL ATOMS ON TOP OF A NANOPHOTONIC CIRCUIT . . . 78
4.1 Introduction . . . 78
4.2 Loading Atoms on Top of a Nano-Photonic Structure . . . 79
4.3 Florescence Imaging . . . 84
4.4 Improving Loading Probability with Introduction of 'Bottom' Dipole Beam . . . 86
4.5 Monte-Carlo Simulations of Trap Loading Probabilities . . . 88
4.6 Optical conveyor belt . . . 91

5 LOADING ATOMS ON TOP OF A NANOPHOTONIC CIRCUIT VIA A 7 TWEEZER ARRAY WITH HIGH PROBABILITY . . . 97
5.1 Background and Cross-talk . . . 99
5.2 Single Tweezer - No Neighbor . . . 103
5.3 Loading 7 Tweezer Array . . . 105

6 ATOM-CAVITY COUPLING . . . 110
6.1 Probing atom-waveguide coupling . . . 115

7 CURRENT AND FUTURE WORKS . . . 120
7.1 Current Work Probing Atom-Cavity Coupling . . . 120

7.2 Evanescent Trapping Scheme 121
7.3 Spin Exchange 125
7.4 CNOT Gate 128
7.5 Conclusion 132

REFERENCES 133

LIST OF TABLES

5.1 Fit parameters for backgound measurements 102
7.1 State map for composite CNOT operation. 129
7.2 State map for control Z operation 131

LIST OF FIGURES

2.1 Fabry-Perot Optical Cavity . . . 17
2.2 Photonic chip . . . 21
2.3 Micro-Ring resonator . . . 23
2.4 Frequency tuning of micro-ring resonance via 1064nm heating laser . . . 24
2.5 James-Cummings model . . . 26
2.6 Polarization gradient cooling schematic . . . 30
2.7 Magneto optical trap (MOT) . . . 32
2.8 Dipole Trap . . . 33
2.9 Raman transition for an atomic lambda system . . . 36
3.1 Energy level diagram for Cesium's D1 transition . . . 41
3.2 D1 Laser setup . . . 42
3.3 Polarization spectroscopy lock . . . 43
3.4 D2 Laser setup . . . 44
3.5 D2 energy level diagram . . . 45
3.6 Solidworks rendering of vacuum chamber . . . 49
3.7 Science Chamber Experimental Schematic . . . 51
3.8 Chip transfer diagram . . . 54
3.9 Chip Loading . . . 56
3.10 Science chamber top view-port image of a successfully docked photonic chip . . . 61
3.11 Cloud transfer process from MOT to mini-mot . . . 62
3.12 Absorption imaging of mini-mot cloud above photonic chip . . . 63
3.13 Microwave scan of Cesium's hyperfine structure . . . 67
3.14 Coil driver circuit for MOT coils . . . 71
3.15 Magnetic field calibration . . . 73
3.16 Coil Driver Circuit Assembly . . . 74
4.1 Experimental schematic for trapping single atoms above a micro-ring resonator . . . 80
4.2 Tweezer lattice potential formed by interference with reflected beam . . . 83
4.3 Florescence imaging of a single trapped atom above micro-ring resonator . . . 85

4.4 Back Beam Potential . . . 87
4.5 Monte-Carlo simulation for atoms loading into tweezer lattice . . . 89
4.6 Simulated trajectories of atoms loading into tweezer lattice . . . 90
4.7 Probability distribution for loading into a specific tweezer lattice site from Monte-Carlo simulation . . . 91
4.8 Optical conveyor belt for atoms trapped in a tweezer lattice above a nanophotonic structure . . . 93
4.9 Conveyoring atoms in a tweezer array . . . 95
5.1 Experimental schematic for preparing arrays of tweezer lattices on top of the surface of a photonic chip . . . 98
5.2 Mean photon counts detected for background images in 7 tweezer array . . . 99
5.3 Background + cross-talk for 7 tweezer array . . . 100
5.4 Background photon counts histogram . . . 101
5.5 Photon detection counts for a single tweezer with it's neighboring tweezer turned off . . . 104
5.6 Atoms loading probabilistically into lattice sites for a 7 tweezer array ontop of a photonic chip . . . 106
5.7 Photon count histogram for each atoms loaded into each site in 7 tweezer array 107
5.8 Mean atom number loaded into each tweezer of array . . . 109
6.1 Probing station schematic for sending in and detecting single photons from micro-ring resonator . . . 111
6.2 Micro-ring transmission scans . . . 113
6.3 Example simulation of waveguide transmission spectrum for a bus waveguide critically coupled to a micro-ring resonator with and without an atom coupled to the resonator . . . 117
7.1 Two color evanescent trap . . . 122
7.2 Simulation of the evanescent trapping potential along direction of resonator waveguide . . . 124
7.3 Long range spin exchange between pairs of atoms coupled to a micro-ring resonator 126
7.4 Raman scheme for coherent spin exchange . . . 127
7.5 Energy level diagram for aphoton mediated ZZ interaction . . . 130

ABSTRACT

Atoms trapped in close proximity to optical resonators provides a powerful tool for exploring atom light interactions and their quantum applications. In this work I will describe the development of a neutral atom quantum simulator that implements trapped cesium atoms which have been localized via optical tweezers in close proximity to the surface of a micro-ring resonator fabricated on the surface of an optical chip. The small separation between the cavity and the atom allows for relatively large atom photon coupling strength g on the order of a few hundred MHz. Coupling multiple atoms to a common nanophotonic mode provides a channel through which atoms can exchange virtual photons for the study of long range spin exchange and other quantum many body models.

This platform has proven to be extremely versatile. We have thus far successfully demonstrated our ability to trap and image individual atoms directly above the surface of our photonic chips as well as the ability to extend trapping and imaging to arrays of tweezer traps which can be loaded with one or more atoms with high probability. Due to the simplified fabrication process of our planar geometry photonic chips we have been able to rapidly prototype and evolve our system to facilitate new and improved methods of trapping atoms near the surface of our nanophotonic structure. In the following I will discuss the development of our apparatus, our current progress observing signatures of atom-cavity coupling, and some of our future goals we are approaching.

1. INTRODUCTION

Quantum computing has become one of the most preeminent topics in modern physics. Originally suggested by Feynman [1] such a machine would encode information on quantum bits or qubits, enabling fundamentally different methods of operation than a classical computer. Taking advantage of quantum superposition and entanglement, quantum computers[2] [3] will offer inherently parallel computation capable of performing algorithms that are currently non-feasible with classical machines. Quantum computers offer promise in two directions; Universal Quantum computation[4][5] and in Quantum Simulation [4], but many experimental and technological challenges must be overcome to bring a large scale system to fruition.

In Universal Quantum computation algorithms are built up out of operations called quantum gates which act on subsets of qubits in a quantum register. It has been shown that single qubit rotations and a two qubit entangling gate can produce a universal set of quantum gates capable of performing any operation that a classical machine can perform[4]. While capable of performing any classical computation, after 25 years only a handful of quantum algorithms have been discovered that outperform their classical counterparts. Quantum simulation makes use of one well controlled system to emulate another and glean certain properties that may be too challenging to calculate outright on a classical machine. As noted in Feynman's original paper, and formalized by Lloyd [6], the problem of simulating quantum mechanical particle on a classical computer is inherently non scalable. Disregarding the operations required for a simulation, the register size or memory needed to just record the state of a quantum system scales exponentially with the number of degrees of freedom. A quantum computer on the other hand would only need 'n' qubits to simulate n quantum particles. To demonstrate how powerful this reduction can be, neglecting error correction, a quantum simulator with only 50 qubits could be capable of studying systems that push the limits of modern day supercomputers.

This thesis will be focusing on the experimental challenges facing quantum computation. While the potential applications of a quantum computer may be broad, the development of these device has been slow and fraught with difficulties. For comparison, the first 25 years of quantum computers has seen devices go from a single qubit to around 50 qubits in state of the art machines, modern computers equivalently started with around 1000 bits in the early 70's and within 25 years had grown to 10's of millions in the 1990's. Many physical platforms have been proposed for building a Quantum Computer and a few have found physical traction, such as trapped atomic ions [7][8], quantum dots [9][10], and superconducting qubits. [11] [12] . The commonly accepted requirements for such a machine were specified by DiVencenzo, known commonly as the DiVencenzo criteria [13]. A physical implementation of a quantum computer must provide: a scalable physical system with well characterized qubits, the ability to initialize the state of the qubits to a simple fiduciary state, a "universal" set of quantum gates, long coherence times relative to the native gate speed, and a qubit-specific measurement capability. While the previously mentioned systems have long established hardware specific means for satisfying several of these criteria, the most elusive remains finding an easily scalable system.

Our approach to developing a quantum computer will utilize neutral atoms coupled to nanophotonic resonators fabricated on a photonic-chip. Neutral alkali atom based platforms [14] [15] with qubits encoded in the hyper-fine ground state manifold have several promising characteristics for use as quantum computers. A plethora of established techniques can be drawn upon for trapping cooling, and manipulating the state of these atoms allowing for well isolated qubits with excellent coherence times. The problem neutral atoms face is their inherently weak interaction strength making it difficult for individual atoms to talk to one another, a few solutions are being explored, most noticeably using Rydberg excitations to induce large atomic dipole moments allowing for long range dipole-dipole interactions. We aim to engineer the method atoms interact with one another by trapping individual atoms in close proximity to nanophotonic structures, allowing for atom(s) to couple to nanophotonic

resonator modes.[16] [17]. Our design will make use of high Q micro-ring resonators fabricated on a planar silicon photonic-chips which can support the trapping of multiple atoms at a time, in extreme proximity to the resonator surface yielding very small resonator mode volumes and high atom-photon coopertivity.

Making use of the established cold atom toolkit, we will be able to trap, cool, manipulate, and perform in-situ state detection for atoms coupled to a nanophotonic device, satisfying several of the DiVencenzo criteria. With use of only a few external lasers we will be able to coherently drive spin exchange operations (H_{xx}) between spatially separated atoms coupled to a common resonator via photon meditated atom-atom interactions (PMAAI). This photonic interface is the core of our system and will provide a path towards studying long range many-body models such as quantum magnetism, but also holds promise for facilitating multiple nanophotonic devices with interconnecting waveguides. In the following I will develop some background knowledge necessary to understand how our system operates, provide an overview of apparatus, and describe our initial results and current progress.

2. BACKGROUND

Recently a great deal of interest has been focused on coupling quantum emitters eg neutral atoms and quantum dots, to nanophotonic structures [18] [19][20]. Such devices have applications in quantum computation[21], simulation, and networking [22] where flying (photonic) qubits are desirable for transferring quantum information between sites. In our work, we are developing an architecture where cold atoms will be localized in close proximity to the surface of a micro-ring resonator which has been fabricated on a planar geometry photonic-chip. We will make use of the enhanced light matter interactions in a CQED environment to perform photon mediated atom-atom interactions (PMAAI) providing a novel platform for quantum computation and simulation. In the following I will begin by providing a introduction into optical cavities and the design ideology for our photonic chips, a description how atoms interact with a single cavity mode, and provide some of the basics for trapping and cooling techniques that we will be using to interface atoms with our micro-ring resonators.

2.1 Optical Cavity

At the heart of our apparatus is the interface through which trapped atomic qubits can coherently communicate with one another, providing the multi-qubit operations necessary for quantum computing/simulation; all of the other equipment and techniques required for trapping, cooling, quantum state preparation and detection for individual atomic qubits has long been established and repeated in many many labs. While there are hundreds of vacuum components, lasers, optics, electronics and computer programs needing to operate in concert with one another just to will our atomic qubit into existence, it is in hindsight quite remarkable that the 'quantum hardware' needed for this communication interface can be provided by the simple optical cavity (or photonic resonator), a passive non-electronic device derived from classical optics.

In it's simplest form, an optical cavity can be built from two parallel mirrors separated by a distance L_c. Light entering the cavity from the backside of mirror one will travel to mirror two then reflect back forming a closed path. A resonance will occur for light when the round trip distance of the cavity L_c is equal to a half integer number of wavelengths, $nL_c = \lambda \mathrm{m}/2$, where n is the index of refraction for the cavity medium. Under this condition light entering the cavity through mirror 1 will be in phase with light that completes a round trip through the cavity and interfere constructively resulting in the beam being transmitted through mirror 2, non resonant wavelengths of light will not fit into the cavity mode and subsequently be be reflected off of mirror 1.

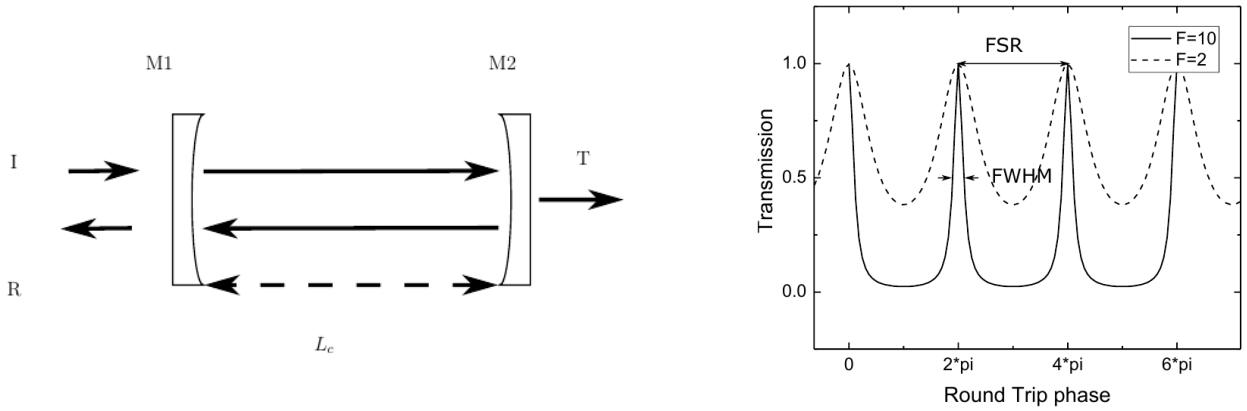

Figure 2.1. Fabry-Perot optical cavity (a) Incident beam I enters the backside of mirror 1, travels the length of the cavity L_c and back. When the wavelength of light is an integer multiple of the round-trip cavity length a resonance will occur and the light will be transmitted through mirror 2, otherwise via destructive interference it is reflected off of mirror 1. (b) Transmission spectrum for a FP with finesse of 2 (dashed) and 10 (solid) lines. Higher reflectivity mirrors leads to higher finesse, lower photon leakage rate, κ narrowing resonances.

The transmitted spectrum of light through the cavity (T) will consist of a series of peaks at resonant modes, each separated in frequency by the free spectral range of the cavity $FSR = c/n_c L$ with width $\delta\omega = FWHM$ [23]

$$T = \frac{1}{1 + (4\mathcal{F}/\pi^2) sin(\delta/2)^2} \tag{2.1}$$

$$\mathcal{F} = \frac{\pi r}{1 - r^2} = \frac{\omega_{FSR}}{\delta\omega} \tag{2.2}$$

where the cavity finesse ($\mathcal{F}$) is a function of the mirror reflectivity (r) and characterizes the loss of system. A more universal figure of merit which can be used to describe how under damped a resonator is, is the quality factor Q,

$$Q = \frac{\omega}{\kappa} = \mathcal{F}\frac{\omega}{\omega_{FRS}} \tag{2.3}$$

where ω is the resonant mode frequency and $\kappa = \delta\omega$ is the decay rate of the excitation (photon leakage rate for the case of an optical resonator). To facilitate coherent interactions between atoms we are fighting a race between the atom photon coupling strength, which determines the atom-atom interaction rate, and sources of photon loss, which immediately decohere the system, hence we are interested in an optical resonator with a very high Q value. In addition, for simplicity and controlabillity, we require the atom only interact with a single mode of the optical resonator at a time, meaning we must find a resonator with a sufficiently large free spectral range such that neighboring modes are extremely detuned from our relevant atomic transitions.

2.2 Micro-Ring Resonators

In our experiment we will be implementing micro-ring dielectric waveguide resonators, which have a different mode of operation then the previously mentioned FP cavities but demonstrate several of the same optical characteristics. In essence, a ring resonator is an optical waveguide which has been wound back upon itself forming a closed loop. Light is

confined via total internal reflection using a high dielectric contrast design, and supports circulating whispering gallery modes (WGMs)[24][25][26].

Originally discovered by Rayleigh while studying acoustic waves, WGMs are circulating waves that are confined by continuous inward reflection about a concave surface. This results in ring-like equatorial modes strongly concentrated near the surface of the dielectric structure. Dielectric resonators that support optical WGM's have been widely studied the last few decades for several different geometries including the aforementioned micro-ring resonators, as well as micro-toroid, micro-disk, micro-bottle and micro-spherical devices. Much like FP cavities, when the circumference of the resonator is an integer multiple of the wavelengths a resonance will occur, with neighboring resonances separated by the FSR of the resonator. While there are not exact analytic solutions for our particular system of dielectric ring on a flat square substrate, a simpler example of a Micro-spherical resonator will support TE and TM WGM modes with the primary electric field components taking the form of [26]

$$E_{mlq} = (r, \theta, \phi) \sim \mathrm{j}_m(nk_q) \times Y_l^m(\theta, \phi), \tag{2.4}$$

where j and Y are the spherical Bessel functions and spherical harmonics respectively, q denotes the order of the Bessel function, m is the angular momentum denoting the number of spatial periods that fit into the mode.

WGM resonators can demonstrate extremely high Q factors (greater than 10^{11}) [27], and small mode volumes on the order of ($V_m \sim \lambda^3$) in some devices, making them extremely attractive for use in CQED experiments[28], nonlinear optics[29], quantum information, and sensing applications[30]. In addition, these devices can be fabricated into monolithic designs, allowing for excellent mechanical stability with greatly reduced low frequency noise compared to conventional FP cavities.

The losses in a WGM resonator can be grouped into by three factors; absorption losses, bending losses, and surface scattering [31], $Q_0^{-1} = Q_{ss}^{-1} + Q_{abs}^{-1} + Q_{bend}^{-1}$. Bending losses for our system were calculated to have a lower limit of $Q_{bend} = 170$ million via FTDT simulations. Internal losses are primarily due to absorption in the waveguide, $Q_{abs} = 2\pi n/\lambda\alpha$ wher α is the absorption coefficient of silicon nitride. The largest source of loss in our system is surface scattering off of the edges of our waveguide structure due to finite surface roughness,

$$Q_{ss} = \frac{3\lambda^3 R}{8\pi^2 \bar{n} B^2 s^2} \tag{2.5}$$

where $\bar{n}$ is the effective index of refraction of the waveguide substrate system, 's' is the rms size of the surface roughness, and B is the correlation length of the roughness at the surface of the resonator.

We are specifically working with a silicon based micro-ring resonator design where the waveguide consists of a silicon nitride layer which has been fabricated on top of a silicon dioxide membrane. Conveniently, silicon based photonics [32] can be readily fabricated using traditional CMOS equipment and techniques that are commonly used for producing electronics. This has been a huge advantage for our group, as university fabrication labs typically have the equipment required for CMOS processing. It can not be understated how impactful having Tzu-Han design and fabricate these devices in house has been, it would have been extremely time and cost prohibitive to iteratively go back and forth with an external vendor over the life of this experiment as we prototyped and customized our design.

Our device (figure 2.2) starts with a silicon wafer which is cut into a $1cm^2$ square chip. A 550nm silicon nitride bottom layer followed by a 2μm silicon dioxide layer are grown on the chip using low pressure chemical vapor deposition (CVD). Later on in the fabrication process, the silicon substrate will be etched away from a 2x8mm window region bellow the micro-ring resonator section of the chip, releasing the membrane and allowing optical access to trap and cool nearby atoms nearby our structures as well as other processes. The thicknesses of the

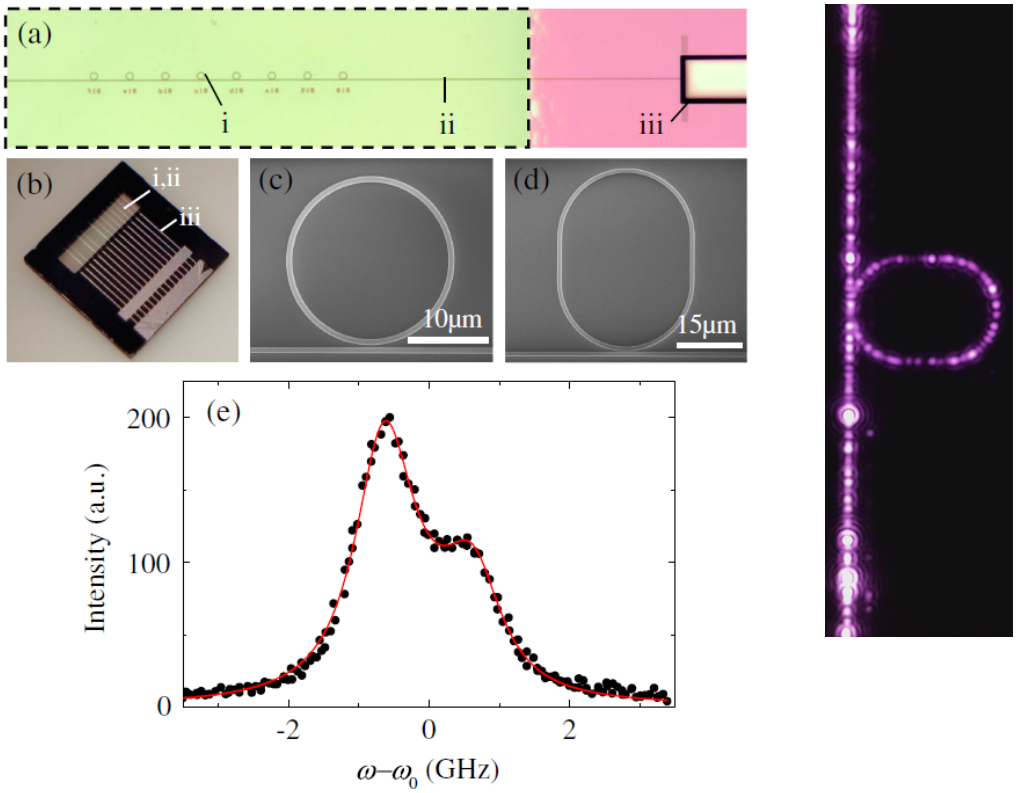

Figure 2.2. Overview of photonic chip platform a) View of waveguide channel on optical chip. i) Silicon nitride microring resonators and ii) bus waveguide (grey) on silicon dioxide window (light yellow). iii) Fiber docking U-groove for coupling external fiber to bus waveguide. b) Zoom out of optical chip, i,ii) 2x8mm SiO_2 window supporting nanophotonic structures and iii) fiber docking U-groove. c,d) Zoom in of microring and racetrack resonators used in our experiments. e) Resonance scan of racetrack resonator taken via scattering intensity measurements. Right) Fit to our resonance curve yields $(\omega_0, \beta, \kappa) = 2\pi \cdot (334.792 \times 10^3,\ 0.655,\ 1.01)$GHz

layers was chosen to provide sufficiently high tensile and compressive strength to prevent the window from breaking or bending after it's release from the substrate. In addition, while the $Si_3 - N_4 SiO_2$ window is mostly transparent to our relevant laser wavelengths, we make use of the fact that a small percentage of the optical tweezer beam, used for trapping atoms in our experiment, does get reflected resulting in the production of a 1D tweezer lattice in close proximity to the surface. The lattice potential provides much tighter confinement of atoms in the vertical direction above the chip compared to a free-space gaussian tweezer beam, with

the first potential minimum's height from the surface being tunable via the dielectric layer's thicknesses. To finish the growth process, an additional silicon nitride top layer is deposited which will be patterned into the waveguides and nanophotonic structures comprising our design using E-Beam lithography.

Each chip contains multiple bus waveguides evanescently coupled to arrays of micro-ring resonators which will be characterized after the chip is constructed, allowing us to select the rings which resulted in the highest Q factor and with resonances sufficiently close to the desired atomic transition of our cesium atoms. The optical properties of the resonators are measured via resonance florescence scans wherein a narrow band DBR laser is fiber coupled to an on chip waveguide which is in turn evanescently coupled to the micro-ring resonators. When the laser wavelength is swept through a cavity resonance coupling is permitted and the micro-ring's intra-cavity light will greatly increase, with scattering mechanisms in the resonator making the ring viewable via an optical microscope. To perform a resonance scan, the PID lock for the TEC that controls the DBR laser's temperature was modified to accept a DAC output channel from a labview card, and a program was wrote to uniformly step temperature, monitor laser frequency, then take images via a raspberry pi camera connected to the microscope for measuring relative intensity.

The figure of merit for atom-cavity systems is the number of coherent oscillations per photon loss which scales as the square root of atom-photon coopertivity 'C' eq 2.6, where 'Q' is again the quality factor, V_m is the mode volume, and λ is the resonant wavelength. Our device was designed to optimize C, balancing the higher Q factor achieved with increased bending radius at the cost of an increasing mode volume, which can be thought of as diluting the field strength per photon in a given mode. Our current devices have a circumference on the order of 100 μm with a FSR of 500 GHz, waveguide width and height dimensions of (W,H=750,380 nm), a quality factor on the order of $Q = 1 \sim 3 \times 10^5$, and a mode volume of $\sim 500\mu m^3$ for an atom trapped 100nm above the surface. Our quality factor is currently limited by the surface roughness of the waveguides which form our micro-ring resonators,

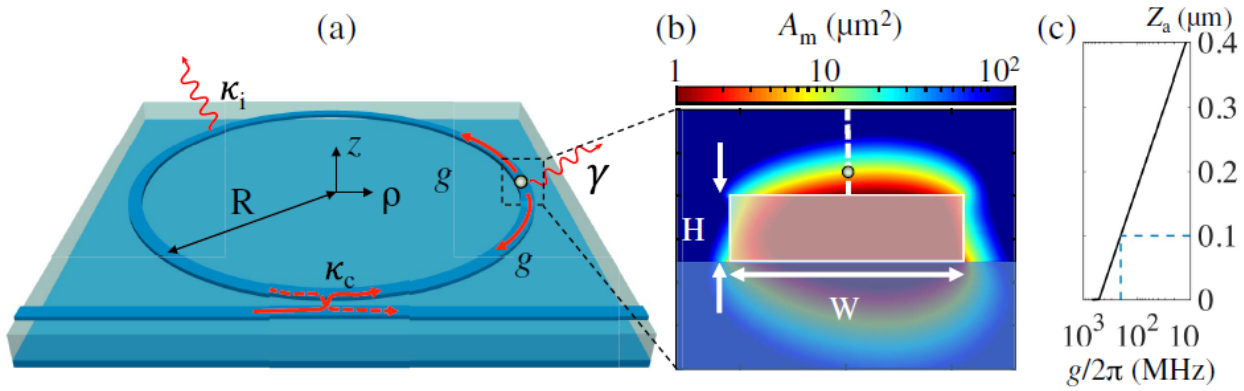

Figure 2.3. Atom-Resonator coupling scheme. a) Silicon nitride micro-ring resonator and bus waveguide (dark blue) on top of silicon dioxide (transparent light blue)- silicon nitride (dark blue) bilayer window, with an atom positioned above the microring (gray) coupled with strength g. Injected light for the left evanescently couples into the micro-ring at rate κ_c exciting the counter clockwise (CCW) mode. Once the cavity mode is excited there are a few possible interactions: coherent back-scattering will lead to cross coupling of the clockwise mode (CW), intrinsic losses of the micro-ring will lead to photon loss at rate κ_i, the excitation may be exchanged back and forth with the atom at coupling strength 'g', the atom may lose an excitation to the environment via spontaneous emission at rate γ, or light may re-couple to the bus waveguide at rate κ_c. b) Cross-sectional view of micro-ring waveguide depicting mode area for an atom coupled to the ring at height z_a above the waveguide. c) Calculated atom-photon coupling strength vs atom height, centered above the waveguide of the micro-ring, where the blue-dash corresponds to our target trapping height of 100nm above the surface

but with state of the art fabrication methods for limiting surface roughness our current design is projected to have a possible Q on the order of 10^6. While silicon nitride micro-rings are commonly used to produce Q factors orders of magnitudes above ours, our device must satisfy constraints for use with cold cesium atoms with resonant wavelengths at Cesium's D1 and D2 transitions ($\sim 850 - 900nm$) instead of silicons low-loss telecom band near 1500nm.

$$\sqrt{C} \sim \sqrt{\frac{Q}{V_m/\lambda^3}} \tag{2.6}$$

Once we have a functioning photonic-chip, with an identified optimal resonator, the device is epoxied onto a PEEK chip carrier platform with grooves for docking into an electronic

translation stage fixed inside of our vacuum chamber for experiments. We select resonators which have resonances slightly blue detuned from the target cesium transition as in situe during experiments finite absorption of our lasers will lead to heating of the micro-ring and red-shift the resonance. Once inside the chamber we re-measure the rings resonance, then introduce light from an additional 1060nm heating beam incident on the bottom side of the silicon chip nearby the window to tune the device onto atomic resonance. While silicon nitride's thermal expansion coefficient is pretty small at around 2×10^{-6} its thermo-optic coefficient is on the order of $10^{-}5$ at room temperature [33], which together result in a -0.5GHz/mW resonance shift allowing a tuning range of approximately 100 GHz with our setup.

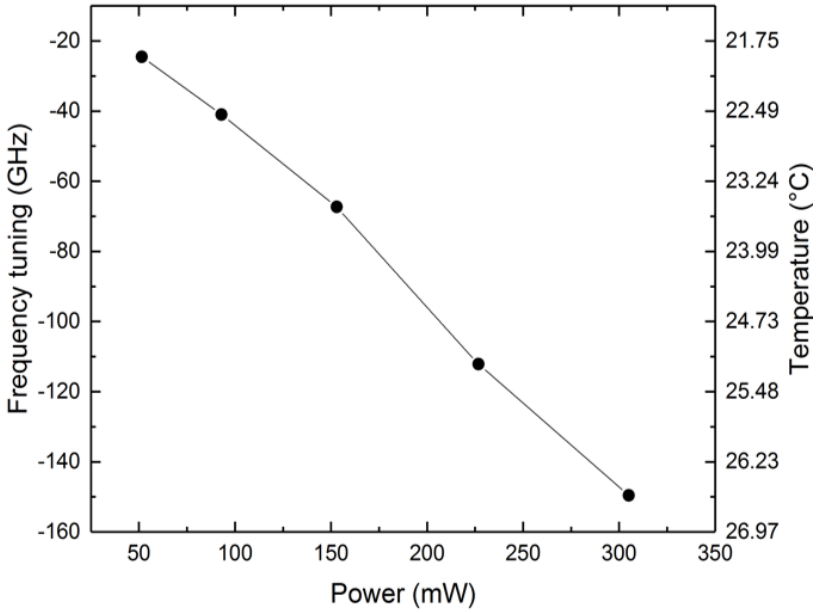

Figure 2.4. Thermal tuning of micro-ring resonance by laser heating from a 1064 Nd-YAG illuminating the backside of the silicon chip nearby the SiO_2 window. A combination of thermal expansion and thermal dependence on the effective index of refraction yield a -0.5GHz/mW frequency shift of the micro-ring resonance

The photonic chips used throughout our experiments were all designed, fabricated and tested by my colleague Tzu-Han Chang working at Purdue's Birck Nanotechnology center. It

has taken a tremendous amount of work on his part to develop these designs and fabrication processes coming from a group of mostly AMO experimentalists lacking experience in these techniques. Beyond the features described in this introduction, many other challenges have been overcome through multiple generations of chips, including design of micro-ring to bus waveguide interfaces to produce critical coupling and a great deal of effort on the U-groove external fiber to bus waveguide-mating.

2.3 Jaynes-Cummings Model

The simplest model used to describe an atom interacting with the field of a cavity is the Jaynes-Cummings Model. This model describes a two level atom ($|1\rangle, |2\rangle$) with energies energies (ω_1, ω_2) interacting with a single mode of an optical cavity at frequency ω_C and ignores any source of dissipation. For our ring resonator, the FSR is large enough to neglect all modes except one, tuned near atom resonance. The Hamiltonian consists of three terms, the internal energy of the atom H_A, the cavity field energy H_C, and the interaction term coupling the atomic dipole moment with the cavity mode H_I,[34][35]

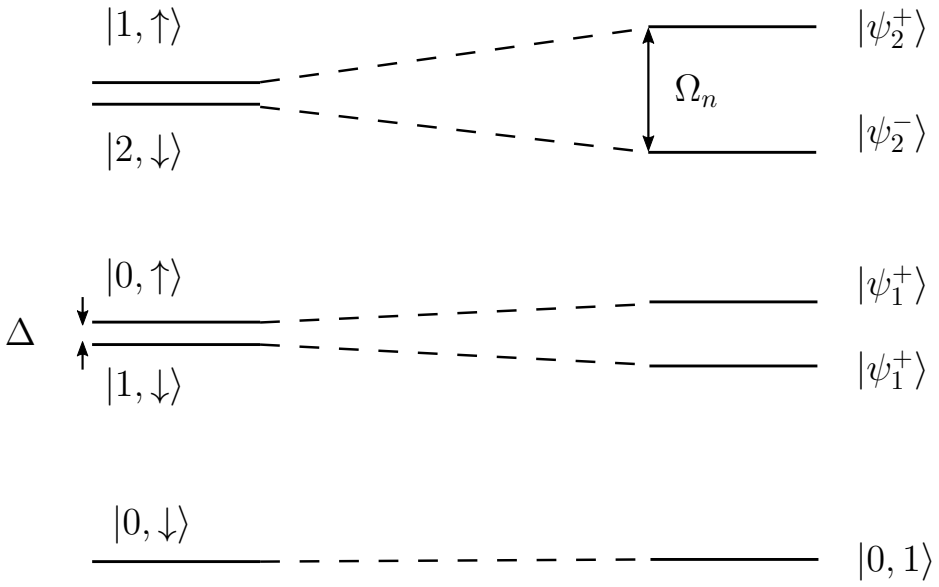

Figure 2.5. Jaynes-Cummings example for the case of a two level atom $(\uparrow,\downarrow)$ and a cavity mode with photon number state (n), detuned by Δ from atomic resonance. When the atom-photon coupling g is introduced, the eigen-states split further forming the dressed states $|\psi\rangle$ separated in energy by effective Rabi frequency $\Omega_n = \sqrt{4(n+1)g_0^2 + \Delta^2}$

$$H_A = \hbar\omega_1 |1\rangle\langle 1| + \hbar\omega_2 |2\rangle\langle 2| \tag{2.7}$$

$$H_C = \hbar\omega_c(a^\dagger a + 1/2) \tag{2.8}$$

$$H_I = \vec{d}\cdot\vec{E} \tag{2.9}$$

$$\vec{d} = \vec{d_{1,2}}\left(\sigma^- + \sigma^+\right) \tag{2.10}$$

where $a^\dagger, a$ are the photon creation and annihilation operations, $\sigma^{+(-)} = |2\rangle\langle 1|\left(|1\rangle\langle 2|\right)$ are the atomic raising(lowering) operators, $\vec{d}$ is the atomic dipole operator, and $\vec{d_{1,2}} = \vec{d_{2,1}} = \langle 2|\vec{d}|1\rangle$ are the transition dipole matrix elements which can be calculated using Wigner-Eckart theorem and the relevant Clebsch-Gordon coefficients. Making the rotating wave ap-

proximation (RWA) for H_I, where energy non-conserving counter rotating terms are dropped yields the interaction Hamiltonian,

$$H_I = \hbar g(\sigma^- a^\dagger + \sigma^+ a) \tag{2.11}$$

The $\sigma^- a^\dagger$ term describes a process where an atom in the excited state decays to the ground state by emitting a photon into the cavity field, $\sigma^+ a$ describes the reverse process where a ground state atom absorbs a photon from the cavity mode. g_0 is refereed to as the atom-cavity coupling constant or the single photon vacuum Rabi frequency, and is defined by the interaction strength of atom in the presence of the cavities vacuum field.

$$\Delta E = \hbar g_0 = \langle \bar{d_{12}} \cdot \vec{E}_{vac} \rangle \tag{2.12}$$

$$g_0 = \sqrt{\frac{d_{12}^2 \omega_c}{2\epsilon_0 \hbar V}} \tag{2.13}$$

where V is the mode volume, (V=Length $\times$ Mode Area $= L \times \frac{\int \epsilon |E(r)|^2}{\epsilon |E(r_{atom})|^2}$). In the $|n-1, 2\rangle, |n, 1\rangle$ basis where the first number is the photonic state and the second is the atomic internal state, the Hamiltonian can be cast in 2d block form yielding

$$H_{JC} = \hbar \begin{bmatrix} \omega_1 + \omega_c(n + 3/2) & g\sqrt{n+1} \\ g\sqrt{n+1} & \omega_2 + \omega_c(n + 1/2) \end{bmatrix} \tag{2.14}$$

The energy eigenstates of the system are no longer the pure atom/photonic state but the dressed states

$$\left|\psi^{+}\right\rangle = cos\theta \left|n,2\right\rangle + sin\theta \left|n+1,1\right\rangle \tag{2.15}$$

$$\left|\psi^{-}\right\rangle = -sin\theta \left|n,2\right\rangle + cos\theta \left|n+1,1\right\rangle \tag{2.16}$$

$$\tag{2.17}$$

with eigen-frequencies,

$$\omega^{\pm} = \omega_c(n+1/2) \pm 1/2\sqrt{(4n+1)g_0^2 + \Delta^2} \tag{2.18}$$

where ($\Delta = \omega_2 - \omega_1 - \omega_c$) is the cavity detuning from atomic resonance, and θ_n is the mixing angle defined by [34][35]

$$tan(2\theta) = \frac{-2g_0\sqrt{n+1}}{\Delta} \tag{2.19}$$

In the absence of coupling between the atomic and photonic states the energy eigenstates form a ladder series of nearly degenerate doublets split by the cavity detuning that repeat every ω_c. When the atom-cavity coupling is included, the eigenstates separate further into the dressed states ψ_n^+ and ψ_n^- with the splitting equal to the effective Rabi frequency $\Omega_n = \sqrt{4(n+1)g_0^2 + \Delta^2}$. An initially excited atom prepared in $|n-1,2\rangle$ will undergo stimulated emission decaying to $|n-1,2\rangle$ and vise versa, with the populations oscillating at frequency Ω_n.

2.4 Doppler Cooling

Much work has been spent the last few decades in developing techniques to trap, cool, and coherently manipulate the state of individuals atoms/ions as well as the collective states of dilute gases. Perhaps the most ubiquitous form of laser cooling, Doppler cooling [36][37], makes use of the relativistic shift caused by an atoms motion to produce a velocity dependent

scattering rate. For the case of a two level atom scattering light from a coherent laser field, the scattering rate γ_p is described by the Lorentzian,

$$\gamma_p = \frac{\gamma}{4} \frac{\Omega^2}{\delta^2 + \Omega^2/2 + \gamma^2/4} \tag{2.20}$$

where γ is the transitions decay rate, Ω is the Rabi rate, $\delta = \delta_0 + kv$ is the laser's Doppler shifted detuning in the atoms frame, and $\delta_0 = \omega - \omega_0$ is the laser detuning from resonance. If a laser is red detuned (lower frequency) of the transition, light in the atom's frame will be Doppler shifted towards resonance when the atom is moving towards the laser and the atom will scatter photons at a higher rate. Every time the atom scatters a photon, it will receive a momentum kick of $\hbar k$ opposite its direction of motion during absorption, slowing the atom down for the case of an atom moving towards a red detuned beam. It will subsequently spontaneously emit a photon giving another kick $\hbar k$ in a random direction, but after several cycles these will produce an average of zero change in momentum due to the isotropic scattering. When the atom moves away from the laser, the initially red detuned light is even further red detuned in the atom's reference frame and the scattering rate is further reduced, decreasing the probability of an atom to receive a momentum kick in it's direction of travel and hence limiting re-heating.

Applying three orthogonal pairs of counter-propagating laser beams allows for the cooling of motion in all directions, and is referred to as 'optical molasses'. Adding the force of each counter propagating beam, $\hbar k\gamma_{p(+)} - \hbar k\gamma_{p(-)}$, yields a velocity dependent dampening force,

$$\vec{F_{OM}} \approx \frac{8\hbar k^2 \delta s_0 \vec{v}}{\gamma(1 + s_0 + (2\delta_0/\gamma)^2)} = -\beta\vec{v} \tag{2.21}$$

With an optimum detuning of $\delta = \gamma/2$, optical molasses will continue to cool until the 'Doppler limit' is reached, $T_D = \hbar\gamma/2k_B$ [38] with typical values of a few 100 μK, for cesium $T_D = 125\mu K$. This lower limit arises due to statistical fluctuations in the absorption and emission processes. While the change in velocity from spontaneous emission kicks averages

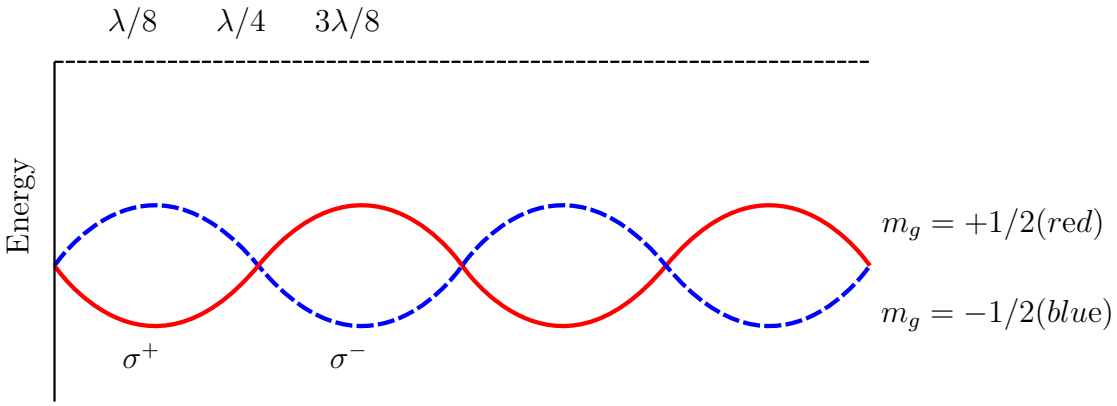

Figure 2.6. Lin-Perp-Lin polarization gradient cooling scheme. Light shift experienced by $m_g = \pm 1/2$ spin states traveling through polarization gradient formed by two counter-propagating beams of the same frequency and orthogonal linear polarizations.

to zero, the mean square value does not go to zero, leading to an unavoidable finite amount of heating, preventing reaching T=0K. In addition, variations in the rate of absorption causes additional heating. At the Doppler limit, the rate of heating due to these processes is balanced by the rate of cooling.

2.5 Polarization Gradient Cooling

It is possible to achieve temperatures below the Doppler cooling limit, but to do so requires schemes that make use of additional atomic sub-levels. One of the most effective is Polarization-Gradient cooling[39][37]. If two beams of the same frequency and linear, perpendicular, polarizations are aligned in a counter-propagating manor, a standing wave is produced with a spatially varying polarization. The resultant pattern will alternate between linear and circular polarization every 1/8th of a wavelength.

For an example consider the effect of this field on an atom with a J=1/2 ground state and J=3/2 excited state. The atom will experience a state dependent light shift given by

$$\Delta E_g = \frac{\hbar \delta s_0 C_{ge}^{1/2}}{1 + (2\delta\gamma)^2} \tag{2.22}$$

where C_{ge} are the relevant Clebsch-Gordon coefficients. When the polarization is $\sigma^{+(-)}$ the $m_j = 1/2(-1/2)$ state will have a larger, more negative, light shift. In addition due to selection rules, the $\sigma^{+(-)}$ light will optically pump atoms into the $m_j = 1/2(-1/2)$ ground state. For an atom starting out in the $m_j = 1/2$ state at $x = \lambda/8$ as the atom moves to the right, it will lose kinetic energy as it climbs the potential hill approaching $x = 3\lambda/8$, at which point absorption of a σ^+ photon followed by spontaneous emission will favor pumping the atom into the $m_j = -1/2$ state, removing energy form the system and the process will repeat as the atom continues moving. PGC is most effective when the atoms are initially cold enough such that the time it takes to travel from trough to peek is comparable to the scattering rate.

2.6 Magneto-Optical Trap (MOT)

The Magneto Optical trap (MOT) is a widespread technique used in AMO experiments to trap and cool large numbers of atoms over a wide thermal range. In our experiment we make use of three MOT implementations; a 'source MOT' to collect the initial hot flux of atoms emitted by our cesium source, a 'science MOT' near the center of our main 'science chamber' to collect atoms which have been pushed through a differential pumping tube from the source to the science chamber, and a final 'mini-MOT' making use of small 1mm beams passing through the window of our photonic chip to localize atoms about 100 microns above the surface of the chip to load atoms into our optical tweezer traps.

The operation principal is displayed in figure (2.7), considering the case of a two level atom with ground state spin 0 and excited state spin 1[40]. A magnetic quadrupole field is applied as well as three orthogonal pairs of counter-propagating circularly polarized laser beams, red detuned from the $j = 0 \rightarrow j = 1$ transition. For small displacements from the trap's center the magnetic field is approximately linear,$\vec{B} = -c_z Z$ leading to a spatially dependent Zeeman splitting of the excited spin states $\delta E = -\mu_B m_s c_z z$. For the case of the z axis, as the atom moves up(down) the transition to the ms=-1(+1) state is shifted

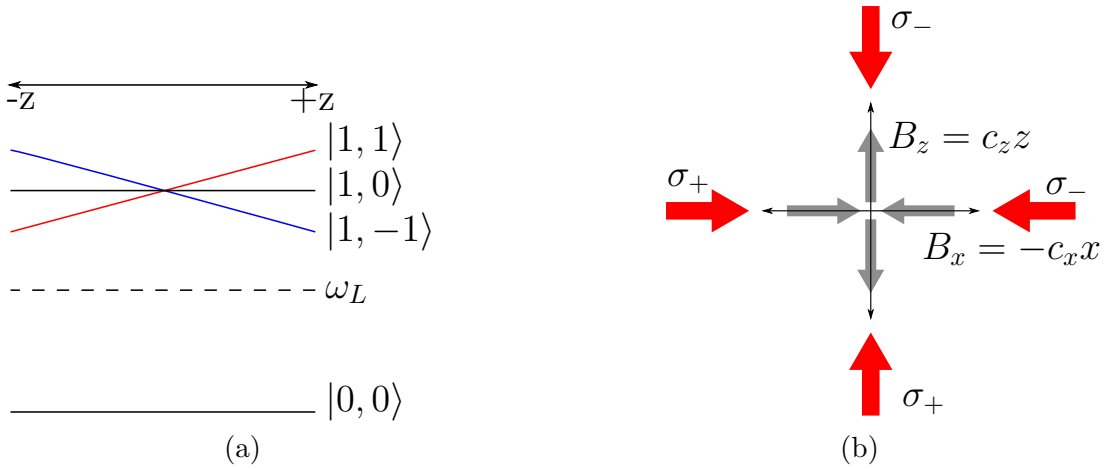

Figure 2.7. Magneto Optical Trap. a) Energy level diagram for the $|s, m_s\rangle$ sub-levels of the spin one excited state in the presence of a magnetic quadrupole field. Near the trap's center the magnetic field is approximately linear with displacement resulting in a spatially dependent Zeeman shift, breaking degeneracy b) X Z cross section of MOT center. Magnetic field directions shown in gray, laser beams in red accompanied by their relevant polarization. As an atom moves in the +z direction towards the σ^- vertical beam and away from the σ^+ beam, the $|1,1\rangle$ shifts closer to resonance and the atom preferentially scatters more light from the incoming σ^- beam pushing it back towards the center, and vice versa for motion in the -z direction

closer to the laser frequency and the atom will preferentially scatter more photons from the counter-propagating $\sigma_-(\sigma_+)$ beam while the $\sigma_+(\sigma_-)$ beam's transition will be further detuned preventing momentum kicks in the direction of the atoms motion that would lead to heating. This preferential scattering provides a restoring force confining atoms to the center of the trap, as well as a cooling mechanism. Magneto-optical-traps are routinely used to trap clouds of up to billions of atoms and temperatures on the order of 10's of micro-kelvin.

2.7 Optical Dipole Traps

An optical dipole trap is a simple but powerful tool for trapping atoms, nano-particles, and even viruses through use of a strong focused beam. When an atom is placed in a laser field red detuned from a transition, a dipole moment (p) is induced in the atom of magnitude ($p_0 = \alpha E_0$) from off-resonant coupling of the ground state to an excited state where α is the atomic polarizability (eq 2.23), E_0 is the amplitude of the electric field, ω is the laser frequency, ω_0 is the atomic transition frequency, and Γ is the scattering rate of the transition.

$$\alpha = \frac{6\epsilon_0 \pi c^3}{\omega_0^2} \frac{\Gamma}{\omega_0^2 - \omega^2 - i\Gamma(\omega^3/\omega^2)} \tag{2.23}$$

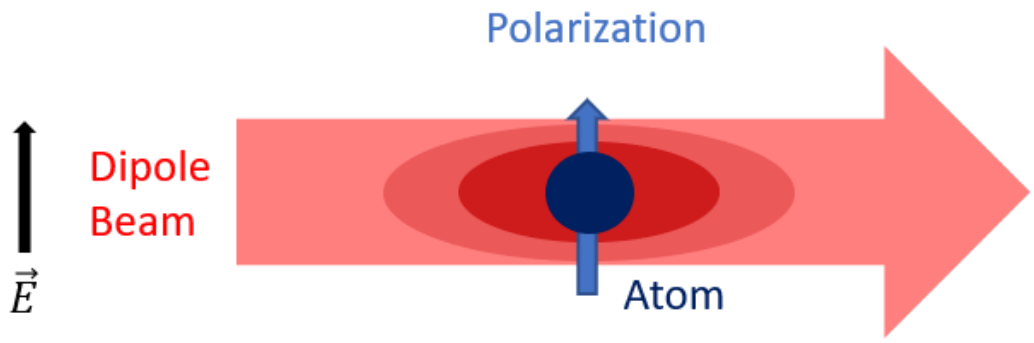

(a)

Figure 2.8. Optical Dipole Trap schematic. When an atom (blue) is subject to the electric field of laser beam (red) which is far red detuned from an atomic resonance ($\Delta = negative$), a dipole moment is induced in the atom (p), aligned to the lasers polarization. This dipole moment then interacts with the field of the laser experiencing potential $U = \frac{-1}{2}\langle \vec{p} \cdot \vec{E} \rangle = \frac{3\pi c^2 \gamma}{2\omega_0^3 \Delta} I(\rho, \vec{z})$ with a force exerted on the atom proportional to the gradient of the intensity. For a focused, gaussian beam, and a red detuned beam the atom is attracted towards the strongest intensity (darker red) part of the beam.

This dipole moment will in turn interact with the electric field from the laser beam and experience a force proportional to the gradient of the intensity of the beam producing a potential energy U,

$$U = \frac{-1}{2}\langle \vec{p} \cdot \vec{E} \rangle = \frac{1}{2\epsilon_0 c} Re(\alpha) I \tag{2.24}$$

$$U(\vec{\rho,z}) = \frac{3\pi c^2 \Gamma}{2\omega_0^3} \left(\frac{1}{\omega_0 - \omega} + \frac{1}{\omega_0 + \omega} \right) I(\vec{r}) \tag{2.25}$$

Using the intensity for a focused Gaussian beam $I(\rho, z)$ and making the rotating wave approximation where the counter rotating term is neglected $(\omega_0 - \omega) = \Delta << (\omega_0 + \omega)$ yielding,

$$I(\rho, z) = \frac{2P}{\pi w^2(z)} \mathrm{e}^{-2\rho^2/w^2(z)} \tag{2.26}$$

$$U(\vec{\rho,z}) = \frac{3\pi c^2 \gamma}{2\omega_0^3 \Delta} I(\vec{\rho,z}) \tag{2.27}$$

where P is the power of the beam, I is the intensity pattern, ρ is the radial distance, z the axial distance in the direction of propagation, $w(z) = w_0\sqrt{1 + (z/z_R)^2}$ is the beam radius, w_0 is the beam waist, and $z_R = \pi w_0^2/\lambda$ is the Rayleigh length. The atom off resonantly scatters photons at rate is $\gamma_{sc} = \frac{\gamma}{\hbar\Delta} U(r)$, the additional factor of $1/\Delta$ relative to the trapping potential allows for the creation of a strong trap with sufficient time between scattering events for coherent operations to be performed on the atom by operating with a further detuned trap at higher optical power.

For the case of alkali atoms interacting with a laser detuning of $(\omega_{FS} >> \omega_L >> \omega_{HF})$, fine structure is then resolved and the D2 and D1 transitions will both contribute to the dipole trap potential with their respective scaling 2/3 and 1/3 from the relevant clebsch-gordon coefficients.

$$U(\vec{r}) = \frac{\pi c^2 \gamma}{2\omega_0^3}\left(\frac{2}{\Delta_2} + \frac{1}{\Delta_1}\right) I(\vec{r}) \tag{2.28}$$

$$U(\vec{r}) = \frac{3\pi c^2 \gamma}{2\omega_0^3 \Delta} I(\vec{r}) \tag{2.29}$$

For small displacements about the trap center the potential can be approximated as a 3d harmonic oscillator with trap frequencies $\omega_\rho = \sqrt{4U_0/mw_0^2}$ in the radial direction and $\omega_z = \sqrt{2U_0/mz_R^2}$ in the axial direction, where $U_0 = U(\vec{r} = 0)$ is referred to as the trap depth. In general $z_R << w_0$, resulting in a weaker trap in the axial direction. For cases that require a tight trap in all directions more than one dipole beam may be introduced, with overlap in the focal region producing a crossed trap, tightening the z direction.

2.8 Raman Transitions

Raman transitions[41][42] are a powerful tool used in a wide range of spectroscopic techniques[43][44], and cold atom applications such as sub-Doppler cooling schemes[45]. They consist of a two photon transition which coherently transfers a quantum system from one ground state to another via their mutual coupling to a third excited state, but without actually populating the excited state during the process. The importance of this may not seem immediately apparent, as cold atom systems are frequently prepared in desirable states via optical pumping routinely in AMO experiments, but unlike optical pumping which involves a spontaneous emission process from the excited state, destroying coherence and any possible entanglement between states, Raman transitions do not populate the excited state during the process and maintain coherence.

Our experiment relies on Raman physics for driving photon mediated atom-atom interactions (PMAAI)[46][47][48] between atoms mutually coupled to a micro-ring resonator mode in a process that can be thought of as a pair of synchronized Raman transitions where one

atom virtually absorbs a photon from an external 'Raman' laser and emits it into a cavity mode without excitation and flipping spin in the process, while a second atom does the reverse process absorbing the cavity photon and emitting it back into the laser field.

2.8.1 Raman Transitions in a Λ System

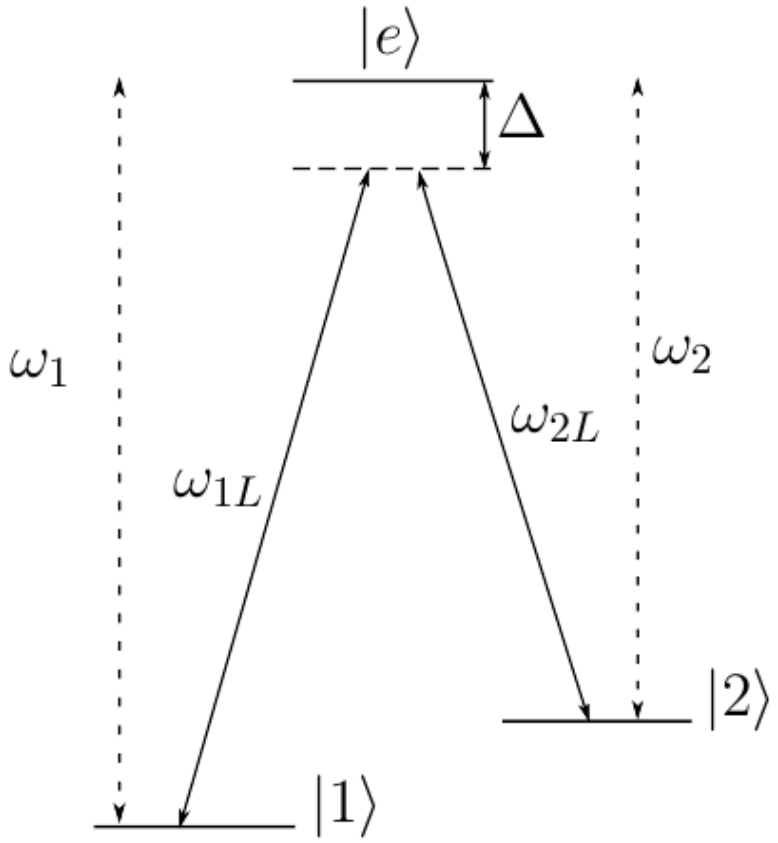

Figure 2.9. Raman transitions for atomic Λ system. Raman beams ω_{1L}, ω_{2L} simultaneously off resonantly drive $|1\rangle \rightarrow |e\rangle$ and $|2\rangle \rightarrow |e\rangle$ transitions at large detuning Δ. The atom coherently transfers population between the $|1\rangle \leftrightarrow |2\rangle$ ground states without actually populating the excited state $|e\rangle$ preventing spontaneous emission which would decohere the state.

To understand how Raman transitions occur, we will consider the case of a simple lambda scheme, (following works[35], [49], [50]) with hyperfine ground states $|1\rangle$, $|2\rangle$ and excited state $|e\rangle$. Raman beam 1 at frequency ω_{L1} couples state $|1\rangle$ to $|e\rangle$, Raman beam 2 at frequency

ω_{L2} couples state $|2\rangle$ to $|\mathrm{e}\rangle$. Both lasers $\omega_{L1(L2)}$ are 'Raman-resonant' with equal detuning Δ from their respective resonant frequencies $\omega_{1(2)}$

$$H_0 = \hbar\omega_1 |1\rangle\langle 1| + \hbar\omega_2 |2\rangle\langle 2| + \hbar\omega_\mathrm{e} |\mathrm{e}\rangle\langle \mathrm{e}| \tag{2.30}$$

$$\begin{aligned} H_I &= -\vec{d}\cdot\vec{E(t)} \\ &= \frac{1}{2}\Big(|1\rangle\langle \mathrm{e}|\,\bar{d_1} + |\mathrm{e}\rangle\langle 1|\,\bar{d_1} + |2\rangle\langle \mathrm{e}|\,\bar{d_2} + |\mathrm{e}\rangle\langle 2|\,\bar{d_2}\Big) \\ &\cdot\Big(\hat{\epsilon_1}E_1 cos(\vec{k_{1L}}\cdot\vec{r} - \omega_{1L}t) + \hat{\epsilon_2}E_2 cos(\vec{k_{2L}}\cdot\vec{r} - \omega_{2L}t)\Big) \end{aligned} \tag{2.31}$$

Where d_i are the dipole moment matrix elements coupling states i to j.

$$\bar{d_1} = \bar{d_{1\mathrm{e}}} = \bar{d^*_{\mathrm{e}1}} = \langle 1|\vec{d}|\mathrm{e}\rangle \tag{2.32}$$

$$\bar{d_2} = \bar{d_{2\mathrm{e}}} = \bar{d^*_{\mathrm{e}2}} = \langle 2|\vec{d}|\mathrm{e}\rangle \tag{2.33}$$

Next, making the rotating wave approximation, (dropping terms in the Hamiltonian that produce rapid time evolution $\sim(\omega_\mathrm{i}+\omega_\mathrm{j})$), and entering the rotating frame, (replacing state amplitudes in our wave function $|\Psi(t)\rangle = c_1(t)|1\rangle + c_2(t)|2\rangle + c_\mathrm{e}(t)|\mathrm{e}\rangle$ with the slowly varying functions $\tilde{c_\mathrm{i}}(t) = c_\mathrm{i}(t)\mathrm{e}^{-\mathrm{i}\omega_\mathrm{i}t}$) yields the interaction Hamiltonian,

$$\begin{aligned} \tilde{H} = &\Big(\frac{\hbar\Omega_1}{2}\mathrm{e}^{\mathrm{i}(\vec{k_1}\cdot\vec{r}-\Delta t)} + \frac{\hbar\Omega_{1,2}}{2}\mathrm{e}^{\mathrm{i}(\vec{k_1}\cdot\vec{r}-(\Delta+\omega_{12})t)}\Big)|1\rangle\langle \mathrm{e}| \\ &+ \Big(\frac{\hbar\Omega_2}{2}\mathrm{e}^{\mathrm{i}(\vec{k_2}\cdot\vec{r}-\Delta t)} + \frac{\hbar\Omega_{2,1}}{2}\mathrm{e}^{\mathrm{i}(\vec{k_2}\cdot\vec{r}-(\Delta-\omega_{12})t)}\Big)|2\rangle\langle \mathrm{e}| \\ &+ \Big(\frac{\hbar\Omega_1}{2}\mathrm{e}^{-\mathrm{i}(\vec{k_1}\cdot\vec{r}-\Delta t)} + \frac{\hbar\Omega_{1,2}}{2}\mathrm{e}^{-\mathrm{i}(\vec{k_1}\cdot\vec{r}-(\Delta+\omega_{12})t)}\Big)|\mathrm{e}\rangle\langle 1| \\ &+ \Big(\frac{\hbar\Omega_2}{2}\mathrm{e}^{-\mathrm{i}(\vec{k_2}\cdot\vec{r}-\Delta t)}) + \frac{\hbar\Omega_{2,1}}{2}\mathrm{e}^{-\mathrm{i}(\vec{k_2}\cdot\vec{r}-\Delta-\omega_{12}t))}\Big)|\mathrm{e}\rangle\langle 2| \end{aligned} \tag{2.34}$$

where we have introduced the direct and cross coupled Rabi frequencies,

$$\Omega_{\mathrm{i}} = \bar{d}_{\mathrm{i}} \cdot \hat{\epsilon}_{\mathrm{i}} E_{\mathrm{i}}/\hbar \tag{2.35}$$

$$\Omega_{\mathrm{i,j}} = \bar{d}_{\mathrm{i}} \cdot \hat{\epsilon}_{\mathrm{j}} E_{\mathrm{j}}/\hbar \tag{2.36}$$

Lastly, the excited state $|\mathrm{e}\rangle$ can be adiabatically eliminated leaving us with an effective interaction Raman Hamiltonian for the two level system $|1\rangle, |2\rangle$

$$\tilde{H_R} = -\hbar\omega_{AC1} |1\rangle\langle 1| - \frac{\hbar\Omega_R}{2} \mathrm{e}^{\mathrm{i}\Delta\vec{k}\cdot\vec{r}} |1\rangle\langle 2| - \hbar\omega_{AC2} |2\rangle\langle 2| - \frac{\hbar\Omega_R}{2} \mathrm{e}^{-\mathrm{i}\Delta\vec{k}\cdot\vec{r}} |2\rangle\langle 1| \tag{2.37}$$

$$\omega_{AC\mathrm{i}} = \frac{\Omega_{\mathrm{i}}^2}{4\Delta} + \frac{\Omega_{\mathrm{ij}}^2}{4(\Delta - \omega_{hf})} \tag{2.38}$$

where $\omega_{AC\mathrm{i}}$ is the light shift of state $|\mathrm{i}\rangle$ due to both lasers ω_{L1} & ω_{L2} and , $\Delta\vec{k}$ is the laser's wave vector difference, and $\Omega_R = \Omega_1\Omega_2/2\Delta$ is the Raman-Rabi frequency.

2.8.2 Raman Cooling

For some future experiments PGC cooling will not suffice, it will be very critical for us to cool atoms to their true ground state of motion, allowing for full quantum control of the motional state and potentially opening additonal degrees of freedom for our qubit register. For tightly bound atomic systems with narrow transitions, (ion traps) it is possible to spectrally resolve motional sidebands and hence drive the red band, removing phonons from the system until it is in the ground state of motion ($\omega_T > \Gamma$)[51]. For most neutral atom schemes, achieving such a strong trapping potential is not practical. For our particular system we will be implementing a 1mK scale tweezer trap to confine individual atoms with trap frequencies on the order of 10's-100's of kHzs, well within the linewidth of cesium's D1

and D2 transitions (4.56Mhz, 5.22MHz). To compensate for our smaller trap frequencies we will have to utilize Raman sideband Cooling (RSC) to reach the ground motional state.

The full cooling procedure only requires two steps, a reversible Raman transition, followed by an optical pumping step to restore the initial spin state [52]. In the $|n, \uparrow / \downarrow\rangle$ basis where n describes the vibrational (phonon number) state and the arrow describes the pseudospin up or down ground atomic states ($|\downarrow\rangle = |1\rangle, |\uparrow\rangle = |2\rangle$ as depicted in lambda scheme figure), the Raman transition between $|n, \uparrow\rangle \leftrightarrow |n-1, \downarrow\rangle \rightarrow |n-1, \mathrm{e}\rangle \rightarrow |n-1, \uparrow\rangle$ flips the spin of the atom while removing a phonon from the system. The process can be repeated until the atom is in it's ground state of motion (n=0) at which point there will no longer be a lower rung for the Raman transition to couple to and the atom will go dark to the Raman beams. The trick to implementing this technique is that the atom must be trapped tightly enough to be in the lamb-dicke regime $\eta^2(2n+1) \ll 1$, where $\eta = \sqrt{\frac{\omega_R}{\omega_t}}$ is the lamb dicke parameter, n is the motional quantum state, ω_R is the recoil frequency, and ω_t is the trap frequency. In short if the trap energy spacing is much larger than the recoil energy, during optical pumping the atom will have a very low probability of changing it's motional state (heating up) when spontaneous emission occurs, preventing heating.

3. APPARATUS

3.1 Lasers

Throughout our experiments we will be implementing several lasers to manipulate Cesium atoms via their D1 and D2 transitions as well as for probing our micro-ring resonators. We utilize several commercial products including; tapered amplifiers (TAs), distributed Bragg reflector lasers (DBRs), solid state Nd:YAG lasers and TiSaph lasers, as well as several homemade extended cavity diode lasers (ECDLs) operating in littrow configuration[53] implementing off the shelf semiconductor laser diodes in the NIR range. In the following I will describe our laser setups for addressing several of the needs in our experiment.

3.1.1 D1

Cesium's D1 transition from $6^2S_{1/2}$ to $6^2P_{1/2}$ occurs at 894.593nm (vacuum) with a decay rate of $\Gamma = 2\pi \times 4.575\text{MHz}$ and a transition dipole moment of $\left\langle J = \frac{1}{2}\middle||er|\middle|J = \frac{1}{2}\right\rangle = 2.702 \times 10^{-29} C \cdot m$[54]. In our experiments we will utilize Cesium's D1 transitions for coupling atoms to the cavity mode of our micro-ring resonator as well as possible future Raman schemes and optical pumping. We use three lasers in our D1 scheme; a master ECDL which is either operated free running or can be locked to Cesium's $6^2S_{1/2}\,|F=4\rangle \rightarrow 6^2P_{1/2}\,|F=3\rangle$ transition, a second slave ECDL for driving the $6^2S_{1/2}\,|F=3\rangle \rightarrow 6^2P_{1/2}\,|F=4\rangle$ transition (with the option to tune both master and slave for either transition depending on the experiment) and a tunable free running DBR laser used for broad scans of cavity resonance.

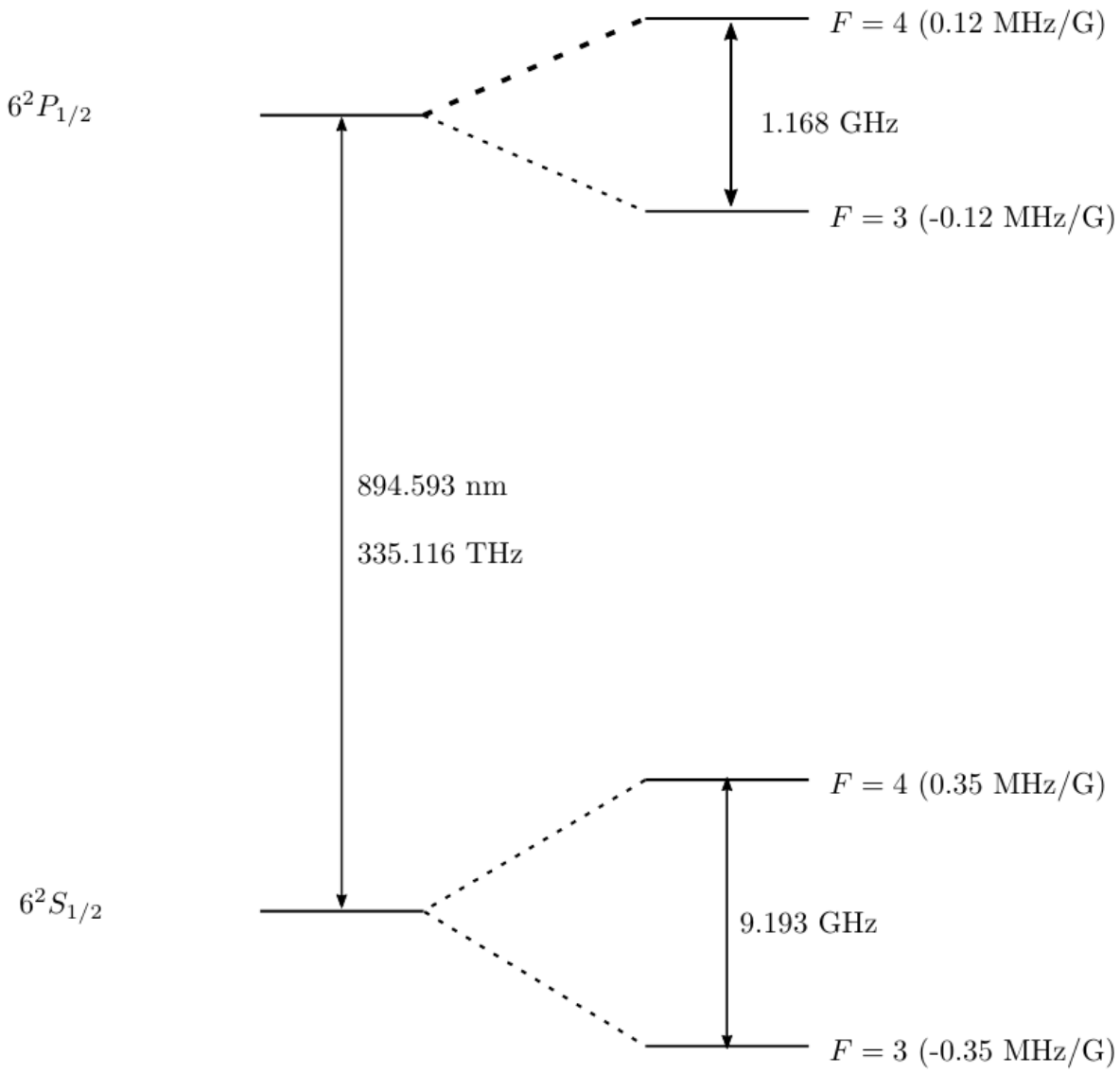

Figure 3.1. Energy level diagram for Cesium's $6^2S_{1/2}$ to $6^2P_{1/2}$ D1 transitions at 894.593nm[54]. The F=3,4 ground states are separated by Hyperfine splitting of 9.193GHz]

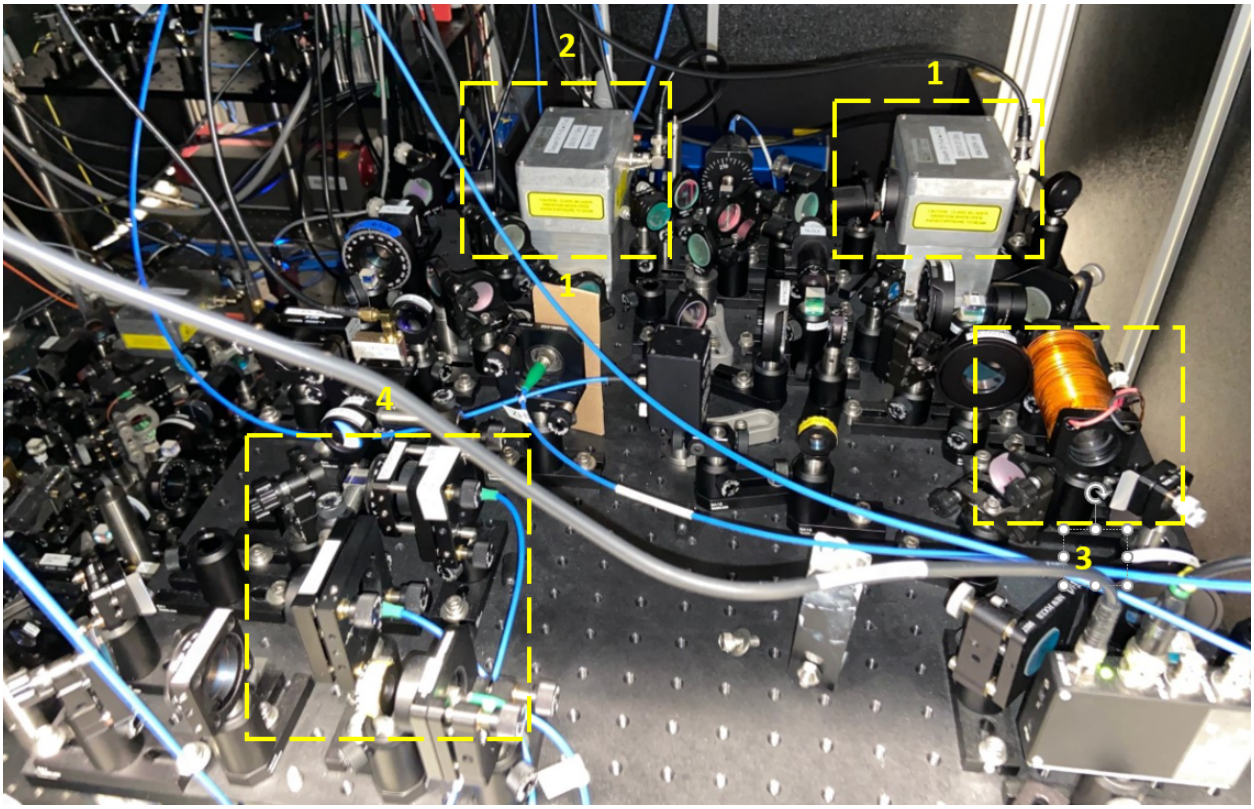

Figure 3.2. D1 Laser setup. 1) D1 master ECDL. 2) D1 slave ECDL locked to the master via an optical phase locked loop (OPLL) with tunable offset. 3) Polarization spectroscopy stage for locking master ECDL 4) Fiber couplings to chamber side of experiment

The master $4 \rightarrow 3$ ECDL is stabilized using polarization spectroscopy [55] [56] (figure 3.3), a technique related to saturated absorption. A beam from the master 4-3 ECDL is sent through a polarizing beam splitter cube (PBS), generating two beams of which one will be used as a pump and the other as a probe beam. The pump beam passes through a quarter wave plate (QWP) creating σ^+ polarized light which then passes through a Cesium cell, optically pumping atoms into the F=4, mF=4 state. This generates a circular dichroism for the linearly polarized probe beam as it passes through the Cesium cell. Using another QWP and a PBS the probe beam is then separated into σ^+ and σ^- components upon exiting the Cs cell, The difference in transmission between the polarizations is monitored via a balanced pair photo-detector generating our lock signal. Polarization spectroscopy allows for a stable

lock with a large capture range, without the need for lock in amplification or frequency dithering of the laser.

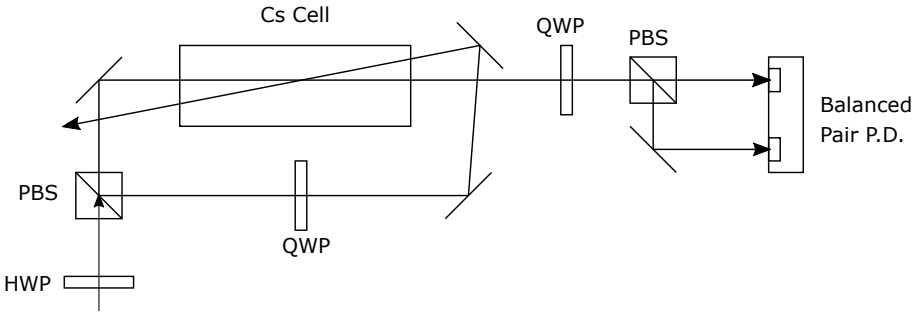

Figure 3.3. Polarization Spectroscopy optical diagram. Polarizing beam splitter cube (PBS), quarter wave plate (QWP), half wave plate (HWP), Cesium vapor cell (Cs Cell), Photo-detector (PD)

The slave $F = 3 \rightarrow F = 4$ ecdl is locked with a tunable frequency offset from the master laser via an optical phase lock loop (OPLL) allowing for a controllable detuning from resonance. Beams from both lasers are aligned co-propagating onto fast photo-detector (EOT ET-3500) creating a beat-note signal at the frequency difference of the lasers. This signal is first sent through a frequency divide by 2 prescaler (ADF5000), then into a high frequency divider/PLL synthesizer ADF4007 accompanied by a locking reference frequency created by a novatech DDS controlled via labview for setting the laser detuning at different stages of the experiment. Following the divide by 2 board the ADF4007 further divides both frequencies further down and implements a phase frequency detector followed by a charge pump which is fed into a PID lock controlling the slave ECDL's frequency via laser current and piezo control of the diffraction grating angle. An on board second order low pass filter was configured and tuned using Analogue Device's ADIsimPLL software with the following settings: VCO frequency of 9GHz, Kv value of 100MHz/V, loop bandwidth of 100kHz, and a phase margin of 50 degrees. The result is a very tight lock with a sub kilohertz bandwidth.

3.1.2 D2

Cesium's D2 transition from $6^2S_{1/2}$ to $6^2P_{3/2}$ occurs at 852.347 nm (vacuum) with a decay rate of $2\pi \times 4.575$MHz and and a transition dipole moment $\left\langle J = \frac{1}{2} \middle|| er \middle| J = \frac{3}{2} \right\rangle = 3.8014 \times 10^{-29} C \cdot m$[54]. We use Cesium's D2 line for trapping (MOT), cooling (PGC), state preparation and imaging in our experiments. In total four lasers are used to address Cesium's D2 transitions in our experiment: two littrow configuration ECDLs (reference and repumper), a Vescent Photonics D2-100-DBR laser and a Tapered amplifier, as well as an additional free running DBR for probing our micro-ring resonances for calibration.

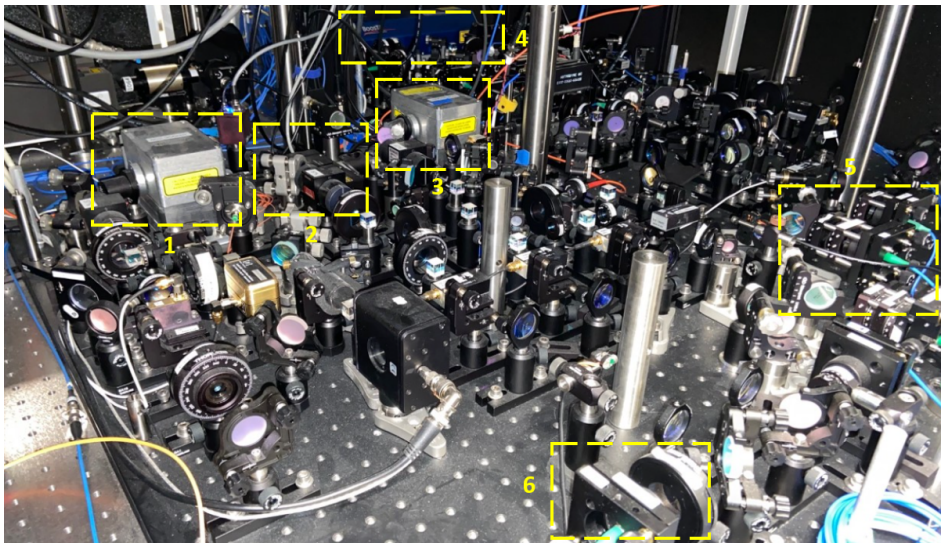

Figure 3.4. D2 Laser setup. 1) Master D2 ecdl locked to Cesium line from atoms in vapor cell via modulation transfer spectroscopy. 2) Commercial Vescent Photonics 852nm DBR laser with attached offset OPLL lock used for F=4-F'=5 transitions. 3) Repumper ecdl locked to master via an offset OPLL used for driving F=3-F'=4 transition. 4) Toptica BoostTA. F=3 and F=4 seed light is coupled in controlled via aom's providing and amplified mixture of both wavelengths. (Right of box) fiber couplings to experiment for source MOT, science MOT, mini MOT, push beam and florescence imaging. 4) Fiber couplings for D2 optical pumping and saturated absorption imaging. 6) Fiber coupling for kick-out beam

The Master (reference) laser outputs approximately 60mW of light at 852.356nm. The laser is stabilized by modulation transfer spectroscopy[57] using Cesium's $F = 4 \rightarrow F = 5$

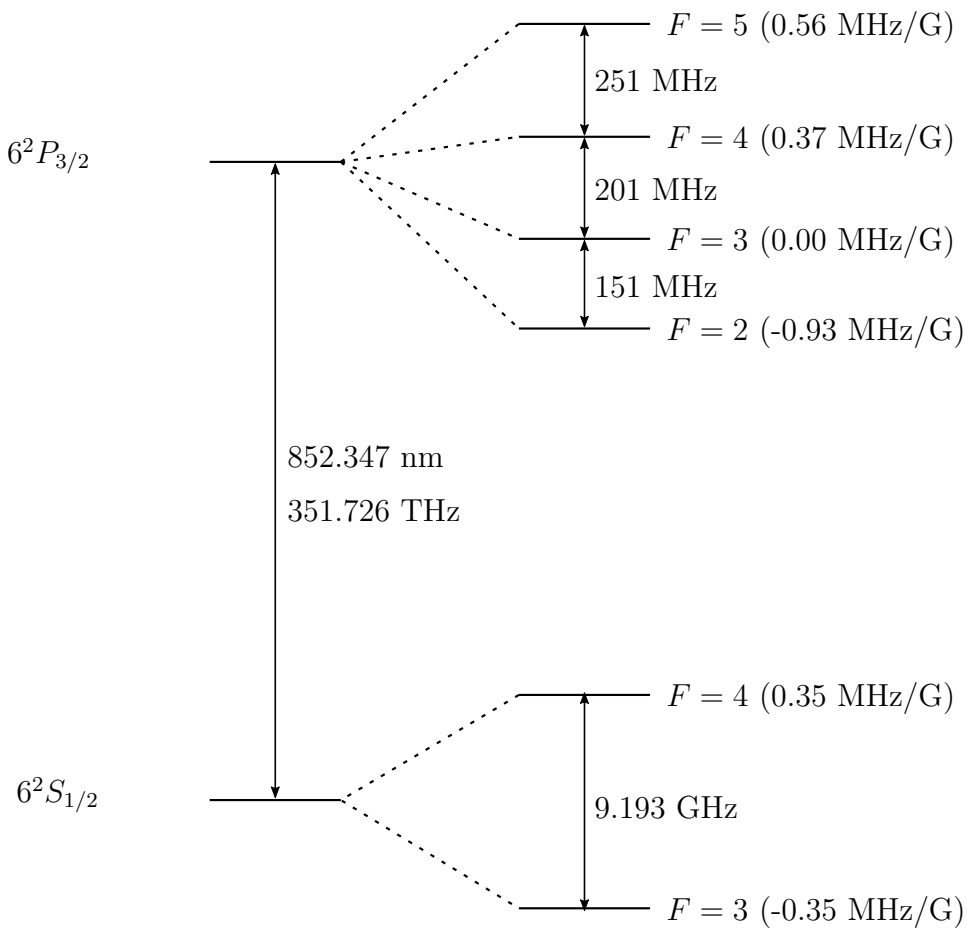

Figure 3.5. Energy level diagram for Cesium's D2 $6^2S_{1/2}$ to $6^2P_{3/2}$ transitions[54] at 852.347 nm (vacuum).

transition detected via a Cesium vapor cell in a pump probe configuration with a New Focus 4002 EOM modulating the phase of the pump beam producing a carrier signal and a pair of weak sidebands at +/- the modulation frequency. When the probe beam is aligned co-propagating to the pump beam, a four wave mixing process will occur for the probe beam when sub Doppler conditions are met resulting modulation transfer of a pair of sidebands. The signal can be detected and locked via monitoring the beat note of the probe carrier and sidebands on an RF photo-diode.

The DBR laser outputs approximately 150mW near 852.356nm and is stabilized via a commercial offset phase lock servo (OPLS) from Vescent Photonics using a beat-note signal produced by the DBR and a pick off beam form the reference laser that has passed through a second order double pass, shifting the frequency by +400MHz. The OPLS has an offset range of 10 GHz and a 100μs settling time allowing for rapidly switching wavelengths for different processes during the experiment. The DBR light is split into an imaging path and a seed path for the MOT light that is fed into the TA

The repumper outputs approximately 30mW of light near Cesium's D2 $F = 3 \rightarrow F = 4$ transition at 852.335nm The repumper is offset locked to the reference laser via another OPLL using an RF photo-diode to monitor a beat-note signal from the two beams. Repump light is used to prevent atoms from accumulating in the F=3 ground state that is dark to our main science beams. The repumper is split into a path used for imaging and another seed path for the TA.

The boosTA is input overlapping beams from the DBR and repumper beams and outputs an amplified mixture of the two beams at approximately 1W. Aligning the TA is quite tricky, one beam is initially aligned onto TA chip by maximizing transmitted power and beam mode. After the first beam has been power optimized it is then fiber coupled to one of the experiment stages downstream such that when the subsequent second beam is aligned for power, it can aligned and optimized using the fiber coupled beam guaranteeing true spatial mode overlap of both input beams. Light from the TA is split into multiple paths via wave plates and

PBS followed by AOM's allowing for individual control of light for the initial Source MOT, Science MOT, mini-mot, push beam used to shuttle atoms between the source and science chamber, and florescence imaging.

3.1.3 Tweezer Beam

A SolsTiS PSX-XF Ti-Saph laser system form M Squared is used to generate light for our optical tweezer beams. The Ti-Saph is pumped by a Lighthouse photonics Sprout-H outputting 12W of green 532nm light. The solstice generates about 5W of light with a wavelength tunable from 700-1000nm, and can be locked to a linewidth of less than 100kHz via an internal calibrated etalon. During our experiment the tweezer beams are run at 935nm, which is the "magic-wavelength" for Cesium's D2 transitions in which the cumulative sum of the light shifts induced on Cesium's $6^2P_{3/2}$ states from all possible induced transitions are almost identical, resulting in near zero differential light shift for the hyperfine sub-states. This effect prevents an otherwise intensity dependent light shift of the resonant frequency for Cesium's D2 transitions that will vary spatially in the tweezer traps resulting in our atoms seeing a different detuning for our trapping and cooling beams. Light from the Ti-Saph is fiber coupled into two paths, one for the top tweezer array and one for the 'bottom beam' we use to increase atom loading rate and implement optical conveyoring.

The optical tweezers are focused onto the surface of our photonic chip b y sending light from the backside of an OD14720C3 infinity corrected microscope objective with a working distance of 20mm and a numerical aperture of 0.35. The tweezer beam is steered by two Isomet 1205c-2-804B AOD's (X and Y) placed in the beam path prior to entering the microscope objective. The tweezer system can be used to generate trapping arrays of up to 10 spots with $\sim 0.8\ \mu m$ spot sizes that can be steered tens of microns on the surface of our photonic chips, allowing for localizing atoms at specific locations above a given micro ring resonator for controllable propagation phases for photon exchanges between atoms.

3.2 Vacuum Chamber

To trap and cool individual atoms and interface them with photonic structures requires the use of an UHV environment with sufficient optical access for all of our relevant trapping, cooling, state manipulation, and imaging beams and sufficiently low pressure to minimizing background collisions interfering with a given experimental run. Our vacuum system consists of three main regions, a source chamber for initially trapping and cooling atoms emitted from a heated Cesium sample, the main Science chamber where our photonic chips are docked into an X-Y-R translation/rotation stage and relevant lasers are aligned unto for trapping and cooling Cesium atoms, and a load lock chamber which allows for rapid installation and removal of our photonic chips from the science chamber without exposing it to atmosphere, and .

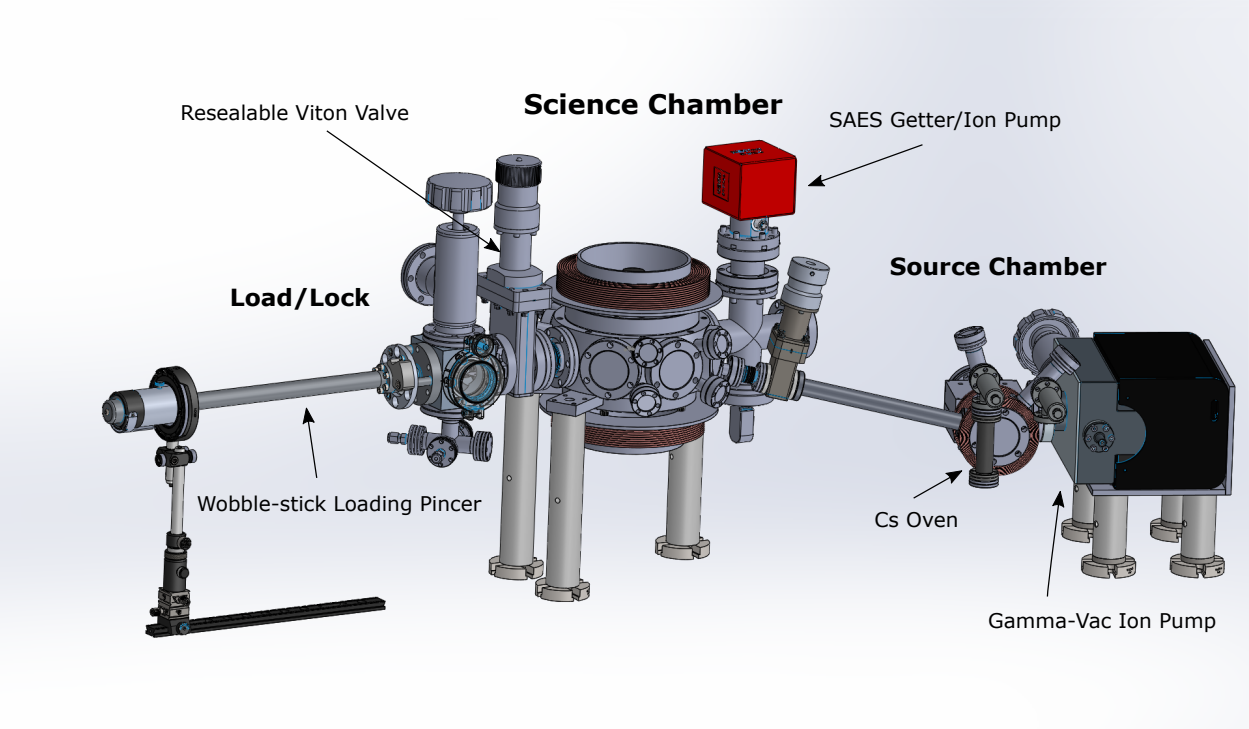

Figure 3.6. Solidworks rendering of our vacuum chamber system. We utilize a three chamber setup consisting of a source chamber where atoms from a cesium oven source are collected and cooled, a science chamber containing an electronic translation stage where our photonic chip is docked, and a load/lock chamber with a wobble-stick loading pincer for transferring chips into and out of the science chamber.

3.2.1 Source Chamber

The source chamber is the starting point for our experiments. A Cesium 'oven' is used to provide a controllable flux of atoms into the vacuum chamber. A long differential pressure tube connects the source chamber to the main science chamber, allowing for high atom fluxes into the source chamber to efficiently collect atoms without substantially effecting the pressure in the science chamber during experiments which would lead to a higher background collision rate.

The Cesium oven consists of a glass cell containing 5.0 grams of 99.95% Cesium (Sigma-Aldrich 239240) placed in a nipple tube connected to a flange on the source chamber. The outside of the Cs oven is surrounded by fiber glass coated heating strip. A 1mm aperture

slows the effusion rate to increase the source lifetime. The oven is turned on and off by control of a heating strip that has an adjustable current driven by a Variac. A Gamma Vacuum Titan 45S ion pump is used to maintain pressures of approximately $7.0x10^{-9}$ torr inside the source chamber. A cold trap consisting of a water cooled TEC separates the chamber and the flange connecting to the Ion pump reducing the pressure and elongating the lifetime of the ion pump.

Inside the source chamber a MOT is formed at the center of the chamber by 3 retro-reflected beam pairs and a series of Helmholtz coils used to generate the appropriate magnetic fields and is used to initially collect atoms and cool atoms from the Cs oven. For typical experiments atoms are collected in the source mot for approximately 600ms before a push beam is pulsed on that transfers them through the differential pressure tube into the science chamber via radiation pressure.

3.2.2 Science Chamber

The science chamber is a custom Kimball Physics MCF600 spherical octagon chamber, with 10 1.33',8 2.75" and 2 6.00" CF flanges, most of which are mounted with view ports providing optical access to the chamber for trapping, cooling, state manipulation, and imaging. The view-ports are fused silica made by MPF with a broadband AR coating providing providing a reflectance of less than 0.5% at Cesium's D1 and D2 wavelengths. The top view-port is a custom recessed window, Q8167-1 with a 1.8" diameter window allowing us to locate our microscope objective as close to the center of the chamber as possible to achieve sufficiently high NA for imaging and tweezers.

An electronic translation stage is mounted in the center of our chamber for docking our photonic chips. The stage consists of two Q-522.00U linear UHV translation stages with 6.5mm of travel (x and y) and a Q-622.90U rotary stage produced by Physik Instruments. The stages are driven by a E-870.4G PIShift drive electronics, controlled via USB. The XYR stage is mounted via Kimball Physics groove grabbers such that rotary arms default

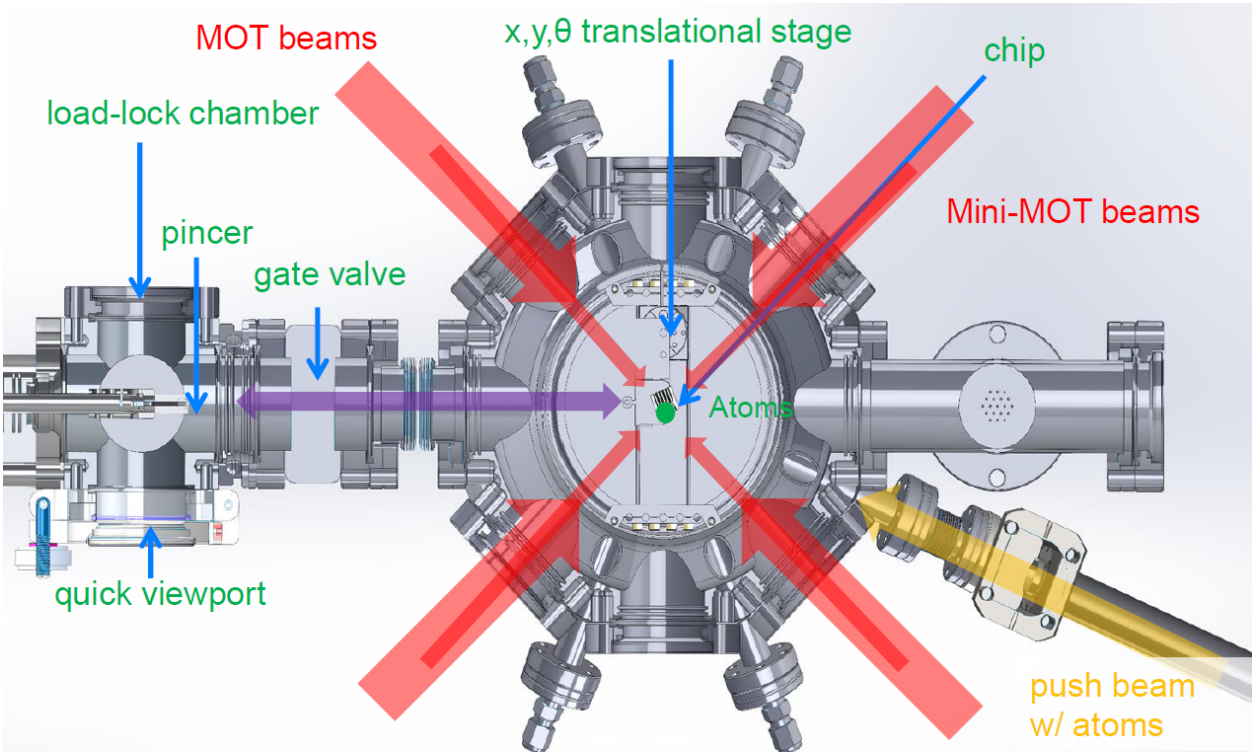

Figure 3.7. Science Chamber Experimental Schematic. Photonic chip is loaded into science chamber from the load/lock chamber via wobblestick pincer (purple path) and docked into the x, y, θ electronic translation stage in the center. Cesium atoms (green) are pushed into science chamber from the source chamber via a radiation pressure 'push beam' and collected into a large 'science MOT' formed by three pairs of retro-reflected 1" beam aligned near the center of the chamber. Additional set of three 1mm retro-reflected 'mini MOT' beams passing through the window and aligned onto the target micro-ring resonator.

positions is at the center of the chamber. Due to geometry constraints of our chamber and the wobblestick pincer, the translation/rotation stages have to be actively adjusted during the final docking stages to provide sufficient vertical clearance for the top of the pincer during the docking procedure. In addition, once a chip is loaded in the chamber, aligning the mini-mot beam's relative to the chip using their respective mirrors can be very challenging and tedious. Once a good mini-MOT cloud is achieved above the window it can be easier to align the chip to the atoms for small displacements. We shifted more emphasis towards this method as the motors have reproduce-able stepping motions that can be undone while adjusting mini-mot beam tilt via the mirrors can take days to reproduce.

An SAES NEXTorr D 100-5 getter+Ion pump is used to maintain UHV pressure in the science chamber, typically down to $10^{-}11$torr. The getter pump consists of a stack sintered extremely porous zirconium graphite "getter" disks absorbing gases that pass through them. The device is activated during a heating cycle to remove any absorbed materials while the vacuum system is externally pumped. If the chamber is to be reopened and exposed to atmosphere the getters can be reactivated by performing another heated de-absorption cycle, but the device does has a finite number of times that this can be performed without degrading the getters performance substantially so exposure to atmosphere should be limited to absolute must need cases. Flushing the chamber with nitrogen allows for the getters to be reactivated more readily and should be done anytime the chamber is to be opened as it is more easily de-absorbed than oxygen.

As a side note for adjusting mini-MOT beam alignments when recovering or moving the trapping location, heating from the main MOT coils will shift the chamber temperature slightly if the experiment has been turned off prior to use, it is suspected this may lead to very small amount of thermal expansion. While this effect is minuscule and not detectable for free space experiments or the 1" science-MOT beams, it may influence the the optical fields of the mini-MOT a few microns from the surface so be sure the experiment is either left

operating overnight or at least 2 hours prior to ensure thermal equilibrium before adjusting the mini-MOT beam alignment relative to the chip.

3.2.3 Load Lock Chamber

In addition to the UHV requirements of a typical cold atom experiment our vacuum system has to facilitate the installation and removal of photonic chips from the science chamber while minimizing it's exposure to atmosphere which can contaminate the chamber and raise vacuum pressure. This is achieved by the addition of a separate chamber connected to the science chamber that can be vented and opened to facilitate chip transfer without perturbing the science chamber.

The loading (or load/lock) chamber is connected to the science chamber via a resealable gate valve (MDC 302011), capable of sustaining vacuum of $10^{-}11$ torr while one side is open to atmosphere. The chamber can be opened and closed very easily via a resealable window port (MDC quick Door 665215) allowing for sufficient access to transfer photonic chips into and out of the chamber. The chip transfer itself is facilitated by a wobble-stick loading pincer (Kurt J Lesker WSRLF-250-H) which hold onto the the photonic chip carrier via a mating grove. The wobble-stick has an retractable arm which can be extended into the center of the science chamber

3.3 Chip Transfer Procedure

Loading a photonic chips into the vacuum chamber represents the culmination of our chip development process where we may be utilizing a chip which took our colleagues months to fabricate. Unfortunately due to physical constraints imposed by the vacuum system, physical access is limited and the loading process can be challenging. During the chip transfer process there is a very serious risk of damaging the chip while entering the science chamber, having fibers from the chip carrier break off in the chamber preventing our load lock from resealing, and a worst case scenario of dropping a chip in the main science chamber potentially creating

debris that obstructs optical access to the chip which may require a full science chamber disassembly setting us back several months. Through several trials with 'practice' mock up photonic chips we have developed a chip transfer procedure to mitigate several of these risks.

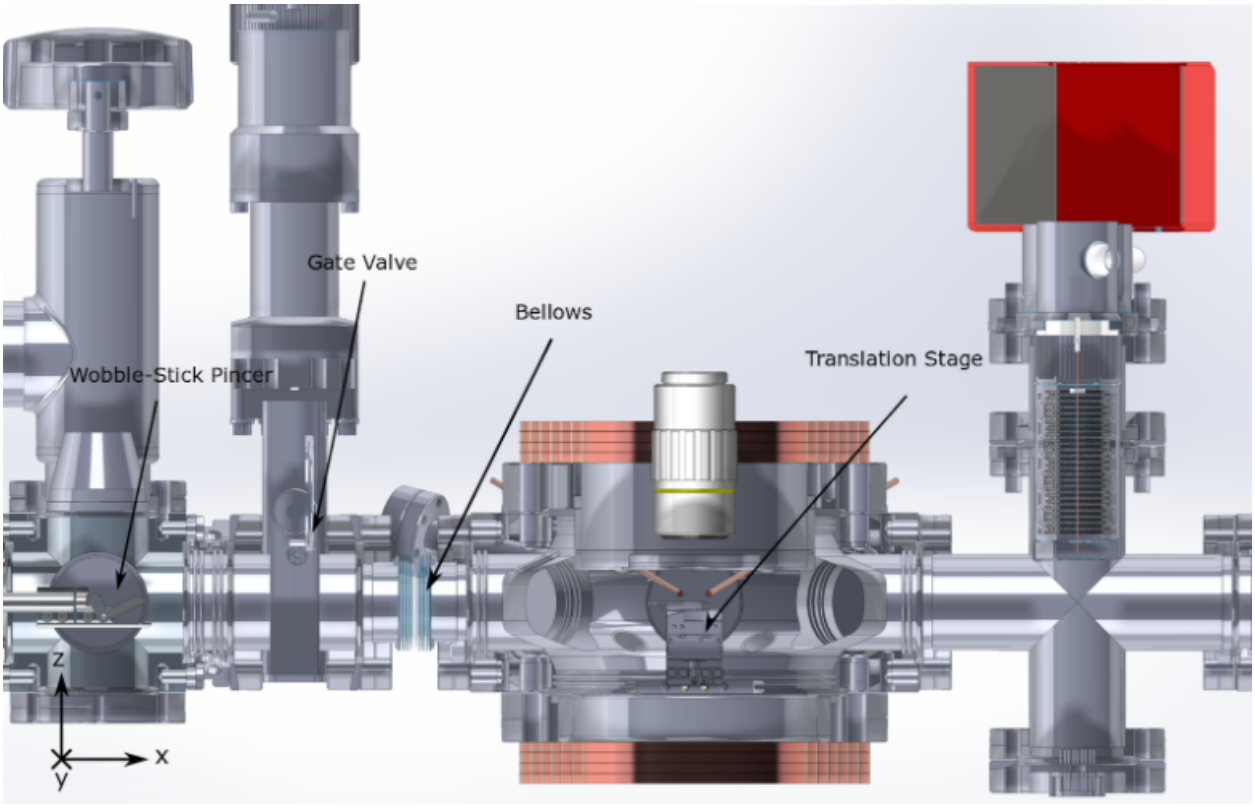

Figure 3.8. Cross sectional internal view of loading chamber and science chamber with wobble-stick pincer and chip docking transnational stage

3.3.1 Preparation

At least one day before attempting a chip transfer the chip, chip carrier, and fibers must be prepared. The chip must first be attached to the peek chip carrier using EPO-TEK OG198-54 UHV compatible epoxy. Much work has been done to develop the curing scheme for the epoxy to prevent out-gassing and possible misalignment insitu, this step should only be done by a team member trained and up to date on the current procedure as this is actively being improved. After curing, the input/output optical fibers should be cut approximately 18" and marked at exactly the 12" point which is the distance from the fiber feed through

in the load-lock chamber to the translation stage at the center of the chamber with the slack allowing for splicing of the fiber leads outside of the feed-through. Once dried the chip carrier and fiber should fixed to a UHV aluminum foil tray using strain release straps made form kapton tape.

If a chip is currently present in the chamber, record it's position for realignment with the new chip by taking images using the absorption imaging CCD camera from both views. If the chamber is empty or after the previous chip has been retrieved, the rotation stage should be rotated 90 degree clockwise to the -x direction to provide room for the chip to move into the science chamber. Physik Instruments UI software is used to control the translation stage. Channel one controls rotation left arrow is clockwise right is counterclockwise, Channel two controls x position left is +x right is -x. The third controls y motion, left is +y right is -y. The motor should be set to 100 steps per click, too large of a step can jolt the chip carrier out of the translation stage arm.

Connect the turbo pump to the right angle bakeable valve at the bottom of the load lock chamber, with a 15-20 psi nitrogen line connected to the turbo pumps vent valve initially closed. Before flushing the load lock with nitrogen, partially open and close the load lock to inspect for fiber debris that may prevent a seal, then fully close the device. Next seal the source chambers valve along the differential pressure tube as well as the Cesium source's valve . Begin flushing the load lock chamber with nitrogen. First open the turbo pumps vent valve allowing nitrogen to flow into the arm. Next while monitoring the pressure in the load lock and science chambers, open the right angle bakeable valve slowly to ensure there is no leak into the science chamber. Finally fully open the valve and allow the load lock chamber to vent.

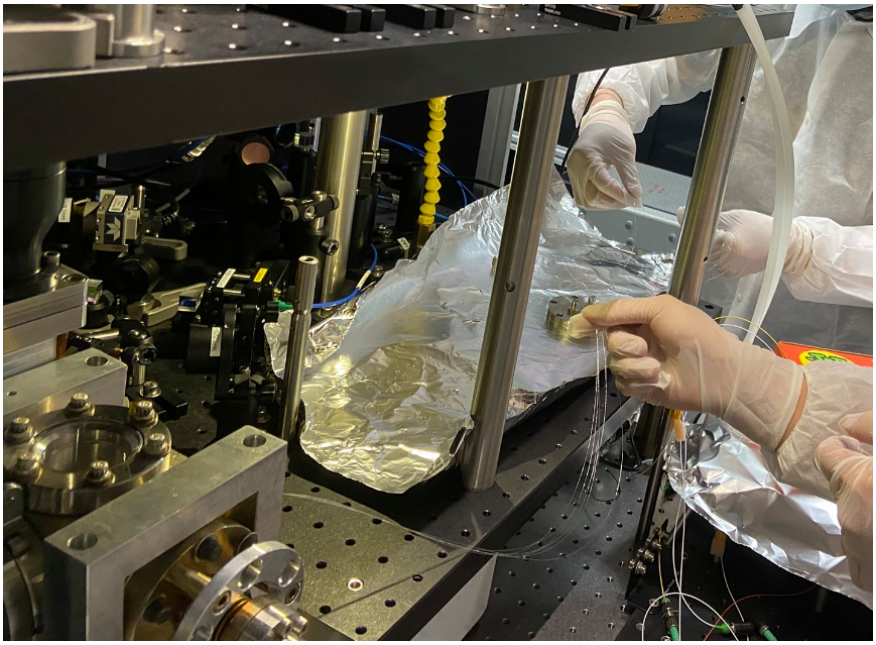

(a)

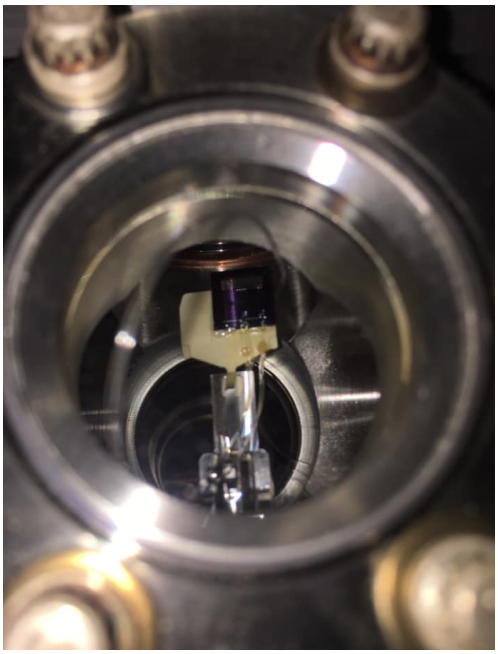

(b)

Figure 3.9. Loading chip into wobble-stick pincer. The chip carrier dibbut should be secured flush in the holder slot of the wobble-stick pincer ensuring snug fitting such that the carrier does not come loose during installation. a) The chip fibers are fed through a Teflon feed-through allowing connections in and out of the chamber. b) Top view of a securely positioned held by the wobble-stick pincer. During installation it can difficult to see through the top view-port of the load/lock while holding the chip carrier in plastic tweezers, using a smartphone or an additional viewracam process more manageable

3.3.2 Pincer Loading

Once ventilation is complete the previous chip can be removed from the pincers. First loosen the swagelok seal holding the teflon fiber feed through. Remove the teflon fiber feed-through freeing the unattached ends. If the feed-through is crimped too strong on the previous fibers it may be cut with scissors to remove. The old chip is now ready to be removed, position the empty tray next to the load lock to place the old device on. Grab the edge of the chip carrier using one of the pairs of plastic tweezers, the plastic tweezers will be somewhat slippery on the carrier so be sure to use sufficient force applied to a safe location that will no effect the chip. Once the chip is securely gripped, slowly open the pincer while carefully ensuring the chip carrier does not slip in the tweezer as tension in the fibers may cause the device to shift. The chip carrier is held in place in a dibbut inside the pincer, it should easily pop out of the pincer by pulling it upward. Transfer the old chip to the aluminum foil tray and wind up any excess fiber, once the ends of the fibers have exited the chamber the pincer can be closed. Tape down a strain release strap on the fibers near the old chip carrier to ensure the chip is safely secured to the tray, then move to the clean room. Next remove the fiber feedthrough adapter exposing the 1.33" flange to allow the new fibers to be passed through.

Bring the tray containing the new chip in proximity to the loading window. Ideally the loading process will use three people, one securing the holder tray itself, one person for the chip and one person for the fibers. The first step is to pass the fibers through the loadlock to the opposite side to be passed through to the fiber feed-through. Remove any strain strap present on the fiber tail while leaving the chip secured to the transfer tray. Have one person use a pair of tweezers to grab the fiber ends and pass them through to the load lock chamber to another person on the opposite side also using a pair of tweezers. While this happens the tray will have to be brought closer and closer to the chamber, it may be required to fold the half of the tray opposite to the chip carrier. Run a new gasket and the adapter over the fiber

and reseal them. Next pass the fibers through the teflon feed-through and pull the excess slack until the feed-through is at the measured 14" marks. Close off the feed-through and hand tighten the swagelok flange.

Secure the chip carrier with a pair of plastic tweezers before removing the remaining strain release straps. With one hand securely holding the chip carrier move it approximately 2" from the entrance port, with a second pair of plastic tweezers slowly coil the remaining fiber into the load lock chamber. Manipulate the fiber such that all of the windings are to the right side of the pincer. Finally move the chip carrier into the chamber, squeeze the wobble-stick trigger to open the pincers then securely place the chip carrier dibbut in the pincer slot. If you cannot see the pincer clearly through the top window a camera phone with zoom may be placed on top for viewing. Ensure the chip carrier dibbut is 100% in the slot, the top of the chip carrier dibbut should be flush with the pincer base. Close the tweezers and inspect again to ensure the fibers are not crossed over the wobble-stick and that the carrier dibbut is properly secured.

Close the window port and hand tighten the seal, double check that the swagelok connector is hand tightened and the adapter has been properly hand tightened then use a wrench to tighten an additional 1/4 turn. Place a folded piece of rubber under the wobble-stick trigger to prevent it from accidentally being pressed open. Close off the turbo pumps vent valve completely then turn on the turbo pump. The pressure should drop down to about 10 hPa in a matter of 2-3 minutes, then rapidly decreased to $10^{-3} - 10^{-4}$hPa range. Using your hand tighten the window ports valve and the swagelok feed-through. As the pump operates iteratively tighted the teflon feedthrough with a wrench in small 1/16th to 1/8th rotations. Wait another 10-15 minutes to ensure the pressure drops down to the low 10^{-5} hPa range, at which point it is safe to allow the pump to run overnight. If the pressure does not reduce as expected and the source of the leak cannot be found in 10-15 minutes the turbo pump must be turned off to prevent damage. After the turbo pump comes to a stop re-flush the chamber

with nitrogen and reinspect vacuum seals and repeat. The next day when the pressure is low enough turn on the gate valve side ion pump

3.3.3 Chip Loading and Retrieval

When the pressure is low enough the gate valve can be reopened. Focus the axial camera on the pincer edge of the wobble-stick. Loosen the cart, wobble-stick position locking screw and vertical movement post such that the wobble-stick may be freely manipulated. The chip carrier will have to be moved through the gate valve, the bellows and into the science chamber for docking. To move the wobble-stick forward use one hand to push the cart base and one on the wobble-stick handle far away from the release trigger. The bellows are vertically bent down about 1cm, as the pincer passes through this region the pincer will have to be lowered by using the wobble stick vertical control (raising the handle end tilts the pincers downward.) As you move forward the main focus should be on ensuring the chip itself does not touch and of the walls, the pincer itself can be positioned slightly off-center horizontally to leave more room between the chip and the wall. Continually move forward and lower while passing through the bellows.

Once in the science chamber raise the pincer until the top touches or nearly touches the top of the chamber, then move the stick into the -y direction to provide room for the translation stage arm. Rotate the arm to about 20 degrees from the -y axis and recenter the pincer. When raised fully the chip carrier will be able to clear the translation stage arm but the base of the pincer will still bump into the arm. Begin moving the chip towards the translation stage until the pincer base is almost in contact. The first step in the docking process is top place the -x +y corner of the chip carrier into the upper docking groove in the translation stage arm. Incrementally rotate the arm forward and move the pincer forward. The pincer should be lowered until the chip carrier is touching the arm. Slightly Rotating the wobble-stick to tilt down the +y side of the chip carrier if necessary. Once there is space to dock the -x+y corner of the chip, rotate the wobble-stick again to ensure the chip carrier

in horizontal. Continue incrementally rotating the translation stage and moving the pincer forward until the -x-y corner of the chip carrier is docked.

When the chip carrier is secured into the translation stage slowly open the pincers and lower them to release the chip carrier. Do not let the pincers close immediately, slowly back the wobble-stick up in the -x direction and bend to the +y direction. Ensure that no fibers are caught in the pincer then slowly close the pincers. Slowly return the pincer to the load lock chamber lowering and raising to traverse the belows as mentioned prior . If removing an old chip chip first, move the wobble-stick into the chamber, and slowly grab the chip dibbut with the pincer. Slowly reverse the docking steps rotating the arm backwards and moving the pincer until the arm is about 10 degrees. Move the pincer forward and raise the chip carrier vertically above the arm then retrieve. It is very likely that the pincer will not perfectly grip the dibbut and the chip carrier will be tilted at some angle. Do not panic or attempt to re-dock and regrab the dibbut as the chance of making things worse is much higher than getting a perfect grab on the chip carrier. If angled the chip can still safely be removed but be very cautious while moving the pincer back to the load lock chamber as any fiber stress or bumping against the bellows may free the chip from the pincers.

When the wobble-stick is returned to the load lock chamber turn on the imaging program and reposition the arm such that the window is in the same location and orientation as the previous chip. When moving the stage first ensure with the vertical camera that the chip carrier does not move from inside the holder on the arm. If the chip comes loose, as mentioned before you will most likely not be able to re-grab the chip carrier and have the dibbut seated correctly in the indent introducing an angle. After previous failures it was determined safer to retrieve the chip to the load lock chamber and correctly re-seat the chip carrier in the pincers instead of trying to re-dock with the chip carrier not securely in the pincers.

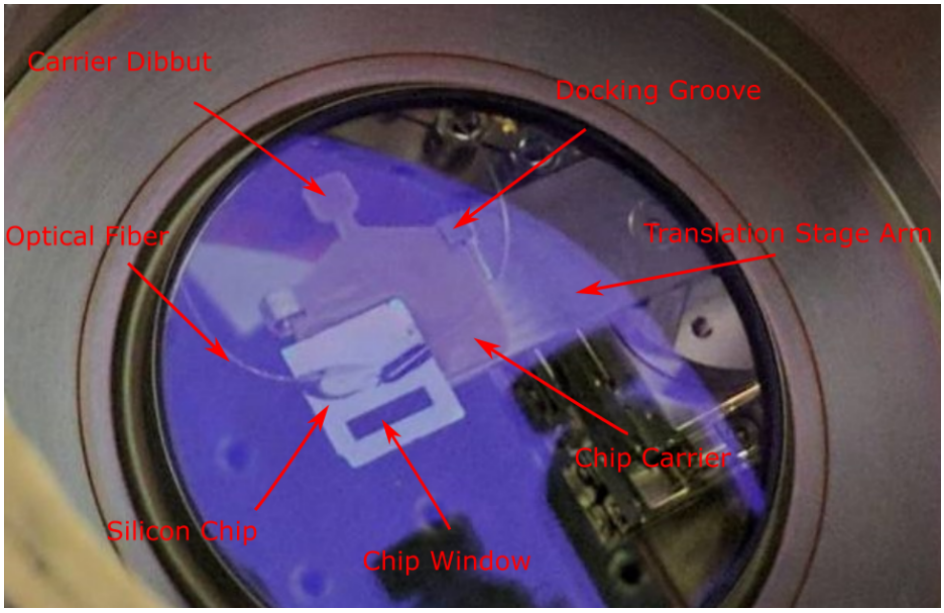

Figure 3.10. Science chamber top view-port image of a successfully docked 'dummy' photonic chip. Silicon photonic chip epoxied atop a PEEK UHV plastic chip carrier with corner dibbuts for docking into the groves of the translation stage arm and a carrier dibbut for temporary mounting inside the wobble-stick pincer

3.4 MOT

In order to load atoms into a tweezer trapping potential above the micro-ring resonator we need to prepare a dense atomic cloud in close proximity to the surface of the chip. Our setup implements three sequential MOT's and two transfer procedures to localize items in the vicinity of the structure. To begin, atoms are loaded into a MOT in the source chamber, collecting and cooling atoms emitted from a heated Cesium cell capped by a diaphragm creating a continuous flux of atoms into the source chamber. At the start of the experiment a near resonant radiation pressure "push beam" passing through the source mot and the differential pressure tube into the science chamber transferring a few million atoms per cycle.

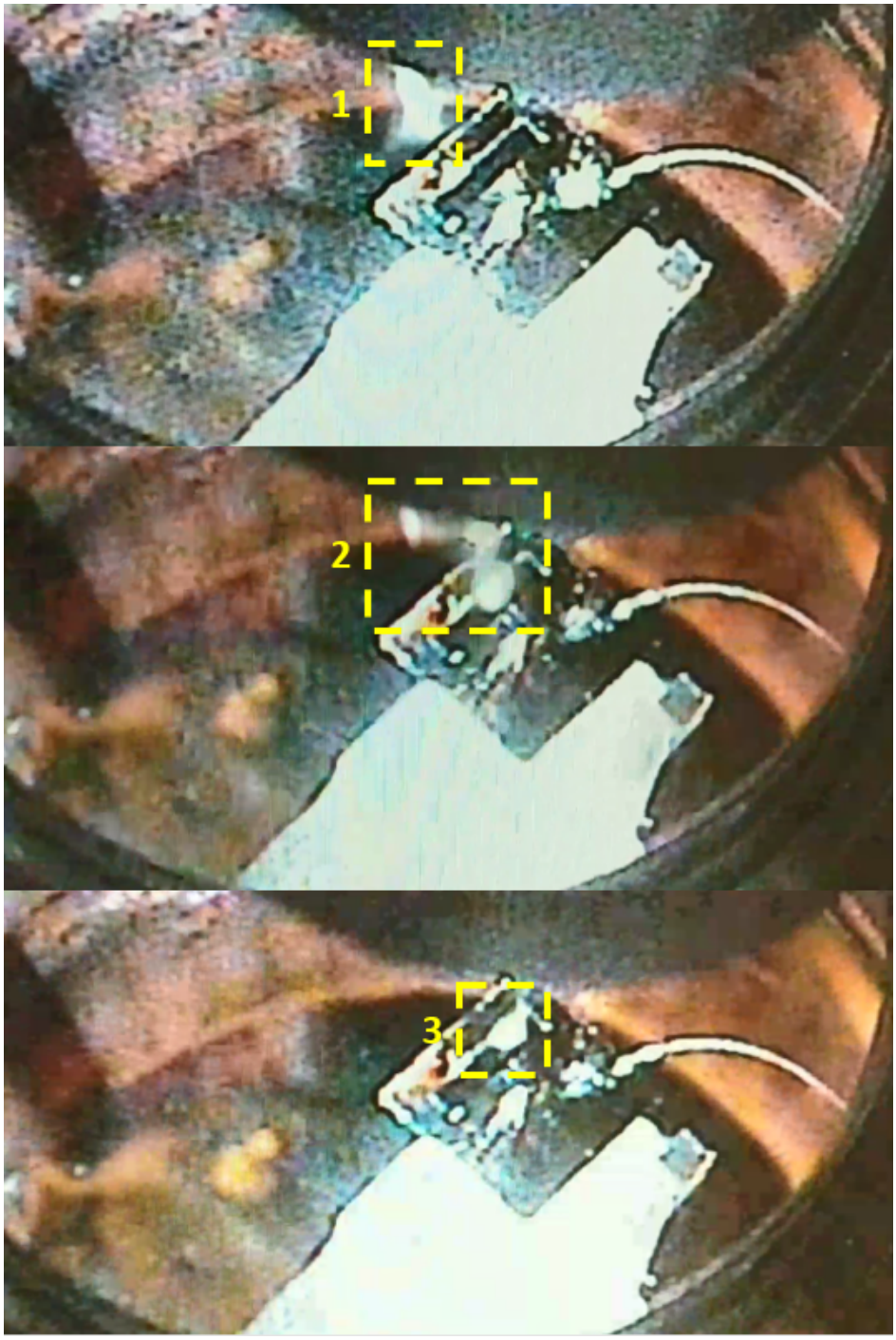

Figure 3.11. Atoms initially trapped in the science MOT are transferred above the micro-ring resonator in a three step process. The vertical magnetic field bias is increased raising the cloud above the chip, followed by velocity selective cooling which imparts a momentum kick downwards and to the target micro-ring resonator where atoms are captured by the mini-mot trap made from 3 retro-reflected pairs of smaller 1mm beams passing through the window.

Inside the science chamber the atoms pushed from the source chamber are collected into a large secondary 'science MOT' produced by three retro-reflected ∼1" beams. Typically ∼ 1-2 million atoms are trapped and cooled to an initial temperature of about $40\mu K$. Due to the geometry of the chamber and the angle of the differential pumping tube, atoms entering the science chamber do not have a clear trajectory to their desired location directly above the chip surface as the chip is located vertically higher than the source MOT center. To manage this, the 'science' mot is first positioned a few mm higher and in front of the chip in the +x direction from target trapping location above the micro-ring.

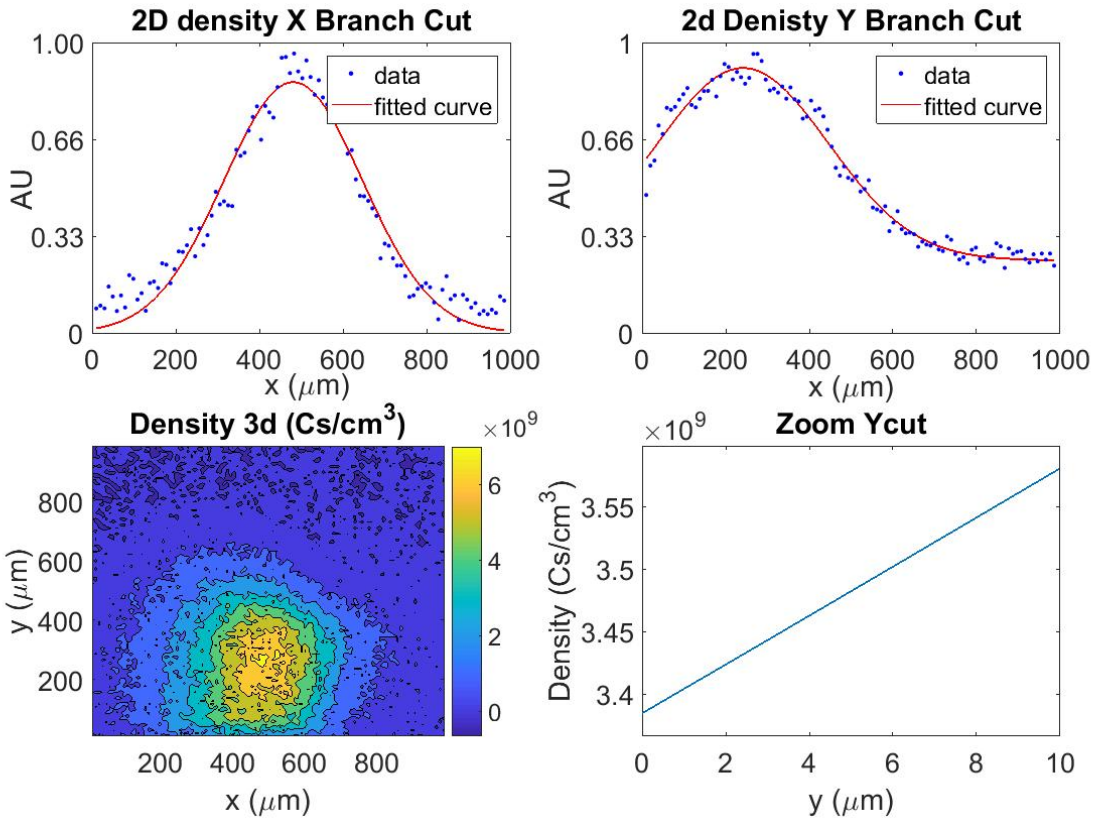

Figure 3.12. Mini-MOT Absorption images taken from our horizontal view ccd were used to the 2D density of the mini-MOT cloud. In image atoms are trapped directly above our photonic chip lying in the X-Z plane at Y=0. a,b) X and Y axes branch cuts were taken through the peak density region of the cloud and fit to Gaussians to extract the width and height of the cloud above the chip surface. c)The average 3D density of the cloud was calculated by approximating the width of the Z-axis ∼ X axis d) Zoom in of peak 3D density near the chip surface

After collecting atoms from the source chamber for about 500 ms a second transfer process is begun to localize atoms above the photonic-chip window. The secondary transfer begins by first increasing the vertical magnetic field offset raising the cloud position. Next a velocity selective cooling process[58][59] is used in which the atoms are shuttled in a direction determined by an integer multiple of photon exchanges form the MOT beams, tuned to "shoot" the atoms towards the target micro-ring resonator in the window. During this step, a third set of smaller, 1 mm diameter retro-reflected "mini-mot beams" are used to collect the transferred atoms in a mot centered approximately 100-200 microns above the surface of the chip with densities approaching 10^{10} atoms/cm^3.

3.5 Imaging

We have four separate imaging pathways incorporated into our apparatus for detecting atoms at different stages in the experiment. We have the ability to perform either vertical or horizontal absorption imaging using 2 pairs of retro-reflected near D2 resonant beams and one of two separate CCD cameras allowing us to view the sciene MOT or mini-MOT cloud distributions relative to the chip and calculate the total atom number and distribution in the XY and XZ planes. For imaging individual atoms we use a microscope objective and an EMCCD to collect light from trapped atoms illuminated from either a near vertical or near horizontal pair of retro-reflected resonant fluorescent imaging beams.

3.5.1 Absorption Imaging

Absorption imaging[60] is performed by shining resonant light onto a gas sample and imaging the shadow cast by the atoms. Resonant light traveling through a sample gas will be absorbed and scattered out of the incoming beam resulting in an attenuation of the incoming beam following Beer's law,

$$\frac{dI}{dz} = n(x,y,z) - \sigma I \tag{3.1}$$

$$\frac{I_t(x,y)}{I_0(x,y)} = \mathrm{e}^{-\sigma \int n(x,y,z)dz} = \mathrm{e}^{-\sigma n_{2d}(x,y)} = \mathrm{e}^{-OD} \tag{3.2}$$

$$\sigma = \frac{\sigma_0}{1 + 4(\Delta/\Gamma)^2 + (I/I_{sat})} \tag{3.3}$$

where n(x,y,z) is the density of the gas, n_{2d} is the two dimensional "column density" of the atom, OD is the optical density, σ is the power broadened absorption cross section, and $\sigma_0 = 3\lambda^2/2\pi$ is the resonant absorption cross section. The transmitted and incident intensities are measured on a CCD camera by taking one image with the sample present and one without. Additional background noise from dark current and other sources is subtracted off by taking a reference image at the beginning of the experiment with no imaging light present. The imaging process is destructive and is performed within a few ms of releasing the MOT.

The horizontal absorption imaging is perform using a Teledyne Dalsa - Genie Nano M2020 CCD camera with 2048x1536 resolution and a pixel size of $3.45\mu m$ x $3.45\mu m$ The imaging path to the camera has a magnification of 0.35. The Vertical absorption imaging path utilizes a Point Grey CM3-U3013S3M-CD camera with 1288x964 resolution and a pixel size of $3.75\mu m$ x $3.75\mu m$ and an imaging path magnification of 0.55

3.5.2 Fluorescent Imaging

Fluorescent imaging is performed by illuminating the trapped atoms with light near resonant with Cesium $F = 4 \rightarrow F = 5$ D2 transition and $F = 3 \rightarrow F = 4$ repumper light. Light is collected using the OD14720C3 microscope objective. The objective forms an image onto a Princeton Instruments ProEM512 EMCCD with a resolution of 512 X 512 pixels,

pixel size of 16μm x 16μm, and a quantum efficiency of approximately 65% at Cesium's D2 wavelength.

Three optical band-pass filters near Cesium's D2 transition at 852nm are installed to prevent high intensity light reflected light from the optical tweezers from saturating the EMCCD. In addition stray light scattered from the surface of our photonic structures may scatter into the microscope objective drowning out the light emitted by an atom, to get around this the polarization of the input fluorescence imaging light is tuned relative to the surface of the chip to minimize reflection and a HWP QWP pair after the microscope object followed by a PBS are used to filter the polarized light scattered from the surface while half of the un-polarized light emitted from a target atom passes through to the EMCCD for detection.

3.6 Microwaves

Beyond optical control of Cesium's internal state, we also implement a microwave source to directly drive the magnetic dipole transition between Cesium's $6^2S_{1/2}$ F=3 and F=4 hyperfine ground states. Microwave are generated via frequency mixing the output of an AD4159 and a novatech DDS. The microwave signal is amplified up to 3W by a minicircuits ZVE-3W-183+ amplifier before being emitted towards the center of the chamber via a pasterneck PE9856/SF-10 microwave horn. Microwave's offer the simplicity of directly driving transitions that would otherwise require two well aligned Raman beams with an OPLL, but the downside is due to the larger wavelength and poor directionality of the source, the horn will emit waves that nearly uniformly reach all of the atoms in the chamber.

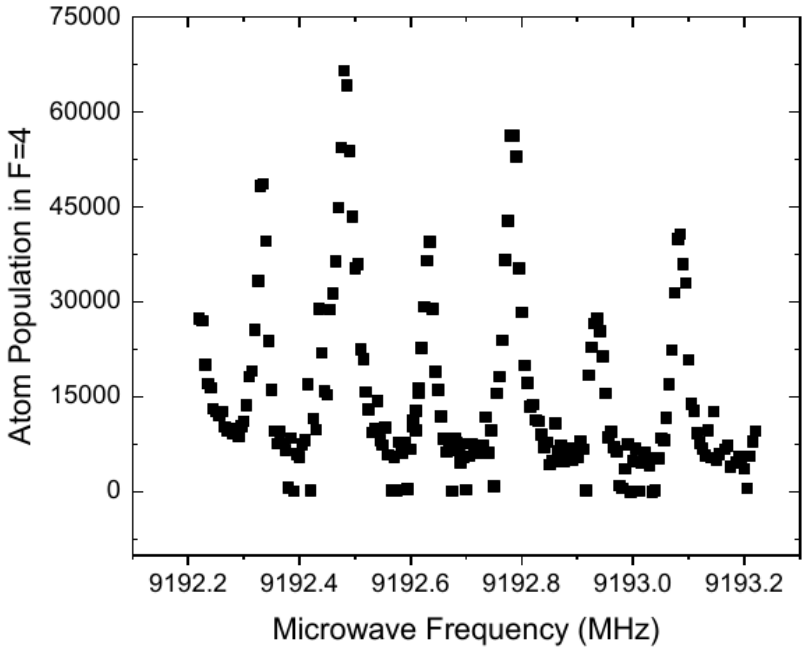

Figure 3.13. Microwave scan for MOT cloud during magnetic field calibration. Repumper light is removed from the mot beams, causing population to accumulate in the F=3 manifold followed by microwave π pulse and state detection using light resonant with the 4-5 transition. The clock transition from $|F = 3, m_F = 0\rangle \rightarrow |F = 4, m_F = 0\rangle$ is present at 9.193Ghz, surrounded by neighboring peaks shifted by the Zeeman interaction from a non-zeroed magnetic field

3.7 Magnetic Field Control

3.7.1 Helmholtz Coils

The magnetic fields used to create our Science MOT is generated by a pair of Helmholtz coils[61][62] fixed on the top and bottom of the chamber. A Helmholtz pair consists of two circular coil windings with N turns of radius R, aligned coaxially, each a vertical distance H from the center of the chamber. When both coils have current I flowing in the same direction (both clockwise or both counter clockwise) it is refereed to as the Helmholtz configuration. Starting with the field. For coils located at $z = \pm H$ axially, the resultant field at the center of the chamber (z=0) will be given as

The magnetic field for a Helmholtz pair can be calculated by beginning with the magnetic field on axis for a current I traveling through a single circular loop of radius R as a function of the on axis vertical displacement from the center of the coil (z) using Biot-Savart law, yielding

$$\vec{B_1}(z) = \frac{\mu_0 I R^2}{2(R^2 + z^2)^{3/2}}\hat{z} \tag{3.4}$$

For the case of a coil with N windings assuming a small wire diameter compared to coil radius the field simply increases by a factor of N. A pair of such coils aligned in the Helmholtz configuration separated a height H=R can be shown to produce magnetic field $\vec{B_{tot}}(z)$,

$$\vec{B}_{tot}(z) = \vec{B}_{top}(z) + \vec{B}_{bot}(z) \tag{3.5}$$

$$\vec{B}_{tot}(z) = \frac{N\mu_0 I R^2}{2(R^2 + (z - R/2)^2)^{3/2}}\hat{z} + \frac{N\mu_0 I R^2}{2(R^2 + (z + R/2)^2)^{3/2}}\hat{z} \tag{3.6}$$

$$\vec{B}_{tot}(z) \approx \frac{N\mu_0 I R^2}{(5R^2/4)^{3/2}}[1 + \frac{6z^4}{5R^4} + ...]\hat{z} \approx \frac{N\mu_0 I R^2}{(5R^2/4)^{3/2}}\hat{z} \tag{3.7}$$

where z is now defined as the axial displacement from the center point between the pair of coils and in the final line the resulting field has been expanded in the limit $R >> z$. For our setup radius $R \sim 3$" and vertical displacement from the axial center z is on the order of 100 microns yielding a spatially uniform field up to the 4th order correction which is on the order of a part per ten thousandth and can be safely neglected.

When the coils are driven in opposite directions (one clockwise one counter-clockwise) it is referred to as the anti-Helmholtz configuration which following a similar derivation can be shown to produce a magnetic quadrupole field,

$$\vec{B}(\vec{\rho}, \vec{z}) = \frac{3\mu_0 I N R^2 H}{2(R^2 + H^2)^{5/2}}(\vec{\rho} - 2\vec{z}) \tag{3.8}$$

where $\vec{\rho}$ is the radial displacement vector from the center axis. Crucially, rhe magnetic field of the anti-Helmholtz configuration now has a spatial gradient which is the key ingredient to the operation of MOT scheme.

The Helmholtz coils used for our main 'science MOT' (referred to simply as MOT coils for the vertical direction) consists of 10x9 turns of 12 gauge MWS square magnet wire with MW36-C insulator rated to $200°C$. The coil windings have an inner diameter of 12.9cm, outer diameter of 17cm, and a height of 2.2 cm. The coils are wound around a holder made from a high temperature epoxy, (Epoxy cast 670 HT). The coils were wound by placing the holder in a lathe and hand turning the device, allowing for constant tension. Each row was covered with Loctite stycast 2762 ft bk epoxy to mold the coil in place. Once wound, the coils were clamped taunt and baked in an oven to cure the epoxy. Once cured the coils were mounted concentrically above (below) the main vertical view ports each a distance xxx from the trap center.

In general the coils will be driven with different magnitude currents producing a superposition of Helmholtz and anti-Helmholtz fields allowing for a magnetic field gradient to be produced with an accompanying offset field. In the Helmholtz configuration the MOT coils generate a field of 5.435 $\frac{G}{A}$, in the anti-Helmholtz configurations they generate a field gradient of $1.06\frac{G}{cm \cdot A}$

In addition to the main vertical "MOT coils" there are two additional pairs of smaller "bias" coils run in the Helmholtz configuration to cancel out background fields in the X and Y directions. The X and Y coils consisted 10 rows by 10 turns of 20 AWG copper magnet wire and generate magnetic fields of 0.532 G/A and 0.530G/A respectively.

3.7.2 Coil Driver Circuit

Each coil is controlled by a bidirectional coil driver circuit. The circuit was designed to switch current direction through an inductive load quickly allowing for creation of a stable quadrupole field for MOT operation with the ability to rapidly zero the field gradient for

transfer to optical molasses while applying offset field in either direction. The coil is driven via a single DC Agilent 6673A power supply by utilizing 4 power MOSFETs in an H-bridge configuration.

To understand the coil current direction we can initially treat the power MOSFETs as simple on/off switches (fig 3.13), if the top left and bottom right power MOSFETs are turned on while the top right and bottom left power MOSFETs are turned off, current will pass through the coil in a clockwise direction while the reverse on/off settings will drive a counterclockwise current through the coil. In practice, the very fine analogue current control required for precise magnetic fields and the robustness needed for handling the back EMF associated with rapidly switching currents through an inductive load lead to competing design requirements which took a decent amount of time to tweak.

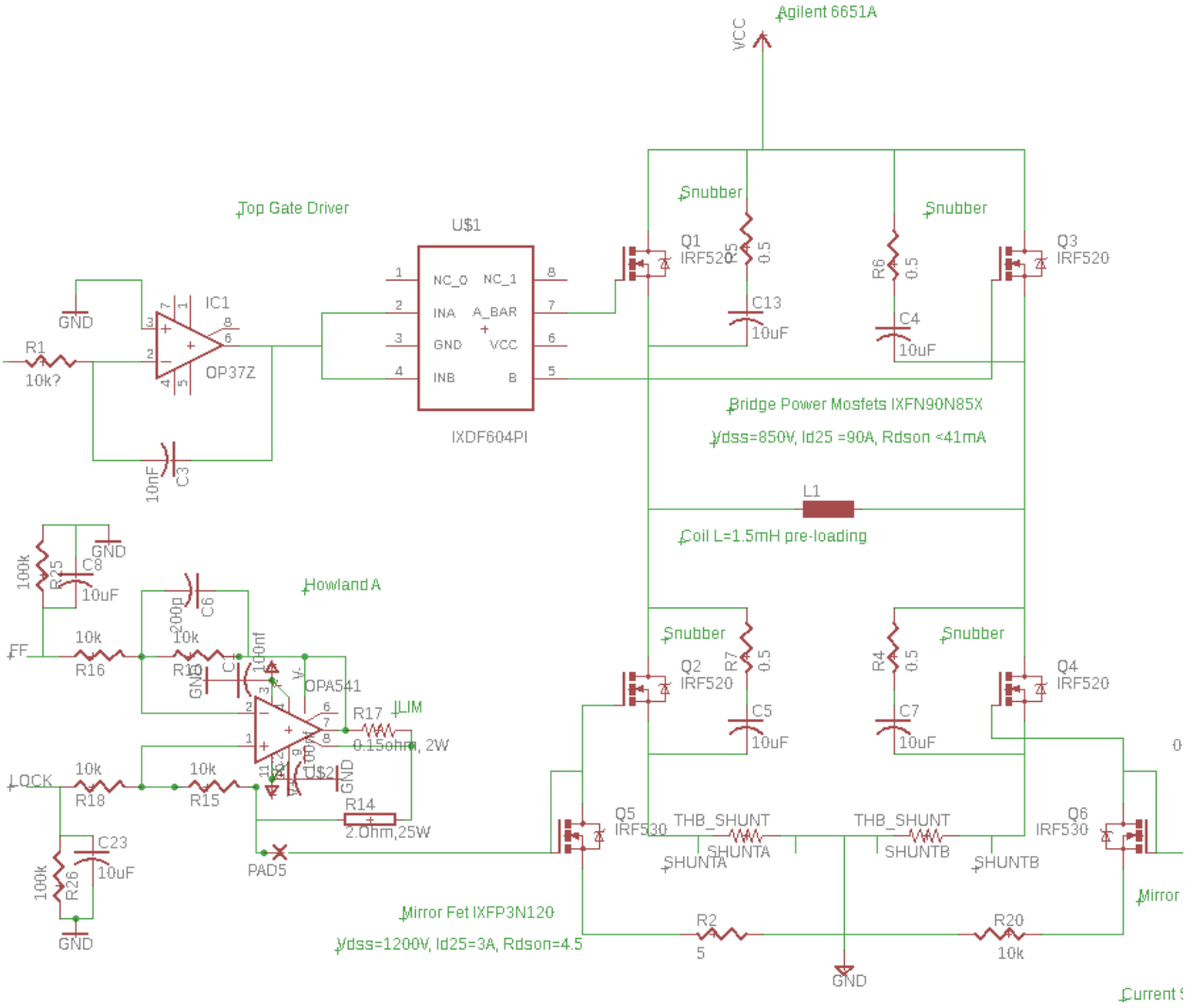

Figure 3.14. H-Bridge coil driver schematic. Four power MOSFETs are used to bidirectionally drive a current through each of our Helmholtz coils using a single Agilent 6651A power supply. The current direction is controlled via the top pair of power MOSFETs (left on right off or vice versa) while the current magnitude is locked via throttling the current in the bottom branch power MOSFETs via a mirror FET connection to a Howland current source circuit with the upper branch MOSFETs operating effectively fully open or closed as driven by a IXYS IXDF604PI inverted two channel gate driver IC which has a control voltage generated from an integrator circuit that samples the polarity of the control voltage applied to the throttling circuit allowing for bidirectional control.

Power MOSFETs behave like a more robust version of the basic MOSFET which operates as a 3 terminal semiconductor device consisting of a Drain (D) where current enters,

a Source (S) where the current exits, and a non current drawing Gate (G) terminal which has an applied voltage to bias the device and control the current passing from D-S, with power MOSFETs being designed for higher current and voltage operation as well as with the addition of an internal Zener diode connecting the source and drain to prevent damage from reverse biasing, (which is crucial for handling the back EMFs associated with inductive switching). The device operation can be thought of as a nonlinear voltage controlled resistor, a voltage applied across the drain to source V_{DS} will drive a current through a resistance controlled by voltage V_{GS}. The H-Bridge in our coil driver circuit utilizes IXFN90N85X power MOSFETs produced by IXYS, chosen for their high peak current ($I_{d25} = 90A$), avalanche breakdown voltage ($V_{DSS} = 850V$), and low on state resistance $R_{DS(ON)} \leq 45m\Omega$ value to prevent runaway heating where high currents lead to more heat which lowers the efficiency and increases the resistance further cascading the effect, as well as a relatively high transconductance (output current response to V_{GS} control voltage) allowing for a sufficiently large current response to the relatively small range of control voltages produced by the DAC outputs interfaced with our labview control cards.

The coil driver circuit implements an effective digital control for the upper power MOSFETs which determine the current direction and a locking circuit which throttles the magnitude current passing through the lower MOSFETs via analogue control. The analogue control voltage is first sent to a fast integrator circuit generating a digital signal which controls an IXDY604PI dual output gate driver (one inverted) capable of sourcing 4A of current for rapidly turning on/off the upper MOSFETs. Parasitic capacitances lead to finite coupling between all pins, causing there to be finite charging times for the gate pins, as well as some other undesirable oscillations (Miller resonance) when switching current direction through an inductive load.

The current in the lower branch is monitored via a pair of heat-sinked shunt resistors (CSI THB-50-500). Each voltage is measured referenced to ground via an INA103KP instrumentation amplifier, which are compared by a third INA103KP allowing for a bidirectional

current monitor. An error signal is generated by comparing the measured current to the set analogue control voltage followed by proportional gain and integration. To linearize the current response to the control voltage a current mirror FET design was implemented. The lock voltage is fed to a Howland current source which then drives a current through a second smaller power MOSFET connected in parallel to terminals G-S of the main power MOSFET. For a typical current mirror, the objective is to perfectly copy the current traveling through another transistor. For our circuit, we chose the second power MOSFET to have a much smaller transconductance, producing current gain allowing a small control current to faithfully drive a much larger main circuit current. 5Ω power resistors were added in series with the mirror FETs to reduce the control current needed to reach the main power MOSFET threshold voltage.

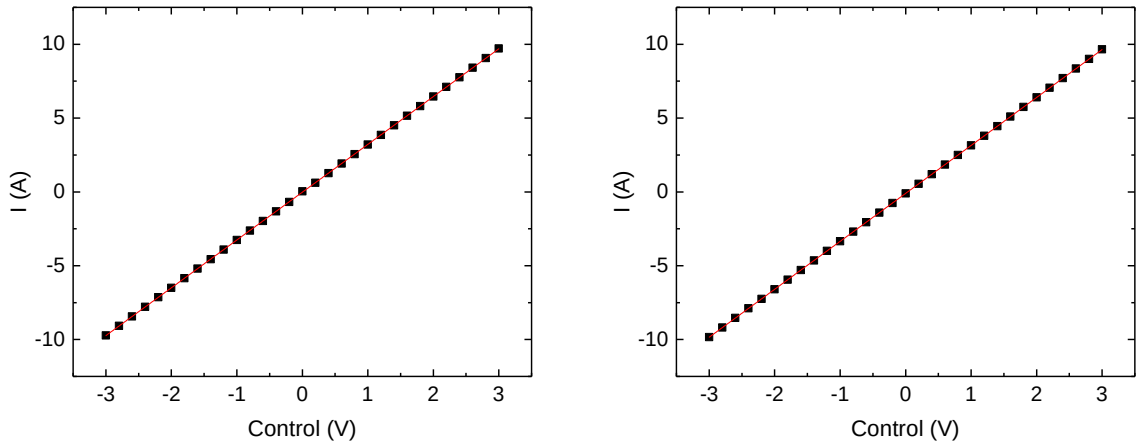

(a) Bottom Coil Control

(b) Top Coil Control

Figure 3.15. Coil current vs Control voltage for top and bottom coil driver circuits measured via keysight 3461A digital multimeter in series

The coil driver current vs control voltage was measured for both top and bottom circuits using a Keysight 3461A digital multimeter. Both circuits demonstrated very linear current responses, Top coil $I_{coil} = 3.2387(14)V_c - 0..0203(25)$, Bottom coil $I_{coil} = 3.2484(6)V_c - 0.1014(9)$. The offsets can be attributed to imperfections in the tunings of the three INA103KP voltage offsets used in monitoring the shunt resistors.

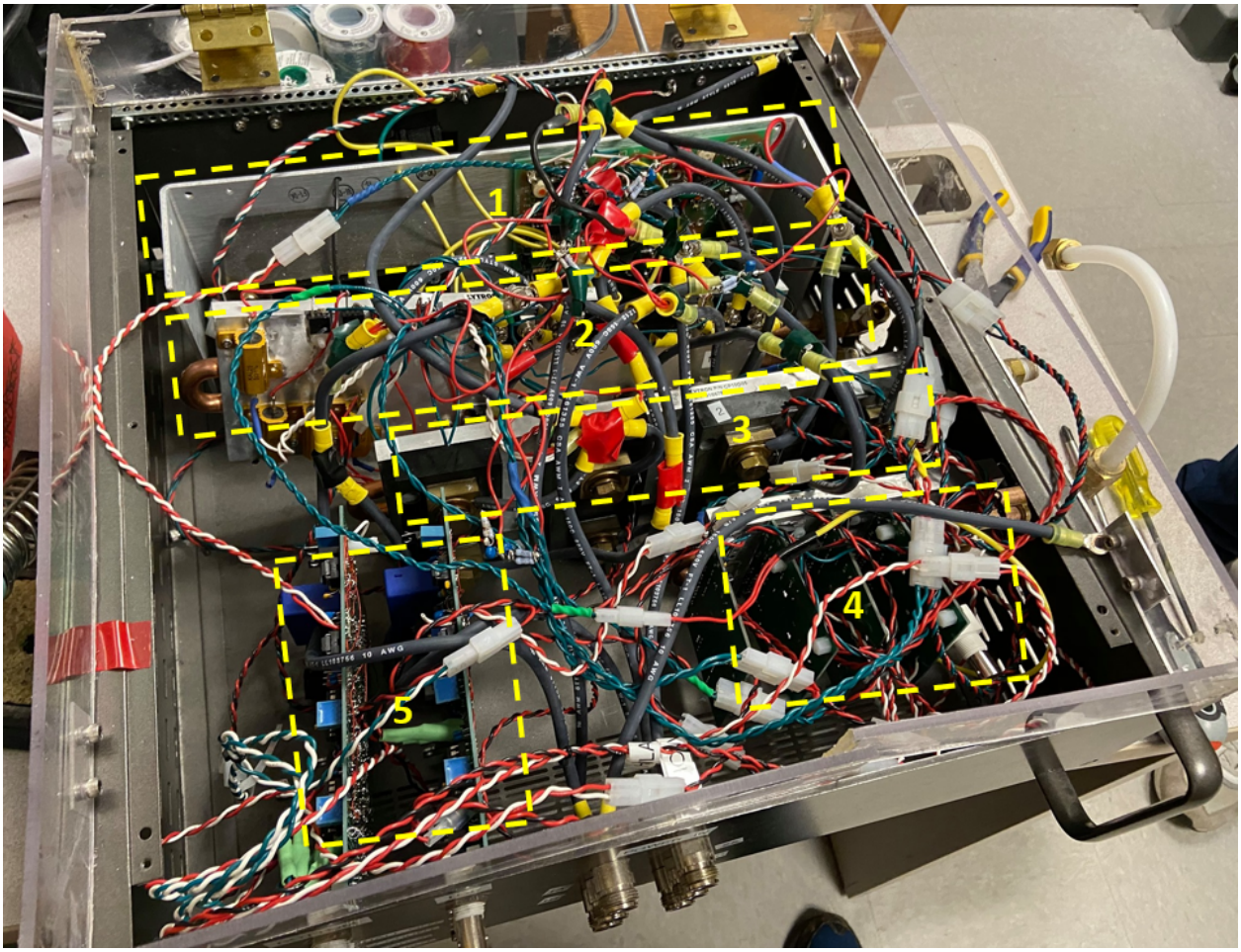

Figure 3.16. Coil driver circuit assembly. The coil driver circuit was built modularly and mounted into an enclosure. 1)±15V power supply for supporting coil drive locking circuit. 2) Cold plate 1 containing power resistors (left), 4 smaller MOSFETs for the mirror-FET circuit, and 8 power MOSFETs for both H bridge circuits (right). 3) Cold plate 2 containing the shunt resistors for current monitoring. 4) Cold plate 3 for heat sinking the power op amps in the Howland current drivers. 5) Coil current locking circuits

The coil driver circuit is assembled together in a enclosure with many features. The box is quite busy inside, if the circuit is redesigned in the future multiple PCB's could be integrated into a single design greatly reducing the need for free floating wires and cables. The box has an internal ±15V power supply for powering the current locking circuit as well as the Howland current sources used in the mirror-FET setup. There are three mounted water cooled cold plates in the enclosure each containing multiple elements. Cold plate 1

contains the power-MOSFETs comprising our H-Bridge design, a set of smaller MOSFETs used in the mirror-FET circuit, and power resistors used in the current mirror to lower the drive current needed to generate a given mirror control voltage. Cold plate 2 contains the shunt resistors used for monitoring the drive current in a given leg of the H bridge circuit. Cold plate 3 is for cooling the power amplifiers used in our 4 howland current source circuits for the mirror-FET design. The two current locking circuits are attached at the front of the enclosure with mounted BNCs for voltage control and current monitor outputs.

The main current used in our coil drive circuit for generating magnetic fields is provided form the previously mentioned Agilent power supply in a separate room and connected to the front panel via type N connector from pasternack. There are additional type N jacks for connections to and from the Helmholtz coils. Inside the box all lines carrying the main coil currents are provided via large diameter flexible multi-strand wiring with connections made via bolted down ring terminals while board to board connections for our current locking circuit components are provided via small diameter wire using Molex connectors. Return paths for the main coil currents are passed through onboard magnetic current sensors for additional reference to the voltage monitored on the shunt resistors. RC snubber circuits (shown in Coil Driver circuit diagram) are attached to the H bridge in parallel to the power-MOSFETs to dampen back EMFs induced during current switching to prevent miller resonances and other undesirable effects.

When initially designed the thought was current switching speed through the coils would be limited by the breakdown voltages of the power MOSFETS allowing for extremely quick rise and fall times. As we progressed in development of the circuit is was discovered that due to the nature of the Howland current driven mirror FET the current locking circuits on the 15V lines are effected by the H-bridge drive voltages. During switching the middle inductive line of the H-bridge can be forced between near ground and Vmax given by the voltage provided by the agilent current source. This complicates matters as the control voltage on each power MOSFET is dictated by the voltage difference between the gate and

source pins, not the gate refenced to ground meaning as the middle line of the H bridge floats, it's relative control voltage will change. Switching too fast can cause enough back EMF to toggle the top channel power-MOSFET above and below gate threshold voltage eg making them turn on and off leading to violent oscillations that will damage the circuit rapidly (usually immediately). The RC snubbers do help a great deal with this effect but it is not robust enough to stop the effect for all switching speeds so after much testing and debugging we decided to implement additional software limits on the coil switching speed via labview (with a slew rate of about 3V per ms for the coil current control voltage being about the upper saftey limit)

The locking circuit PCBs have onboard breadboard which was used to add the additional integrator circuit and IXYS gate driver circuits for controlling the floating top channel power-MOSFETS in the bridge. IF something goes wrong and rapid coil current oscillations are induced and the ciruit breaks it will either by the top gate driver IC (most likely and easiest to fix) or one of the power MOSFETs has broke down. When this occurs, immediately stop the labview control program, then power off the locking circuit 15V power supply on the back of the enclosure, then finally power off the Agilent current source. While debugging first check the gate driver IC's, if one is damaged it will typically draw high current on failure and the IC will be very hot to the touch making it easy to identify as the problem, these can be easily swapped out. Even if neither IC is warm it is recommended to swap the installed chip with a new one, one at a time for both boards to see if that fixes the problem. If both gate drivers are functioning properly it is recommended to check on the power-MOSFETs in the H bridge. Check each device and ensure there is high impedance between D-G and G-S. Next grounding the G terminal ensure that the impedance goes high in-between D and S representing the turned off state. If it is indeed one of the power MOSFETs that has failed, it may be required to remove the cold plate to gain sufficient access to the mounting screws on the cold plate. After making sure al power lines are off, shut off the coolant pipe lines for entry and exit to not drain coolant circulating to the rest of the lab, then with a cup or bowl

disconnect the line and collect the fluid inside the cooling loop in the cold plates to safely drain the water out prior to removal. Make note of all electrical connections you intend to remove, preferably take a photo of the device for reference before disconnect. When the plate is removed, unscrew and replace the damaged power-MOSFET, apply thermal paste to the device then mount and reassemble.

4. TRAPPING AND IMAGING INDIVIDUAL ATOMS ON TOP OF A NANOPHOTONIC CIRCUIT

4.1 Introduction

The integration of trapped atoms with nanophotonic circuits[63][64][65][66] provides for a rich platform capable of exploring topics in quantum optics, many body physics, and topological physics. Previous efforts in this field have mainly relied on individual suspended waveguide structures, providing sufficient optical access to facilitate traditional cold atom procedures, eg trapping cooling and imaging, but are more complicated to fabricate and assemble in situ and do not lend themselves towards a scalable architecture. The choice to pursue a 2D photonic chip platform has allowed for rapid prototyping, greatly advancing our rate of progress by limiting fabrication complexity. In addition, even though the results described in this thesis only seek to lay the ground work for coupling individual to small arrays of atoms to a single micro-ring resonator, the chip platform itself is already capable of extending itself to experimental architectures orders of magnitude more complex with the limiting factor being our external laser/optical setup.

As described in chapters 2 and 3, our approach makes use of a planar geometry fabricated on an optical chip which can facilitate many nanophotonic structures on a single device with the possibility of bus-waveguide coupling between multiple integrated devices . Guided modes on these nanophotonic structures allows for inducing cooperative atom-photon coupling, as well as novel evanescent wave trapping schemes which we are currently actively developing. In combination with the established techniques from modern cold atom toolkits this provides a path towards assembling quantum matter piece by piece with tunable interactions between constituent atoms.

4.2 Loading Atoms on Top of a Nano-Photonic Structure

For our first project we sought to trap, cool, and image Cesium atoms atop of a nanophotonic structure demonstrating the feasibility of our experimental architecture. A multi-layer photonic-chip was constructed using a silicon substrate, with a 550nm thick Si_3N_4 bottom layer followed by a 2 micron thick SiO_2 layer and a 360nm thick Si_3N_4 top layer upon which the waveguides and nanostructures are patterned using e-beam lithography. Subsequent chips we (Tzu-Han Chang[67]) developed implemented feature U-groove docking stations for external lensed fibers to transmit light into and out of the vacuum chamber coupled to bus waveguides that sends light to the nanophotonic structures fabricated on top of the 2x8mm window (figure 4.1 b), but for this device the fiber-waveguide docking design had not been optimized yet so fibers were epoxied onto the chip without optical coupling just as a mock up. The window was created by etching away the back silicon substrate leaving only the mostly transparent SiO_2 and Si_3N_4 layers, allowing optical access to for performing cold atom manipulations (trapping, cooling, state prep, detection) directly above the surface of the target nanophotonic structure. The previously mention Si_3N_4 bottom layer provides extra tensile strength to keep the window flat after removing the substrate, freeing the membrane.

The optical tweezer beam is generated from an M Squared SolsTis continuous-wave Ti-Sapphire laser tuned to Cesium's 935 nm 'magic wavelength'. A 2 level atom, (ground state $|g\rangle$, excited state $|e\rangle$) interacting with an oscillating electric field of frequency ω_L, with small detuning (Δ) from atomic resonance (ω_0), ($\Delta = \omega_0 - \omega$) $<<$ ω_0 can be described by a Hamiltonian consisting of two terms; $\hat{H}_A$ describing the bare atomic energy levels and $\hat{H}_{int}$ describing the interaction. Entering the rotating wave approximation yields Hamiltonian (4.2) where $\Omega = \vec{d}_{eg} \cdot \vec{E}_0$ is the Rabi frequency.

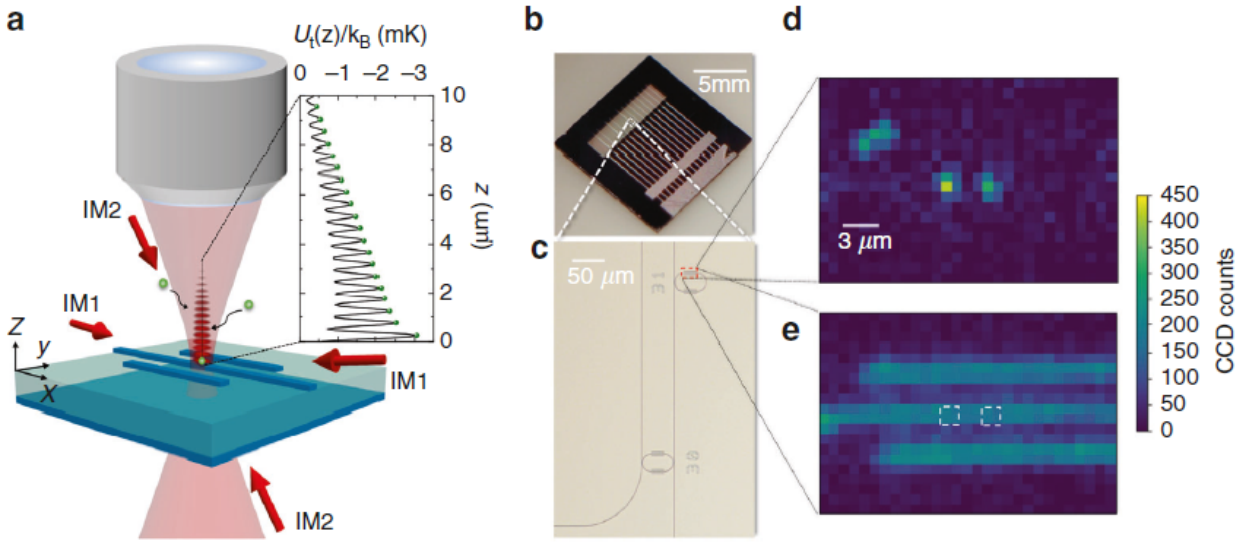

Figure 4.1. a) Experimental schematic, 935nm optical tweezer beam (light red) is focused on the surface of Si_3N_4 waveguide structure (dark blue) on top of the SiO_2 substrate via a NA=0.35 microscope objective. A small percentage of light reflected off of the structure interferes with the incident beam producing a 1-d optical lattice with 15-20 defined trapping sites (dark red ellipsoids). Trapped atoms (green) are fluorescence imaged by a pair of retro reflected near resonant beams (IM1 and IM2), and focused onto an EMCCD via the same microscope objective that focuses the tweezer light. b) Photonic chip, with back etched window (gray dashed) c) Zoom in of window region with Si_3N_4 waveguides and microring resonators depicted in dark grey. d,e) EMCCD images of two atoms trapped above waveguide structure with(d)/witout(e) polarization filtering of imaging light where the fluorescence imaging light's polarization is tuned to minimize scatter while a QWP HWP pair followed by a PBS in front of the EMCCD are tuned to remove this light letting half of the un-polarized light form the atom pass through

$$\hat{H} = \hat{H}_A + \hat{H}_{int} \tag{4.1}$$

$$\hat{H} = -\hbar\Delta \left|\mathrm{e}\right\rangle \left\langle \mathrm{e}\right| + \frac{\hbar\Omega}{2}(\left|\mathrm{e}\right\rangle \left\langle g\right| + \left|g\right\rangle \left\langle \mathrm{e}\right|) \tag{4.2}$$

$$E_{\pm} = -\frac{\hbar\Delta}{2} \pm \frac{\hbar\sqrt{\Omega^2 + \Delta^2}}{2} \tag{4.3}$$

$$E_{\pm} \sim E_{\mathrm{e}_0/g_0} \pm \frac{\Omega^2}{4\Delta} \tag{4.4}$$

$$\delta E = \pm\frac{3\pi c^2\Gamma}{2\omega_0^3\Delta} I \tag{4.5}$$

Solving for the energy eigen-states gives the bare excited(ground) state energies plus (minus) the light shift (δE), where I is the intensity of the electromagnetic field. For the ground state, using ($I \rightarrow I(\vec{r})$) for our tweezer beam gives exactly the dipole trap potential for a red detuned beam as derived in chapter 2. A problem arises when considering the opposite sign shift experienced by the excited state. $I(\vec{r})$ has a spatial dependence causing a differential light shift between S and P states, with frequency difference (ω_0), between $|\mathrm{e}\rangle$ and $|g\rangle$. While our trapping mechanism is dependent upon the spatial variation of the ground state light shift, the spatial variation of the differential light shift is very undesirable as different regions of the trap will experience a different detuning of our cooling and imaging beams leading to heating of the trapped Cesium atoms.

The magic wavelength solution arises from the full treatment of Cesium as a multi-level atom, which will include additional terms for all states coupled by the dipole operator, specifically the P-D transition for which the lower energy state P will receive an additional negative light shift. The solution for which the S and P states receive the same net light shifts, yielding constant ω_0 with no differential light shift, is called the magic wavelength and is commonly utilized for optically trapping different species in optical tweezers.

Out trap is formed by focusing the red detuned tweezer beam directly on top of the surface of the photonic chip. While SiO_2 and Si_3N_4 are mostly transparent in the NIR, a small amount of light is reflected off of the surface ($\sim 10\%$). The resulting interference pattern yields a small 1D lattice, with approximately 15-20 defined potential wells, with the bottom-most trap forming at (z<200nm) above the surface, being the deepest trap and stable against atom-surface Casimir-Polder interactions[68][69][70].

For our experiment the alignment of the focus of the tweezer beam onto the surface of our nanophotonic structure is crucial as small misalignment will not allow the atom to be trapped stably and close enough to a structure for sufficiently coupling to occur. The microscope objective we use is an apochromatic objective (corrected for 3 mm thickness of our vacuum glass view-port) serving our detection needs but does produces a small amount

of chromatic aberration, resulting in different imaging planes for the 935 nm tweezer trap and 852 fluorescence light. This makes aligning the tweezer beam focus to lie directly on top the surface of the structure very difficult to do visually.To surmount this and ensure proper alignment, we use the polarized tweezer light that gets reflected off of the surface and collected by the microscope and filtered prior to entering the EMCCD via a QWP HWP pair and a 1" PBS cube leading to the EMCCD. This polarization filtering was installed initially to improve signal to noise of light detected from our atoms verses background scatter during imaging, but by monitoring the power of this reflected beam allows us to infer information from the tweezer beams focal location by making use of the difference in reflectance between the silicon dioxide substrate $R_{SiO_2} \approx 0.3$ and silicon nitride waveguide $R_{Si_3N_4} \approx 0.03$ we seek to focus on. The silicon nitride waveguide has similar sized width (w=870nm) to that of our tweezer beam waist ($w_0 \approx 0.8\mu m$), and lower reflectance than silicon dioxide, so when the tweezer beam's focal plane truly lies of the waveguide rail of a structure it will have the smallest diameter and hence nearly 100 percent of the beam will fit on the structure producing the largest dip in reflected light. In practice to perform the alignment, the microscope objective height is adjusted in small steps followed by scanning the tweezer over and through the waveguide rail while monitoring the dip in reflected power measured to ensure true minimum.

Our experimental cycle consists of several steps to load atoms into the optical tweezer and eventually image them onto the EMCCD. To begin, atoms from a continuously operated source MOT in a separate chamber, connected to the science chamber via a long differential pressure tube, are transferred into our main science chamber via a push beam using radiation pressure. Unfortunately there is not a direct path for these atoms from source chamber to their target final position above the window of our chip due to the source chamber lying at a lower height on our optical table so we adopted a scheme to support multiple transport steps. The pushed atoms are initially collected in a large 'science' MOT comprising of 1" beams upon arrival,with a trap center located a few mms in front of the window of the optical

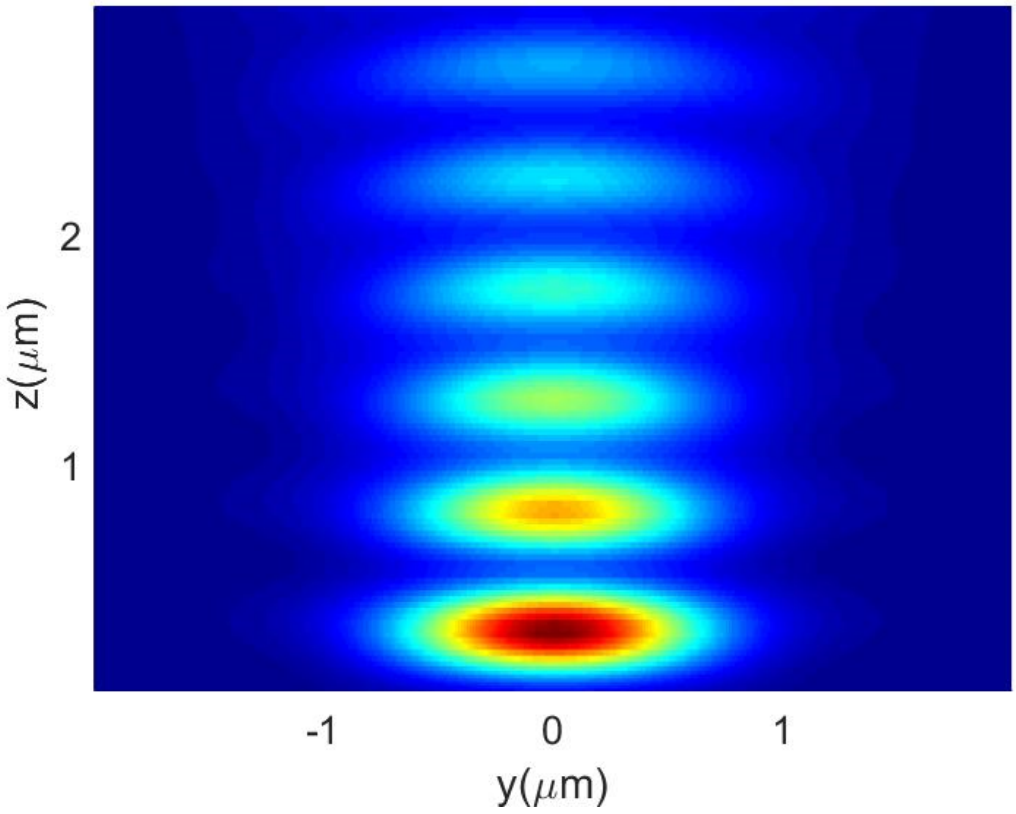

(a)

Figure 4.2. Comsol simulation of the intensity for 1D tweezer lattice formed by interference of incident tweezer beam and reflected beam for tweezer with $w_0 = 1.2\mu m$ focused at (0,0,0) directly on the surface of the Si_3N_4 waveguide (a.u.). For $P_{tweezer} = 5mW$, bottom-most trapping location has a trap depth of approximately 3mK. Fine adjustment of the silcon dioxde and silicon nitride layer thicknesses allows for tuning the height of the resultant interference field.

chip, typically gathering about a million cesium atoms at approximately $40\mu K$. Next the bias magnetic field of the MOT is briefly increased raising the cloud above the chip, followed by velocity selective cooling (VSC)[58][59] which imparts a controllable integer momentum kick proportional to the difference in k vectors of our MOT beams and "shoots" the cloud downward, at an angle, towards the target nanophotonic structure.

After VSC the science MOT beams are turned off and three smaller (w_0 $1mm$) retro-reflected 'mini-MOT' beams passing through the optical chip's window are turned on collecting atoms in a small cloud centered a few hundred microns above the surface of the target

resonator, with an atomic density of approximately ($\rho_0 \approx 3.5 \times 10^9 cm^{-3}$) near the surface of the photonic chip. The alignment of these mini-MOT beams is crucial as the tweezer loading rate is almost entirely dominated by the density of the cloud within the first few microns from the surface. After the transfer has completed the magnetic field is quickly zeroed and the mini-mot beams' frequency detuning from resonance is set for optimizing polarization gradient cooling (PGC), during which the tweezer beam power is increased to full power (5mW, 3mK trap depth) and atoms begin loading into the trap. After 10 to 20 ms of PGC, typically leaving the atoms cooled to about $15\mu K$, the cooling beams are turned off for at least 50 ms allowing for unbound atoms to exit the trapping region. This step is of great importance as loosely bound nearby atoms can scatter light and lower our signal to noise ratio.

4.3 Florescence Imaging

Next a pair of linearly polarized, near resonant beams (20 MHz red detuned from Cesium's $F = 4 \rightarrow 5$ transition) are turned on to perform fluorescence imaging for a period of 30ms, followed by a 40-50ms wait period to let unbound heated atoms escape the trap, and a second 30ms imaging period producing a second frame. Light scattered by the atoms is imaged using the same NA=0.35 microscope objective used for focusing the tweezer beam onto the surface. In addition to the aforementioned polarization filtering stage we implement a set of narrow band-pass filters centered on cesium's D2 transition, providing an order of 10^-12 attenuation for light outside of the D2 band, filtering out background light and any remaining light from the intense tweezer beam at 935nm. A pair of tube mounted lenses then focuses the collimated light onto the EMCCD.

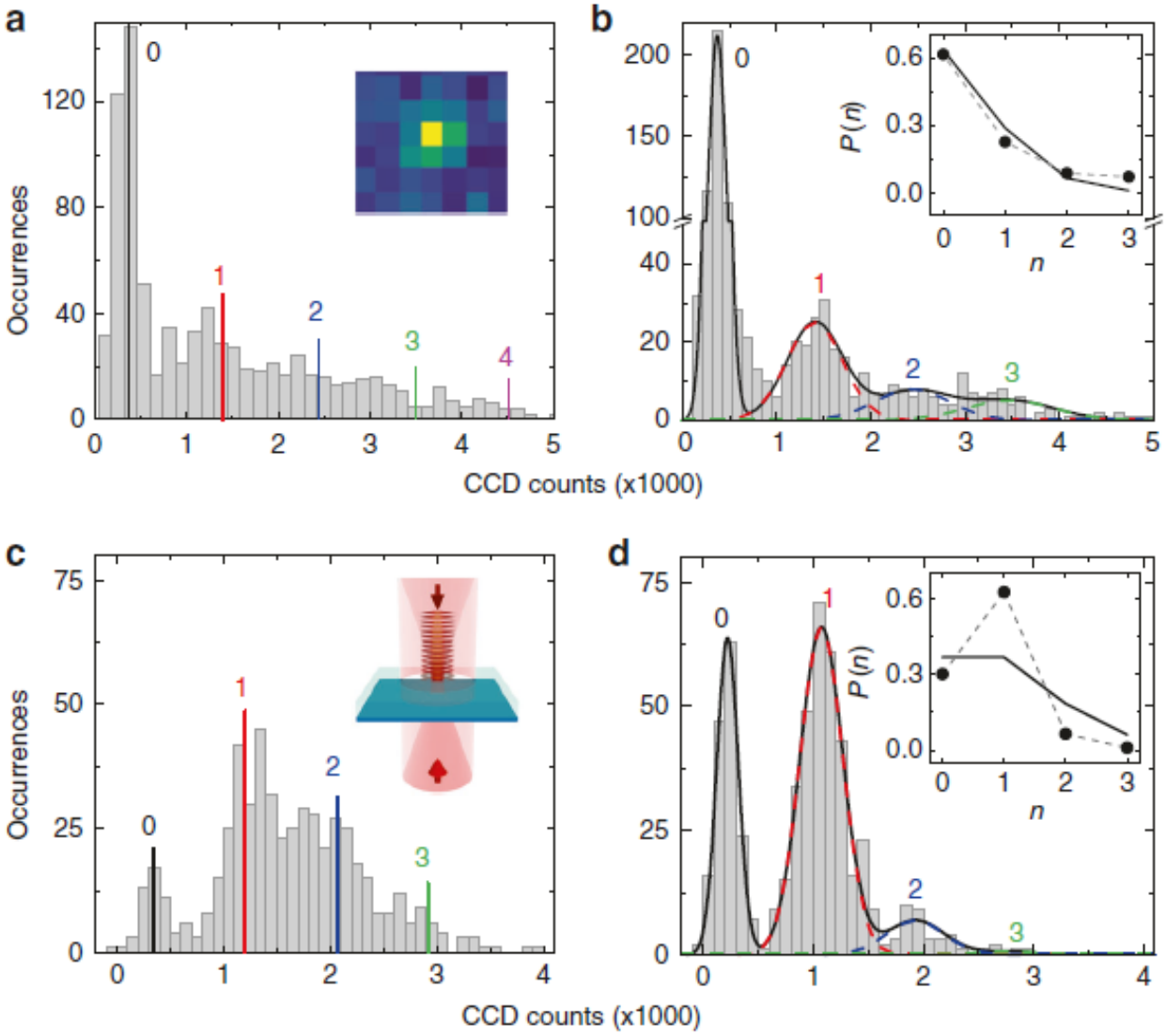

Figure 4.3. Florescence imaging of single atoms trapped on-top of nanophotonic structures. (a,b) Histograms of photon counts detected by EMCCD for atoms trapped on top of Si_3N_4 wave-guide structure. a) depicts the counts measured during the 'first frame' of 30ms fluorescence imaging, (b) is the 'second frame' of fluorescence imaging taken 40ms after the first. The imaging process heats out loosely bound atoms which scatter a few photons before escaping the potential well, producing a clearer second frame with more distinct atom-number peaks. (c,d) Histogram of photon counts for trapped atoms on top of SiO_2 membrane (with no wave-guide structure) when an additional second broader, ($w_0 = 7\mu m$), phase coherent dipole beam from the same 935nm source is introduced to increasing trap depth and improve loading efficiency. Discernible 0 (Background), 1,2, and 3 atom peaks are present

Histograms for the resultant number of photons detected during florescence imaging sequences by the EMCCD for two experiments (both repeated 1000 times) are shown in figure 4.3. In sub-figures (a,b) a single tweezer beam is focused onto the rail of a micro-ring resonator to load atoms, a) shows the florescence counts for the first frame (30ms imaging sequence) and b) shows the second frame. A clear background peak is observed in frame 1 while 60% of the time we observed florescence count's distinctly higher than background but without sufficient contrast in the higher photon counts region to clearly identify tom number peaks. The second frame though does demonstrate the desired separate atom number peaks, which are fitted to Gaussians (solid black, red, blue, and green curves in b)), with approximately 1000 photons detected per atom per experiment, vertical reference lines are imposed in a) to show atom number centers. In frame 2 40% of the time we observe count's corresponding to 1 or more atoms. After fitting the atom number peaks to a sum of Gaussians, the probabilities of trapping 0,1,2,3 atoms are fitted using a Poisson distribution consistent with $\bar{N} = 0.45$.

As can be seen by the increase in height of the background peak (0 atoms) in the second frame (b) the near resonant imaging beam heats some of the atoms out of the trap during the first imaging sequence. This lowers the number of atoms detected in frame 2 but has the benefit of also removing the loosely bound atoms that scatter a few photons during imaging before escaping, which are responsible for the poor contrast in frame 1.

4.4 Improving Loading Probability with Introduction of 'Bottom' Dipole Beam

To improve the atom loading probability into the tweezer lattice a more powerful (84mW), broader ($w_0 = 7\mu m$), dipole trap beam was introduced from the bottom of the chamber, counter-propagating towards the incident top tweezer beam. The initial thinking was to increase the trap depth of the lattice sites and at the same time increase the atom flux from the PGC cloud towards the lattice sites. This beam, referred to as the 'bottom' or 'back' beam, is derived from the same TiSaph source as the top tweezer beam, with all

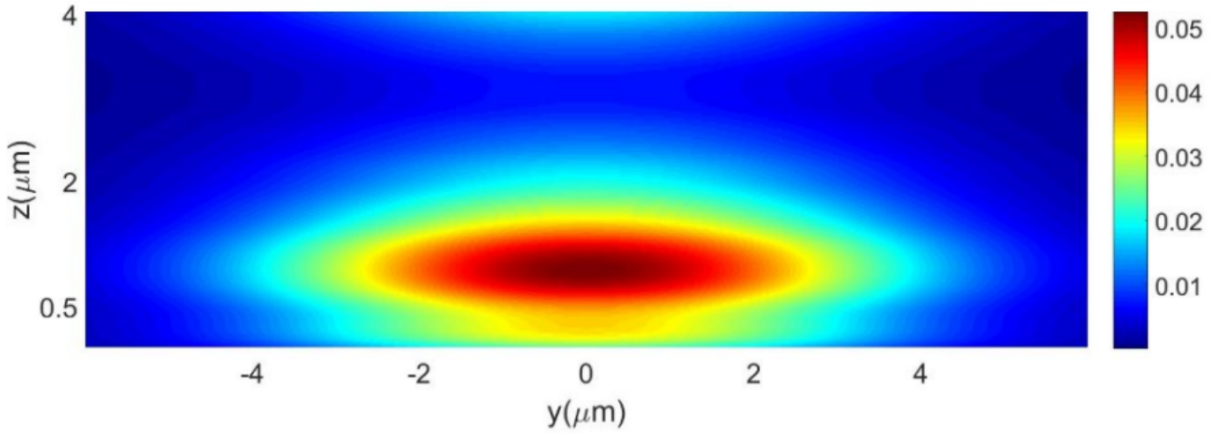

Figure 4.4. Cross section of the intensity pattern for a 935nm 'bottom' beam with a beam waist of $10\mu m$ diameter focused onto a silicon nitride waveguide entering from the bottom of the window (a.u.) with the membrane lying at z=0. As the beam passes through the smaller width waveguide rail, the dielectric contrast of the waveguide structure creates a lensing effect with a focal point about 1 micron above the surface of the waveguide rail.

control AOMs and AODs being driven by the same AWG allowing phase coherence of the beams. A 1:1 microscope was made using two thorlabs AC508-300-B-ML f=300mm, 2" diameter achromatic doublet lens connected via lens tube and an initial f=4.5mm aspheric fiber collimator intentionally slightly misaligned from collimation to match the divergence angle of the focused 300mm lens. Light entering through the bottom of the chamber focused on the top of the window passes over the silicon nitride waveguide and experiences a lensing effect which further focuses the beam.

To measure the effect of this beam on the atom loading efficiency we performed experiments with the same atomic cloud preparation as before, but with the trapping site moved off of the waveguide structure to the membrane to remove potential complexities from the bottom beam lensing over the waveguide, with the bottom beam left on during the loading procedure but ramped off before imaging. Sub-figures (c,d) in 4.3 show the photon detection histograms for atoms imaged in the tweezer lattice after loading with the back beam on. In the first frame c) a clear increase in overall photon counts is observed com-

pared to the top tweezer only scheme, with approximately 90% of the experiments having counts distinctly higher than background, indicating 1 or more trapped atoms. The second frame again displays improved contrast of the atom-number peaks and a 60% probability of retaining one or more tightly trapped atoms after imaging.The peaks were fit to a sum of Gaussians to calculate the loading probabilities, yielding a sub-Poissonian distribution $\langle \delta N^2 \rangle = 0.35 < \bar{N} = 0.77$ attributed to the collisional blockade effect[71][72] while atoms are being cooled and loaded into the lattice. Performing fits on the first frame yields a mean atom number of $\bar{N} \geq 1.6$

As mentioned before, these experiments utilized a 'dummy' chip with waveguide structures but no actual coupling of the bus waveguides to the optical fibers taking light in and out of the vacuum chamber. Without that tool we were unable to directly explore atom-light interactions with the cavity field, at the time, which would have allowed for probing if the atom was truly trapped in the closest site as the evanescent field falls off rapidly for trapping locations outside of the first hundred nm above the resonator. Using to EMCCD we are constrained by the objectives optical depth of field ($z \leq 10\mu m$) when determining the vertical position of a given trapped atom in the tweezer lattice, limiting our knowledge of the true trapping location to that of one of about 15-20 lattice sites. Due to the rapid fall off of the evanescent coupling of cavity photons with atom height above the surface, any future plans for the experiment will require atoms that are in fact loaded in the closest first lattice site to have sufficient atom photon coopertivity to coherently perform operations so we explored how much we could infer with only our optical microscope measurement of the atoms position.

4.5 Monte-Carlo Simulations of Trap Loading Probabilities

Revisiting the tweezer lattices intensity profile, a Monte-Carlo simulation was performed for atoms loading into the lattice to get an estimate of the loading probability of a given lattice site using MATLAB and scaled versions of the previous COMSOL generated intensity

simulations. For the simulation atoms were loaded from the borders of a 10x10x10 micron cube simulation region with the waveguide structure centered on the bottom of the x-y plane at z=0. Casimir-Polder interactions were modeled via a simplified potential $U_{CP} = -\frac{C_4}{z^3(z+\tilde{\lambda})}$ where $C_4/h = 158(267)$ is the CP_4 coefficient[73] for cesium above a $SiO_2(Si_3N_4)$ plane and $\tilde{\lambda} = 136nm$. 10^6 simulations were performed with randomized initial positions on the simulation boundary regions and initial velocities generated from a Boltzman distribution for cesium atoms at $20\mu K$. In addition to the tweezer potential, optical molasses was included in the simulation via probabilistic scattering momentum kicks, this was chosen for simplicity compared to modeling PGC but does yield higher temperatures than our actual experiment allowing us to take these results as more of a floor to expect for worst case scenario meaning our true value should be slightly higher. An atom was considered trapped, and it's final location recorded, if it remained in the simulated region during the entire 100ms-1s simulation, simulations were terminated and atom recorded not trapped for cases where it left the region.

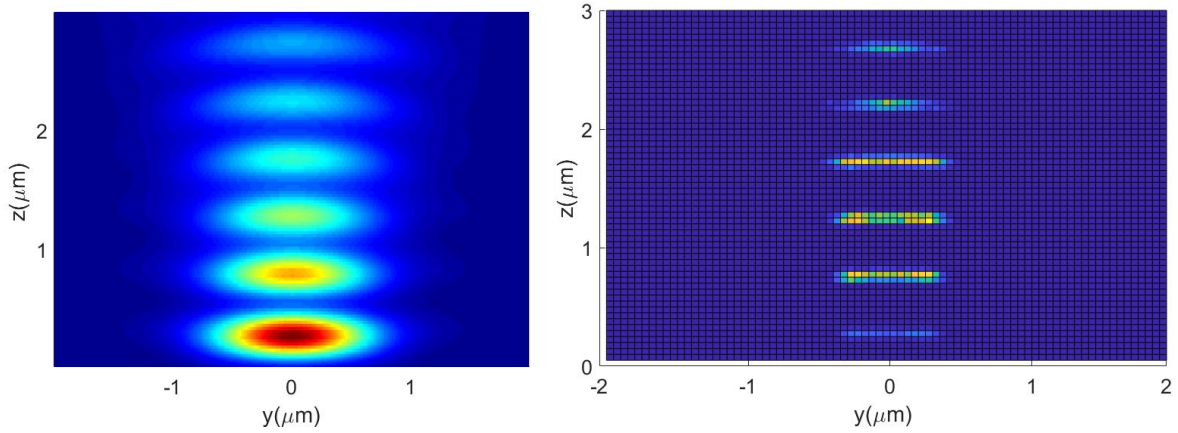

(a) (b)

Figure 4.5. a) Tweezer lattice intensity profile for $1.5\mu m$ beam focused on top of the waveguide structure (a.u). b) Monte Carlo simulation for trapped atoms final location after 200us of travel time loaded from $x = -2\mu m$

Of the 10^6 simulations, 1.3% of the trajectories remained trapped, and only 2% of those were populating the target bottom most trapping site. This came as quite a surprise to

us, when designing our system we felt confident that the bottom site, being the deepest trapping potential in the lattice, would be populated at a much higher rate. Geometrically the explanation lies in the fact that once an atom enters a lattice site it has a high probability of remaining in that site due to it's low kinetic energy (fig 4.5), and the solid angle for trajectories that can successfully be pulled into the bottom site is actually quite small, with the higher up sites in effect shielding atoms from making it to the bottom site unless an atom near the surface entered traveling nearly parallel to the surface.

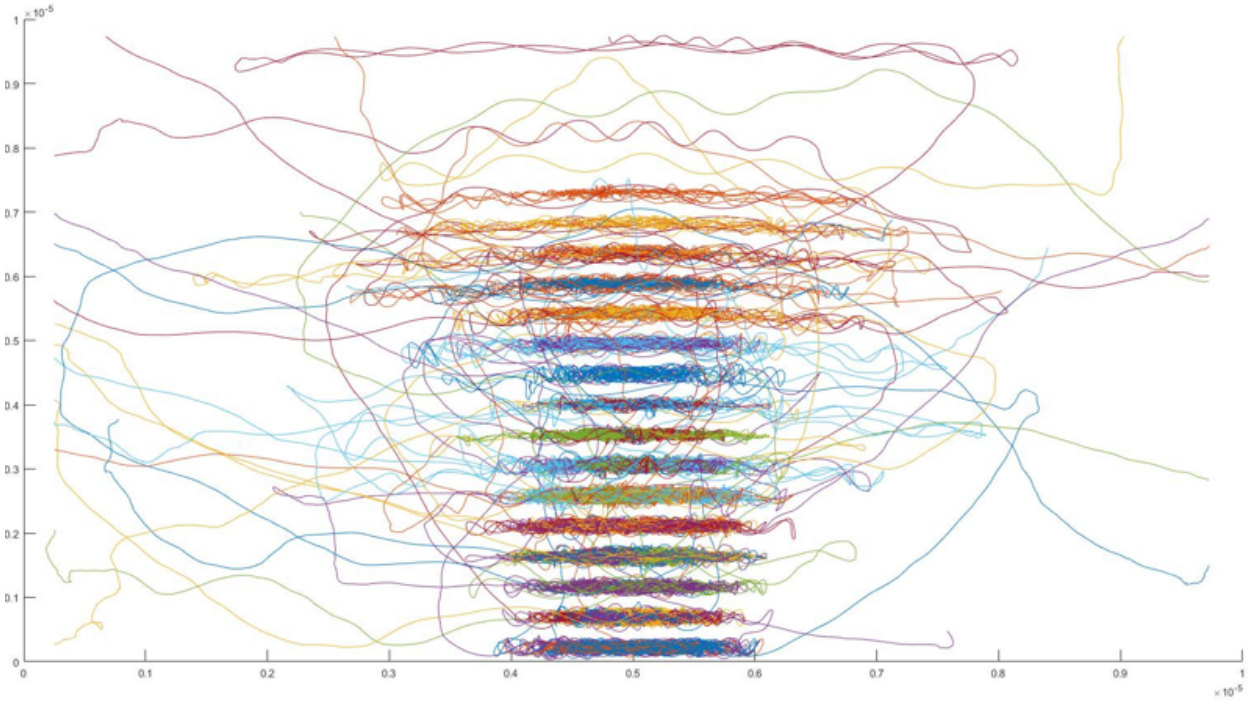

Figure 4.6. Sample trajectories for cesium atoms which successfully remained trapped during the Monte-Carlo loading simulation. Atoms initially entering form the boundary walls of the simulation region are pulled towards the lattice before entering a particular lattice site with the atoms almost always remaining trapped in that same site for the duration of the simulation.

Monte-Carlo simulations were then performed with the additional presence of the bottom tweezer with the beam in(out) of phase with the incident tweezer beam, yielding a lattice trapping probability of 27%(13%), aided by the larger trapping volume and increased trap depth at each site. Figure 4.6 depicts the probability distributions for loading in a given

lattice site for those atoms which remained trapped during the simulations. Even though the overall loading probability remains higher, the percent of trapped atoms populating the target site is still low (P<2%) indicating that a new loading method would have to be designed.

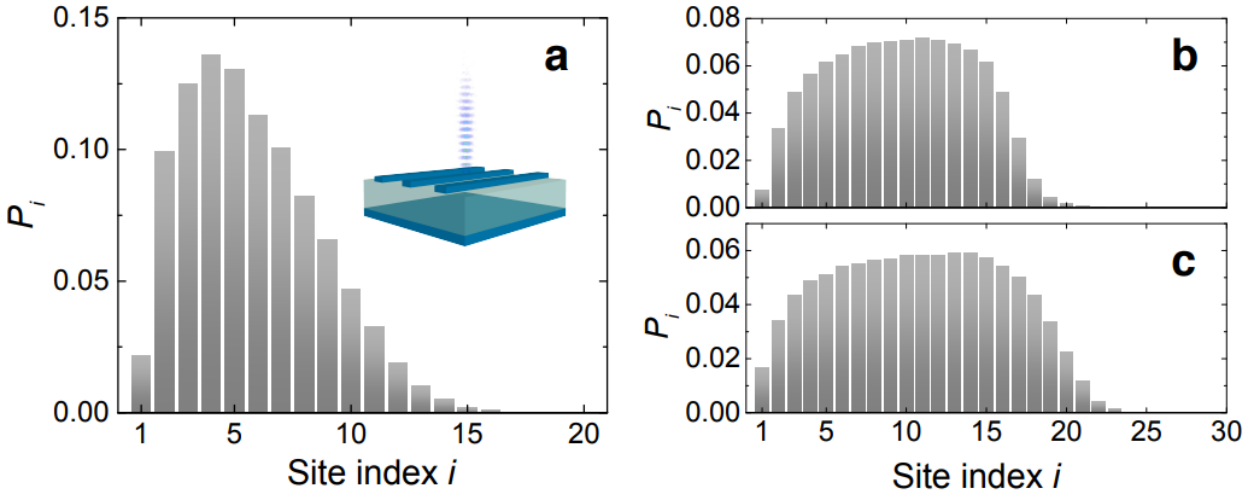

Figure 4.7. Normalized loading probability for each site in the tweezer lattice from Monte-Carlo simulations where site 1 corresponds to the bottom most site on top of the chip. Loading probabilities for loading into a) tweezer lattice only, b) tweezer lattice with additional bottom dipole trap beam turned on in phase with the tweezer reflection and c) out of phase with the tweezer reflection.

4.6 Optical conveyor belt

After a few brainstorming sessions, my advisor suggested we consider using the bottom beam to implement a technique previously demonstrated for transporting atoms confined in free space optical dipole traps called an 'optical conveyor belt'[74][75][76]. For this technique atoms are initially trapped in a lattice formed by two coherent counter-propagating dipole beams of the same frequency ν, then to conveyor atoms one of the beams is slightly red-detuned by $\delta\nu$ producing a traveling wave in the lab frame(eq 4.4), but a coherent standing wave for an atom moving at velocity $v = \lambda\delta\nu/2$, which sees equally shifted beams of the

same frequency. Leaving the frequency detuning on for time Δt shuttles atoms a distance $\delta z = \lambda/2 \int_0^{\Delta t} \delta\nu(t)dt$

$$U(\rho, z, t) = U_0 \frac{w_0}{w(z)^2} \mathrm{e}^{-2\rho^2/w(z)^2} cos^2(\pi\delta\nu t - kz) \tag{4.6}$$

The top tweezer passes through a pair of AOD's both driven at 80MHz by a channel from the AWG for a net shift of 160MHz, while the bottom beam is controlled by via an AOM in a double pass configuration, and driven by a second channel on the AWG at 80MHz leaving both with the same frequency shift. To implement the conveyoring, the AWG was programmed to linearly ramp the bottom beams channel to half of the target frequency detuning ($\delta\nu/2$) over 1ms (double pass adds shift twice), hold for time τ ms, then linearly ramp back to the initial 80 MHz tone over another 1ms period. The potential of the lattice + back beam is shown in fig 4.8-a, with about 30 trapping sites defined in the depth of field of the microscope objective ($z_{df} \approx 15\mu m$).

To observe the effect of the conveyor belt, experiments were performed in which atoms were initially loaded into the tweezer lattice + bottom beam field on top of the membrane as before. After turning off the cooling beams for 50ms, the shuttling program was triggered for a range of detuning frequencies from ≈ -20 to $\approx +20$kHz, with a hold time of 1(gray), 3(green), 7(red), or 9ms (blue). After shuttling the bottom beam is ramped off over 2ms then florescence imaging is performed as prior. Fig 4.7-c displays the mean counts observed in the first frame after the shuttling procedure for the various hold times as a function of frequency, and 4.8-d displays the mean photon counts detected form the same experiment as a function of the shuttling distance. As the atoms are shuttled upwards or downwards the mean counts is observed to drop off, immediately it is apparent that the loss in counts (atoms) is dependent only on the shuttling distance not the shuttling frequency indicating that the loss mechanism is indeed due to the atoms being conveyored out of the lattice and not heating from the conveyoring or other effects (as this would be frequency dependent).

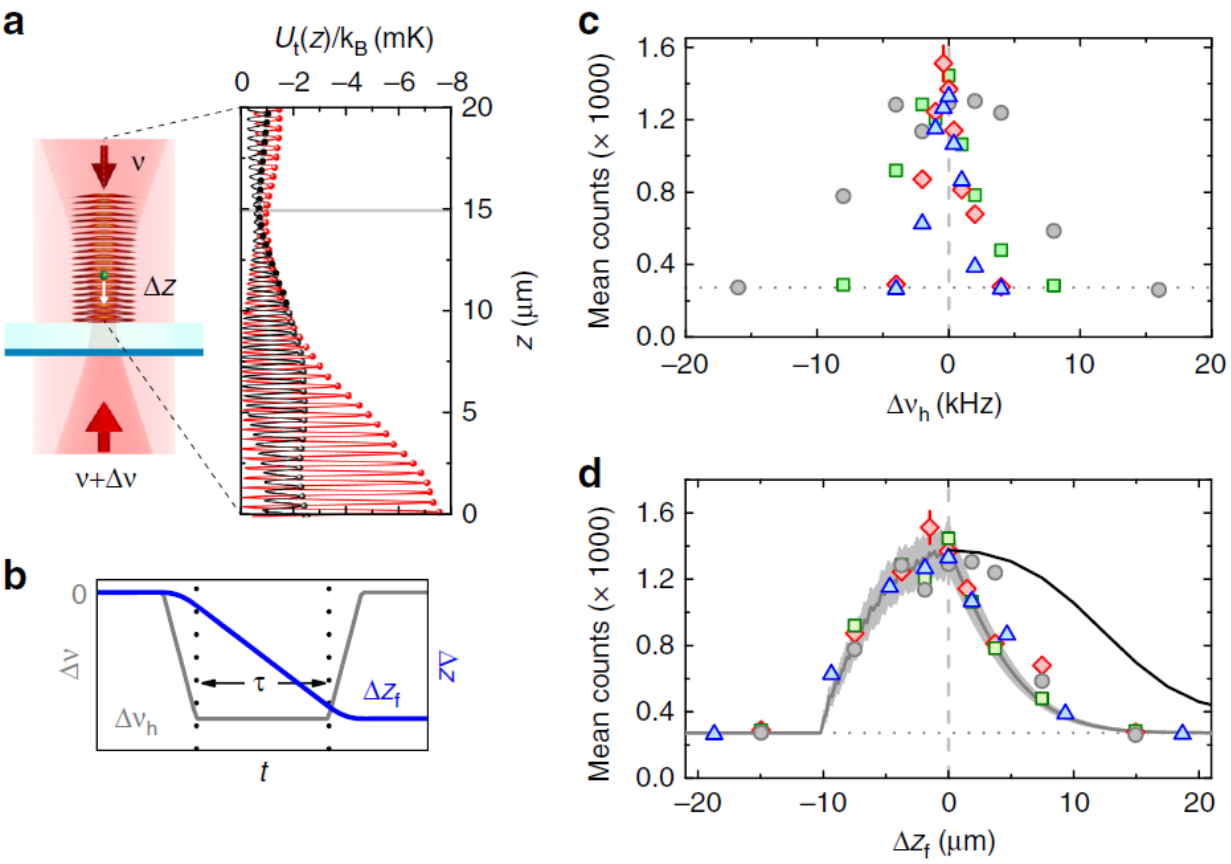

Figure 4.8. Optical conveyor belt for atoms trapped in a tweezer lattice above a nanophotonic structure. a) Top tweezer beam (Red) is focused onto SiO_2 membrane and partially reflected, with the resultant interference pattern producing 1D lattice (dark red ellipsoids). Bottom dipole beam (light red) is introduced producing trapping potential U (inset) where the red(black) curves represent the case of the bottom dipole beam being totally in (out of) phase with the reflected tweezer beam. b) Transport distance for atom in tweezer conveyor for back beam detuning ν and hold time τ. c) Mean fluorescence counts for atoms after conveyoring with 1 ms chirp rise/return and 1ms(gray), 3ms(green), 7ms(red), or 9ms (blue) hold times vs frequency detuning of back beam. d) Same as c, but plotted vs shuttling distance Δz, different conveyoring frequencies were used to verify the loss of atoms is not due to heating induced by the conveyor. The solid black line represents the loss in photon counts due to the microscopes inability to focus light from atoms onto the EMCCD as the atom moves upward away form the focal plane, with the steeper measured reduction in mean counts indicating that atoms are in fact being loss as they are shuttled upward into the the weaker potential. For the case of atoms shuttled towards the surface, as the conveyor moves the atom down the tweezer lattice sites become deeper (stronger trap), maintaining photon counts on detection until an atom is conveyored into the surface and lost producing the observed asymetry in counts with shuttling direction.

The gray line in d) is the fit to mean atom number with the shaded area indicates the uncertainty of mean. The solid black line for ($\Delta z_f \geq 0$) is the calculated loss in counts that would occur due to atoms moving outside of the objectives depth of field as atoms are shuttled upwards and the objective can no longer focus scattered photons onto the EMCCD. The asymmetry of mean counts observed for shuttling upwards vs downwards can be explained as follows: when moving upwards the objective is able to focus less light from the atoms, as mentioned, but additionally the trap depth of the lattice sites is decreasing the further away from the tweezers focal plane on the surface resulting in atoms escaping during shuttling or being heated out of the shallow uppermost lattice sites during imaging. As the atoms are conveyored downwards, they are moving towards the focal plane of the , and the lattice trap depth is increasing up until the last site, resulting in more counts per atom, therefor the decrease in mean-counts is attributed primarily to atoms impacting the surface and exiting the trap.

In the future we plan to extend this conveyoring scheme to multiple atoms confined in an array of tweezer lattices utilizing a common bottom beam. The scheme would begin by loading atoms into the tweezer array, with each tweezer being separated a few microns apart from one another, all directly above the waveguide of a microring resonator. This time we will make use of a broader back beam, ($w_0 \approx 15\mu m$) capable of addressing all of the tweezers in the array. The array itself will be generated by driving the AOD's with a multi-tone signal with each tweezer beams driving tone separated by 8-10MHz from one another. The frequency separation of the tones used for the AOD's is much larger than the trap frequency for atoms inside a lattice site (10's to 100's kHz), allowing the back beam to only be sufficiently tuned close enough to one tweezer tone at a time during the conveyoring pulse, while the other atoms observe a detuning to high in frequency to respond to, and effectively experience a time averaged stationary lattice and are not shuttled, providing us the ability to individually addressing the atoms one at a time.

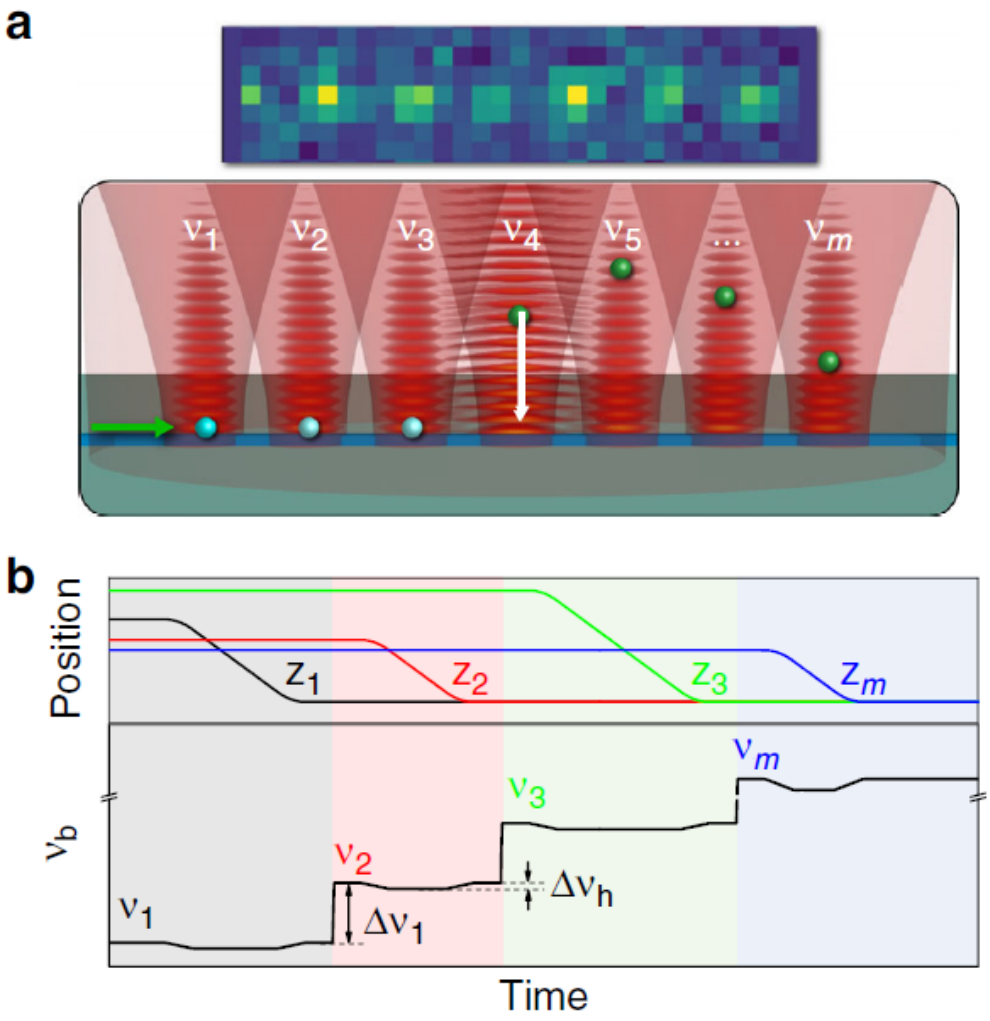

Figure 4.9. Conveyoring atoms in a tweezer array. a) Linear array of 7 tweezer lattices loading atoms on top of membrane using a multi-tone signal from an AWG to drive an AOD, each tone separated by 8MHz, and approximately 4mW power per tweezer. Illustration of an array of atoms trapped on top of waveguide with atoms loaded into random lattice sites. When the back beam is near red detuned from a target tweezer that site will be conveyored while the detuning from the neighboring sites is large enough that atoms trapped will see a time-averaged stationary lattice. b) Proposed back beam conveyor frequency ramping scheme, quickly jump to near target tweezers detuning, allow approximately 5-10ms for conveyoring, probe if an atom is coupled, upon verification shelf current atom in dark state then shift the frequency of the bottom beam to the next site and repeat

Implementing the process with a photonic chip which actually has fiber connections will allow probing the transmission of the bus waveguide evanescently coupled to the target mi-

croring resonator during the experiment. When an atom is not present within the evanescent field range (bottom lattice site), the atom is not coupled to the microring, light on resonance with the microring resonator, (with the rings resonant frequency being tuned to atomic resonance) will couple strongly to the ring from the bus waveguide, greatly reducing the photon transmission rate. When an atom is trapped within the evanescent range of the microring, the atom-cavity systems forms a pair of dressed states with frequecies seperated by g (on the order of 100MHz for our system) and are no longer on resonance with the bare atomic resonance, greatly increasing transmission. Once atom-cavity coupling is detected the atom can be pumped to a dark state using waveguide photons, the back-beam detuning can then be shifted to address the next tweezer and the process can be repeated.

5. LOADING ATOMS ON TOP OF A NANOPHOTONIC CIRCUIT VIA A 7 TWEEZER ARRAY WITH HIGH PROBABILITY

If order to demonstrate the feasibility of our platform we need to be able to demonstrate that we can extend our trapping scheme beyond a single atom in a tweezer lattice to multiple atoms trapped in an array of tweezer lattices. With our current geometry, (approximately 100 micron circumference micro-rings with atoms trapped in $w_0 = 0.8\mu m$ tweezers transversely separated 1-3 microns from one another other upon the surface of the micro-ring structure) we can facilitate arrays with 10's of tweezer trapping locations per micro-ring without having the traps impinge on one another. For reference state of the art ion and superconducting qubit based systems both have on the order of 50 qubits[77][78][79] . For this example we used a linear array of 7 tweezer traps on top of the membrane of our photonic chip to demonstrate how well we could trap multiple atoms at a time.

To implement the 7 tweezer scheme we made use of one of a pair of orthogonally mounted accouto-optic-defectors (AODs)[80] driven by a Keysight arbitrary waveform generator (AWG) outputting a multi-tone signal to produce multiple beams from a single incident source beam derived from a TiSaph laser operating at Cesium's magic wavelength at 935nm. An AOD operates by the same principles as an acousto-optic modulator (AOM), but has been designed to have a linear deflection angle vs drive frequency and a broader RF bandwidth. Our Isomet 1205C-x-804B has a peak efficiency of 85% at 80MHz, and drops down to 77% at 70(90)MHz and 66% at 60(100) Mhz. After passing through our optical layout, the AOD produces a beam deflection of $0.383\mu m$ per Mhz on the surface of the photonic chip. The AWG was programmed to output a 7 tone signal centered at 80MHz with tones separated by 8MHz, with the amplitude of each tone scaled to account for our expected efficiency decreases in the AOD away form 80 MHz. The optical tweezer power was tuned to be approximately 4mW per tweezer in situ on the photonic chip (after losses).

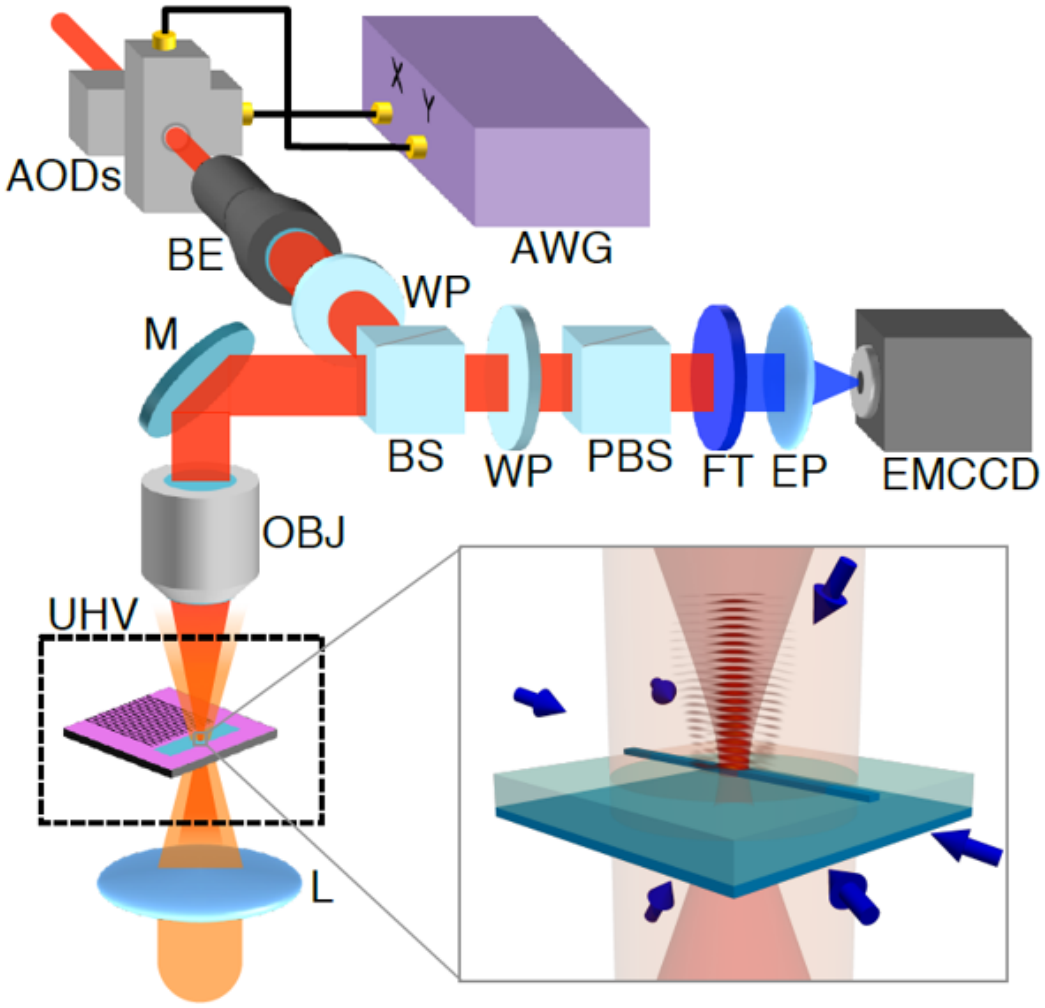

Figure 5.1. Experimental schematic for preparing arrays of tweezer lattices on top of the surface of a photonic chip. 935nm tweezer beam from TiSaph (red) is incident upon a pair of orthogonal AODs (only a single is implemented in this work) driven with a multi-tone signal from an AWG. The beam is expanded via a commercial beam expander (BE) prior to entering the backside of a NA=0.35 microscope objective (OBJ) where it is focused onto the surface of a micro-ring on the window of a photonic chip. Atoms trapped in the tweezer lattices are imaged via near resonant fluorescence beams (blue) with light scattered by the atoms being collected and collimated by the same microscope OBJ, before being polarization (WP & PBS) and wavelength (FT) filtered such that only light at Cesium's D2 transition is focused onto the EMCCD for imaging via a final eye-piece optic

5.1 Background and Cross-talk

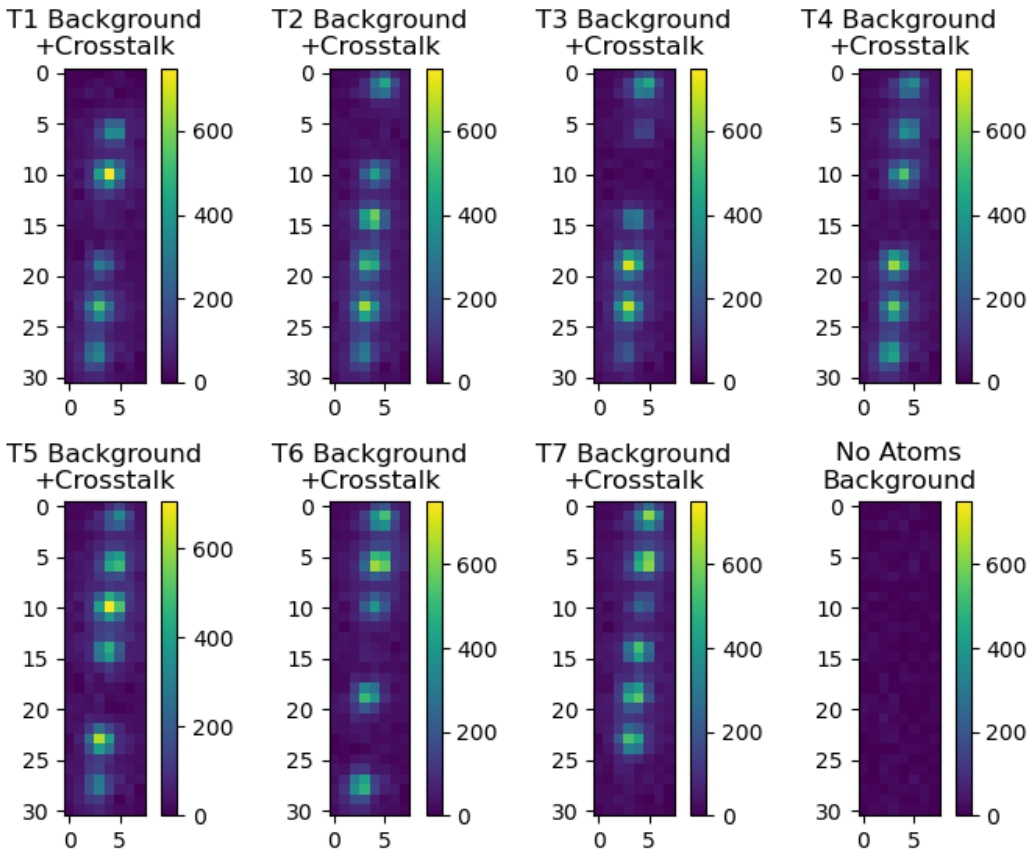

Figure 5.2. Mean counts images of tweezer array datasets used for background measurements. For each tweezer, a background was taken with the target tweezer turned off while the others remained on, this way the effect from cross-talk due to neighboring sites can be accounted for. XY coordinate represent EMCCD pixel location, color bar depicts mean photon counts per pixel.

To quantify the success of our loading scheme, we want to know how likely our system traps at least one atom per tweezer, as well as the mean atom number loaded into each tweezer. Having seen evidence of collisional blockade effects we expect no more than 1 atom per lattice site in a given tweezer, and due to the short range of the atom-cavity coupling only an atom in the bottom lattice site closest to the surface will interact with the micro-ring, so

as long as at least one atom is trapped per tweezer per experimental run it can be shuttled to the target lattice site allowing for planned operation without too many detrimental effects. Unlike our previous result with a single tweezer where photon detection counts are solely due background light, when implementing arrays of tweezers, atoms trapped in an adjacent tweezer location can contribute to the light detected in a given target tweezer's pixel bin area on the CCD, causing cross-talk[81].

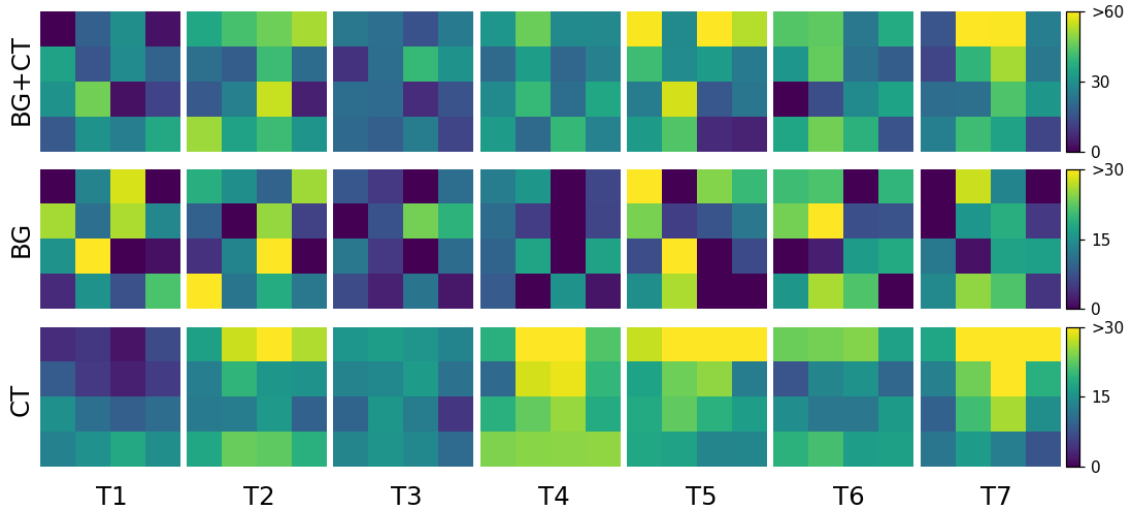

Figure 5.3. Zoom in of each trapping location bin with a 4x4 bin. Top: Mean counts for Background+Cross-talk (BG+CT), where target tweezer is turned off while others remain on to see effects of atoms trapped at neighboring sites on target tweezer's window. Middle: Background (BG) with no atoms present. Bottom: BG+CT-CT yielding cross-talk only. As can be seen crosstalk is highest on edges of 4x4 window. With this in mind performed remaining analysis using 2x2 window centered at middle of trapping sites to remove noise

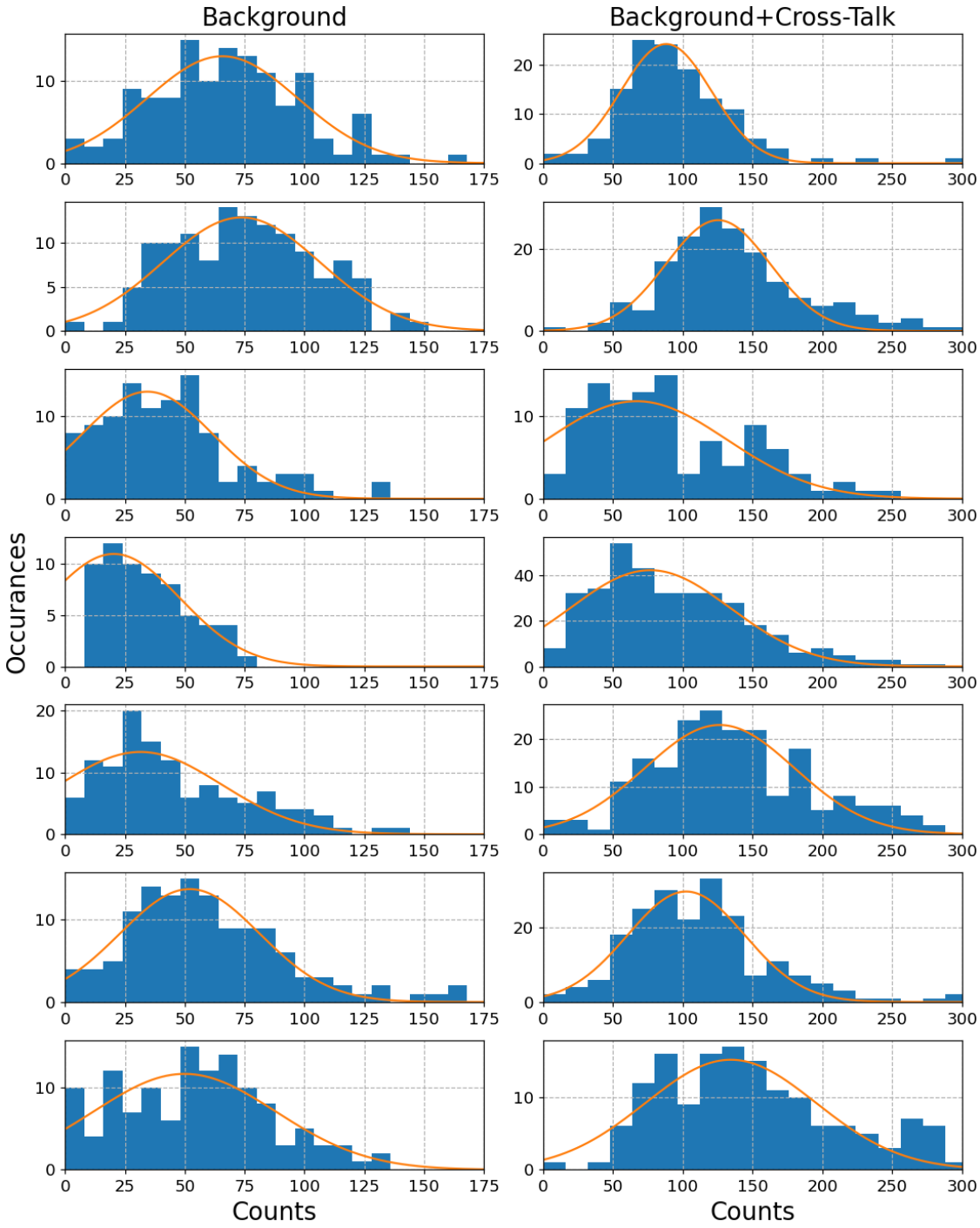

Figure 5.4. Left) Background data set histograms of the number of photons detected by CCD, (with a 2x2 pixel binning on each tweezer center), for each tweezer site with no atoms loaded in any tweezer. Right) Backgrounds + Cross-talk histograms, where the target tweezer was turned off while the rest of the tweezers remained on loading atoms. Photon counts histograms were fit with Gaussians, BG average mean photon counts of 47 per tweezer site, BG+CT 103 photon counts per tweezer site.

To analyze the effects of cross-talk on the photon counting rates for a given tweezer site, individual background data sets were taken for each site where the target tweezer was turned off while the others remained on and loading atoms. An additional background data set was taken with all tweezers off. We began analysis by using 4x4 pixel binnings centered on each atom to develop our counting statistics. Subtracting the all tweezers off background from the individual backgrounds with neighboring tweezers still loading we can view the effect of just cross-talk on each site (CT-Bottom row figure 5.2). The cross-talk predominantly resulted in counts near the bordering pixels of each individual tweezer, motivating the choice to reduce down to a 2x2 pixel binning on each site to increase our signal to noise ratio.

The individual tweezer backgrounds (B), and background+cross-talk (BC) were fit with Gaussian peaks yielding an average mean photon counts of 47 per tweezer for the background only datsets and 103 photon counts per tweezer for the background + cross-talk sets, these fits would be used for fitting the zero peaks in the subsequent tweezer loading analysis to reduce the number of free parameters.

Table 5.1. Fit parameters for background (BG) and background+cross-talk datasets (BG+CT) where the histograms of photon counts per experiment detected by an EMCCD with 2x2 pixel binning centered on each tweezer location, with each site was fitted to a Gaussian, centered at X_0 and with width σ

	BG		BG+CT	
$T\#$	X_0	σ	X_0	σ
1	65.7±2.5	31.5±2.6	88.1±1.5	32.4±1.5
2	73.7±2.2	32.8±2.3	125.3±2.25	37.3±2.2
3	34.4±2.3	27.2±2.6	66.9±9.8	64.6±10.8
4	20.3±2.3	27.7±1.8	76.7±4.4	57.4±4.9
5	31.5±4.6	33.8±4.9	126.4±4.5	53.6±4.5
6	52.1±1.6	29.2±1.7	102.4±2.9	41.9±2.9
7	49.9±4.3	38.2±4.8	134.4±5.8	61.2±5.9

5.2 Single Tweezer - No Neighbor

The next step was to look at the photon counting statistics of an individual tweezer while it's immediate neighbors were turned off but the remaining tweezers were on. The motivation for this was to see if the distinct atom number peaks in the detected photon counts from our previous single tweezer experiment could be reproduced under the new conditions of the tweezer array, this would provide the basis of where to expect our atom number peak centers for the subsequent experiments and place bounds upon our fitting parameters. We chose to take this measurement instead of our prior single atom data due to the fact that even with the neighboring site turned off there still is a larger potential well with 5 of 6 other tweezer beams turned on which would result in higher atom flux towards the chip's surface then when a single beam of the same power on by itself. To do so we reused the background+crosstalk dataset for tweezer number 6 where it itself was turned off, leaving tweezer 7 (bottom tweezer) on with no neighbor, eliminating most cross-talk effects. The top right image in fig 5.4 shows the mean photon counts detected per pixel for the 7 atom array over 200 experiment repetitions, with the yellow highlighted box depicting the pixel binning used for the site is centered on tweezer 7 (data shown is for 2x2 center of the box)

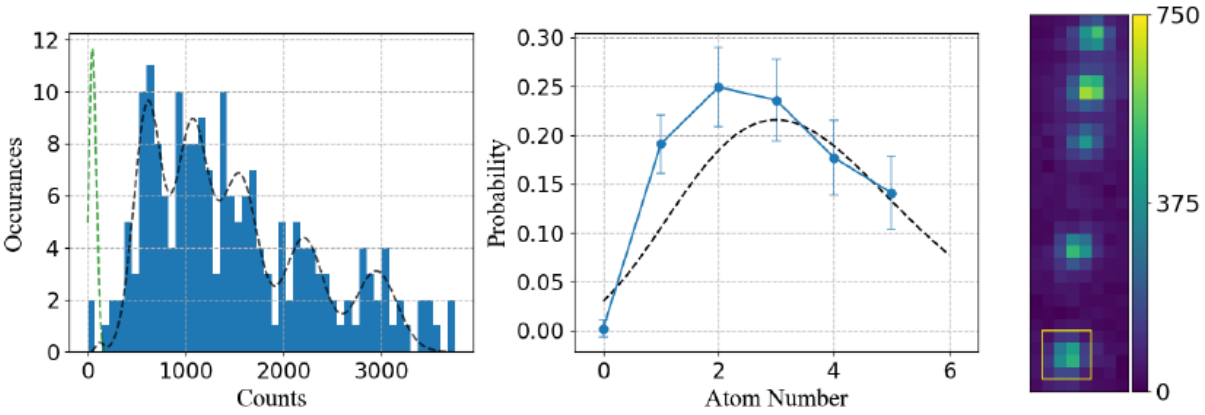

Peak	Amp	Center	Width	P	Peak Sep.
BG	1.95	49.90	38.20	0.01	0.00
1	9.41	611.39	141.74	0.18	561.49
2	8.68	1066.47	200.45	0.23	455.08
3	6.71	1553.87	245.50	0.22	487.40
4	4.36	2207.94	283.48	0.17	654.07
5	3.10	2946.02	316.94	0.13	738.08

Figure 5.5. Top Left) Histogram of photons detected per experiment for a single tweezer site with it's immediate neighbors turned off. Fitted to a sum of Gaussians (black dash) for each peak, background fit (green dash) shown scaled for reference. There are 5 discernible peaks beyond the background peak corresponding to 1-5 atoms trapped respectively. 99% chance to load at least one atom. The mean peak separation corresponds to about 576 photons per atom trapped, with the number of photons per atom appearing to increase slightly with atom number. Top Top Middle) Poissonian fit to atom-number loading probabilities. The fit yields a mean atom number of 3.43(.13), simply taking the mean of the atom number probabilities and attributing the 6% of events that fall beyond the 5th atom peak to correlate to 6 atoms yields a mean atom number of 2.99. Top Right) Zoom-out of mean counts per pixel for used data set with yellow box depicting pixel binning of data set (actual data uses 2x2 binning to reduce crosstalk). Bottom) Table of fit parameters for each Gaussian peak used to represent a given atom number. Amplitude in arbitrary units, P is the correctly scaled loading probability, other values given in terms of mean number of photon counts

Five distinct atom number peaks were observed corresponding to loading 1-5 atoms respectfully. Each of the peaks was fit with a Gaussian. Approximately 5% of the events had counts correlated to more than 5 atoms (the six atom peak is visible, higher counts were cut off from graph fig 5.4) but did not occur frequently enough to perform a meaningful fit for this dataset. After normalizing our peaks, it was determined that 99% of the time at least one atom is loaded into the tweezer. There were approximately 576 photons detected per atom trapped, with the photons/atom increasing with higher atom number, this may be attributed to a super-radience effect observed (broways citation) but due to the small number of atoms and involved and error in the less frequent occurring high atom counts it is difficult to draw a conclusion at the point.

$$P_N = \frac{m^N \mathrm{e}^{-m}}{N!} \tag{5.1}$$

Subsequently the atom number loading probabilities were fit to a Poisson distribution, where the 'P_N' is the probability to detect N atoms for a trap with mean atom number 'm'. The mean atom number trapped was calculated to be 3.43 ± 0.13 showing that in the absence of cross-talk, and other possible effect from the immediate neighboring tweezers, our trapping scheme works with a high degree of success, the atom number peak centers for photons detected will subsequently be used as a guide for fitting the datasets for loading all 7 tweezers

5.3 Loading 7 Tweezer Array

Having calibrated our system, we then proceeded to studying the atom number loading probabilities for each tweezer in a linear array of seven tweezers. The experiment was performed with the same conditions as prior, with each tweezer on and loading atoms, a trap depth of about 3mK per tweezer, and a tweezer spatial separation of about 3 microns on the

photonic chip's surface, and was repeated a little over a thousand times to develop enough photon counting statistics to performs fits.

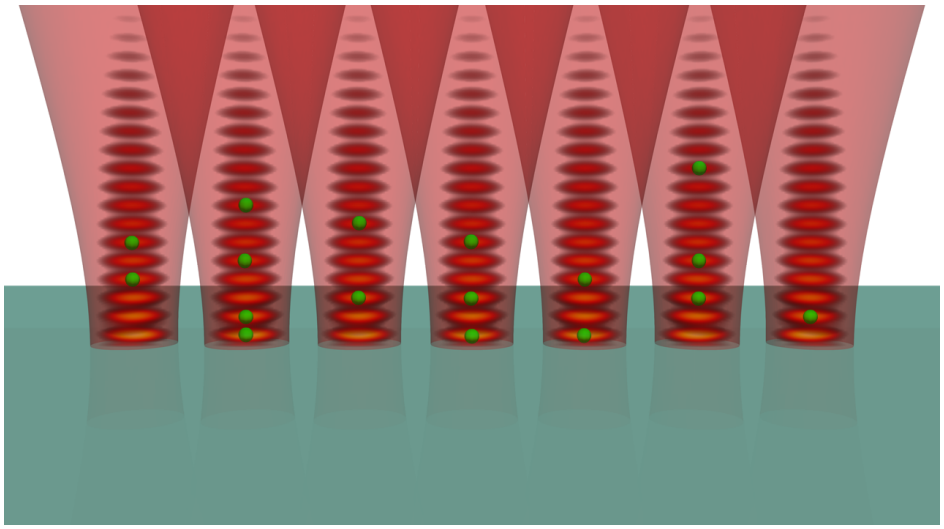

Figure 5.6. Atoms loading probabilistically into lattice sites for a 7 tweezer array ontop of a photonic chip. Each tweezers reflection on the surface produces a small 1-D lattice with 15-20 defined trapping locations. Each tweezer probabilistically loads N atoms (green balls) per experiment into random sites thought the lattice

Histograms were constructed for the number of photons detected per experiment for each tweezer using a 2x2 EMCCD pixel binning (Fig 5.6) for each. One of the first differences that becomes clear comparing the full loading histograms to the single site no neighbor histogram (Fig 5.4), is the reduced visibility of the atom number peaks for each site. Some sites only have 1 or 2 discernible peaks, while others have multiple single bin peaks and troughs making it difficult to establish if a peak is actually there or not. In additon, one of the data sets, tweezer 5 (3rd from bottom), had a greatly reduced loading rate from the single tweezer site. The one positive of the lower mean atom number is that it had a pronounced no atom peak which fit very well to the background +cross-talk dataset's fits from earlier. Most concerning was that site 7 in this dataset is the same location we chose for the single tweezer no neighbor histograms, but as can be seen it's mean atom number was greatly reduced and it's peaks as well have greatly reduced contrast.

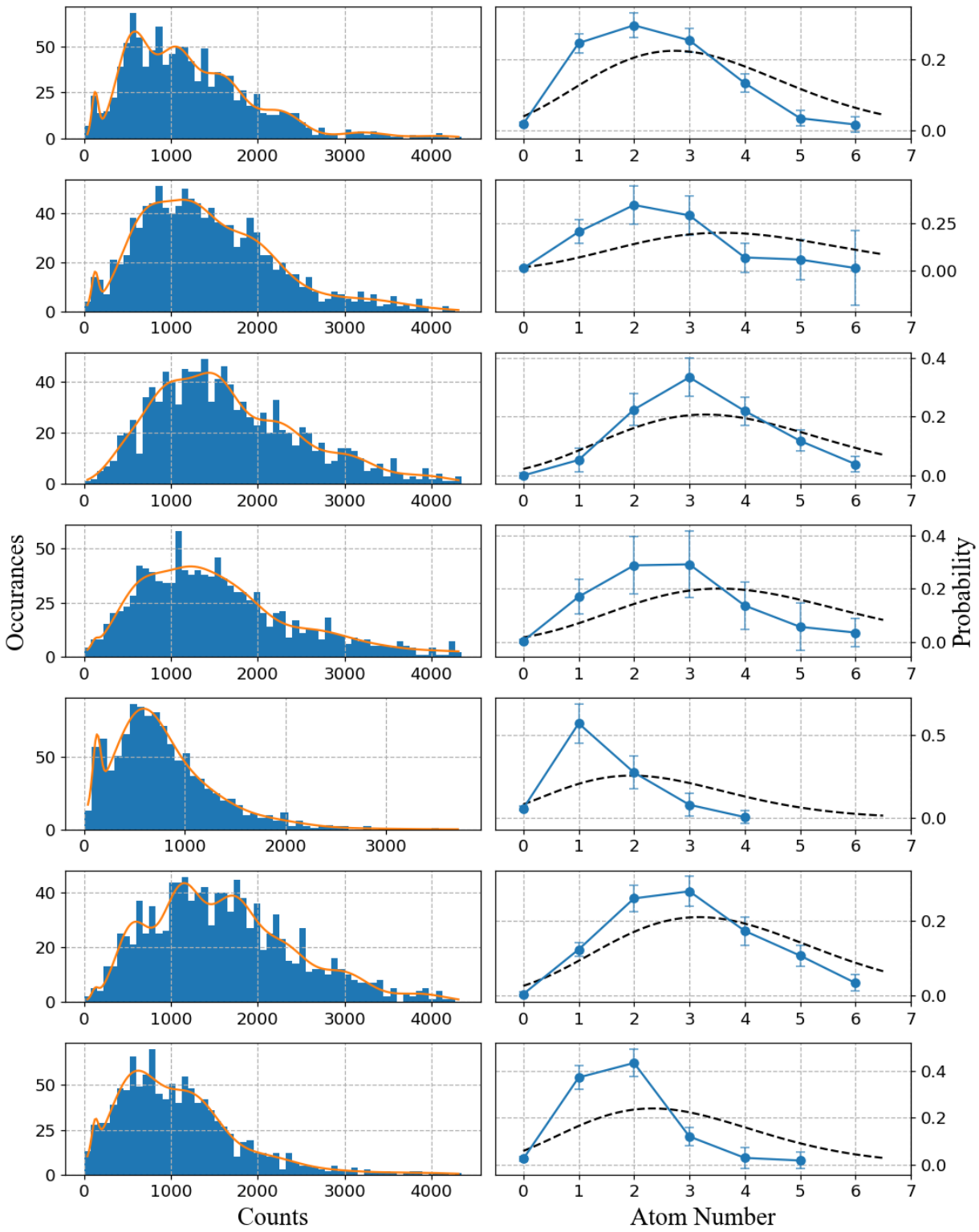

Figure 5.7. Left) histograms for the number of photons detected per experiment for each Tweezer (T1 at top, T7 at bot.), calculated gaussian fits in orange. Right) Calculated atom-number probabilities for each tweezer site fit to poisson distribution.

$$O(N) = A_0 \mathrm{e}^{-(N-\mu_0)^2/(2\sigma_{bc}^2)}\ A_1 \mathrm{e}^{(-(N-\mu_1)^2/(2\sigma_1^2)}\ + A_2 \mathrm{e}^{-(N-\mu_2)^2/(2\sqrt{2}\sigma_1^2)}$$
$$+ A_3 \mathrm{e}^{-(N-\mu_3)^2/(2\sqrt{3}\sigma_1^2)}\ + A_4 \mathrm{e}^{-(N-\mu_4)^2/(2\sqrt{4}\sigma_1^2)}\ + A_5 \mathrm{e}^{-(N-\mu_5)^2/(2\sqrt{5}\sigma_1^2)}\ + A_6 \mathrm{e}^{-(N-\mu_6)^2/(2\sqrt{6}\sigma_1^2)} \tag{5.2}$$

The histograms were fit to a sum of up to 7 Gaussians, (eqn 5.2), where N is the number of photons detected (counts), O(N) is the occurrence of N photon detection's, A_N are the amplitudes (proportional to the probability of loading N atoms), μ_i are the peak centers and σ_i are the peak widths. The first peaks were fit using constraints from the background+crosstalk peaks with only a free amplitude scaling, while the atom number peak centers were given bounds based on the peak centers seen previously with the single tweezer no neighbor data sets. To reduce the number of free parameters, the width of the atom number peaks for $N > 1$ were all scaled in terms of the one atom peak width assuming, $\sigma_N = \sqrt{(N)}\sigma_1$ obeying Poissonian statistics.

The fits/histograms were cut at up to 6 atoms, there were additional detection's with counts corresponding to more than 6 atoms but were not able to be fit accurately due to their rare occurrence and larger widths. The subsequent atom number probabilities for each tweezer were then fit to Poissonian functions, with the probability scaling taking into account the cut data points.

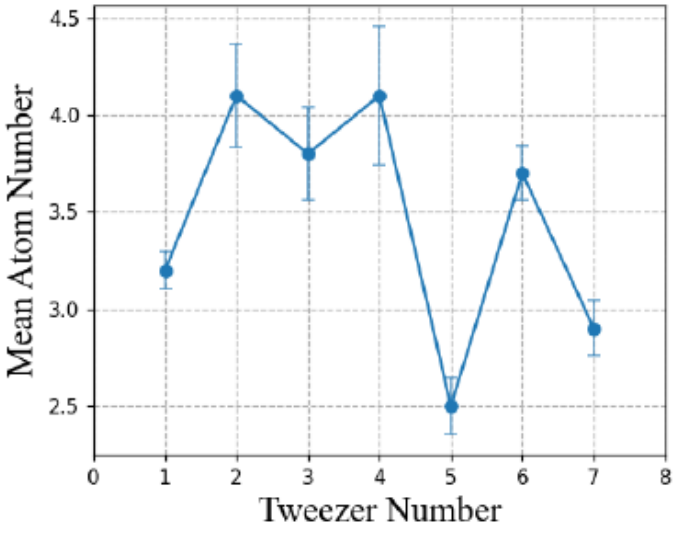

$T\#$	$P_{N>0}$	$\bar{N}$
1	98.21(.45)%	3.25(.01)
2	98.85(.46)%	4.10(.26)
3	100.00(.85)%	3.80(.24)
4	99.63(.74)%	4.05(.36)
5	94.06(1.32)%	2.48(.15)
6	99.71(.51)%	3.68(.14)
7	97.60(.95)%	2.85(.14)

Figure 5.8. Individual tweezer atom loading probabilities derived from Poissonian fits. The average mean atom number for the tweezer array was 3.45 atoms/tweezer with and average probability of 98.29% to load at least one atom per tweezer

As the histogram fitting was unable to convincingly discern a single experiments atom count, a second methodology was used to determine the rate at which all 7 tweezers loaded at least one atom. We implemented a discriminator method where in if a tweezer site resulted in a detection of a number of photons greater than the 95 percentile mark of that sites background+cross-talk measurements, T1-7 (157, 240, 185, 205, 242, 201, 282) yielding trapping 1 or more atom probabilities of $P_{N>0}$ T1-7 (97.1%, 97.1%, 99.5%, 98.4%, 87.2%, 99.2%, 92.0%), slightly lower than the Gaussian fits predicted so we can consider these as a minimum bound. Using this method, we were able to determine that in at least 74.2% of experiments all 7 tweezers loaded at least one atom, demonstrating our apparatus is capable of preparing loading atoms into a 7 tweezer array with high probability which may be increased with better balancing of the power distribution between the tweezers in the array.

6. ATOM-CAVITY COUPLING

Having demonstrated our ability to trap atoms in close proximity to the surface of our micro-ring resonators our next milestone will be demonstrating that we are capable of observing atom-cavity coupling. In order to perform these experiments we will need to the capability to probe the atom-resonator system using single photons, perform time tagged counting of photons exiting the bus waveguide, and spectroscopicly determine our micro-rings resonant wavelength to ensure it is aligned with the target atomic transitions wavelength. To facilitate these measurements an optical probing station was constructed and coupled to the fiber connections to our photonic-chip.

Our probing station provides optical connections to the bus waveguide coupled to our target micro-ring resonator, as well as multiple light detection stages. The probe station begins with a DBR laser centered near cesium's D1 transition (for broadly probing the micro-rings resonance) and a very low power locked D1 slave laser (referred to simply as the probe beam), both of which are coupled into the two inputs of a 99/1 beam-splitter (fig 6.1). Both beams pass through clean up cubes followed by QWP HWP pairs to align the input light unto the bus waveguide's TM mode before entering one of the two input ports of a 99/1 fiber beams-splitter with the DBR coupled to the 99% input and the probe beam coupled to the 1% port.

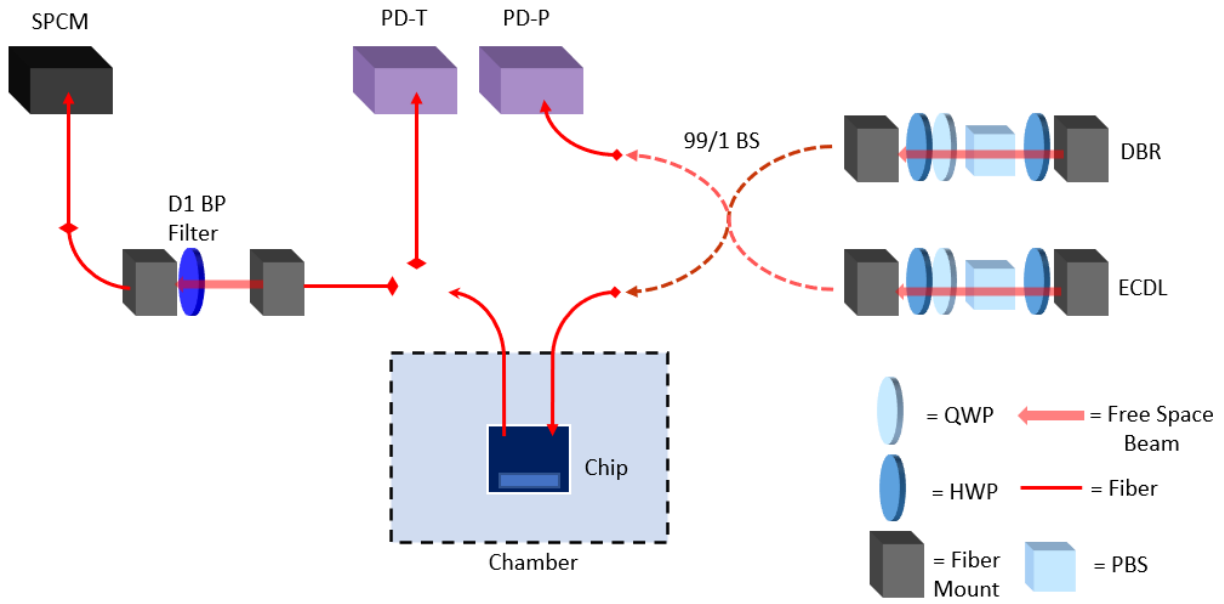

Figure 6.1. Probing station schematic for sending in and detecting single photons from micro-ring resonator. Light from a DBR laser and a OPLL locked ECDL pass through clean up cubes followed by a QWP HWP pair to align the input light unto the bus waveguide's TM mode before entering one of the two input ports of a 99/1 fiber beams-splitter (DBR-99, Probe-1). The 1% pick off line output is coupled to a Newport 2051 photo-diode for monitoring changes in input power during resonance measurements. The 99% fiber line enters the vacuum chamber via a Teflon fiber feed-through, is connected to a bus waveguide on the photonic chip which is evanescently coupled to the target micro-ring resonator, then sent back out of the chamber via another output fiber. The output contains the transmitted light after interacting with the atom-cavity system. The transmitted light is either fiber connected to a second Newport 2051 photo-diode for monitoring during polarization alignment, or sent to an Excilitas single photon counting module (SPCM) after passing through a D1 band-pass filter to generate detection events which are subsequently counted by a Fastcom MCS6A MCS6A 100 ps per time bin, multiple-event time digitizer

The 99% output port is fiber connected to the photonic chip input fiber, sending light into the bus waveguide towards the resonator. The 1% output port is connect to a Newport amplified photo-diode and used to calibrate the input power during broad resonance scans of the micro-ring. The photonic chip output fiber is connected either to a second Newport detector for monitoring transmission during broad resonance scans, or a fiber leading to a

single photon counting stage during experiments, consisting of a D1 band-pass filter centered near 895nm supplying 10^{-12} attenuation, followed by a shielded fiber that couples light into an Excilitas AQR series single photon counting module (SPCM). Photon detection events are monitored via a Fastcom MCS6A 100 ps per time bin, multiple-event time digitizer which counts the number of photon detections made by the SPCM and time tags them with a programmable time bin and number of bins.

The current generation photonic chip implements micro-ring resonators which can support multiple resonant wavelengths, two of these modes are used for atom light interactions, one slightly blue detuned (10's to 100GHz detuning) from Cesium's D1 transition at 894nm and a second similarly detuned from Cesium's D2 transition at 852nm. In order to couple a trapped atom to the micro-ring, the micro-ring must have it's resonance tuned to overlap with the desired atomic resonance. To do this we implement a 1064nm Nd:YAG laser as a heating source, with the beam sent from the bottom of the chamber, incident upon the photonic-chip's silicon substrate nearby the window. A small amount of the beams power is absorbed by the silicon and heats the chip and hence the micro-rings, lowering the resonance frequency via thermal expansion and Si_3N_4's thermo-optic coefficient increasing the index of refraction with temperature, resulting in a net shift of $\delta\omega_0 \approx$-0.5GHz/mW of heating light (in situ alignment of the heating beam onto the chip will lead to slightly increased or decreased performance).

Connecting the photonic-chip output port to the Newport detector, the DBR laser is used to broadly scan the micro-ring's resonance frequency for initial resonance tuning. The DBR's frequency is measured via a pick off beam with is fed to a High-Finese wave-meter. The temperature controller for the D1 DBR was modified to allow control via it's initially designed trim-pot, as well as a separate analog control input. A labview program was constructed to step the DBR temperature controller to change the lasers frequency, pause for a few ms for the thermal lock to settle, read the wave-meter, then record the voltage from the pair of Newport detectors for inferring the ratio of transmitted to input light.

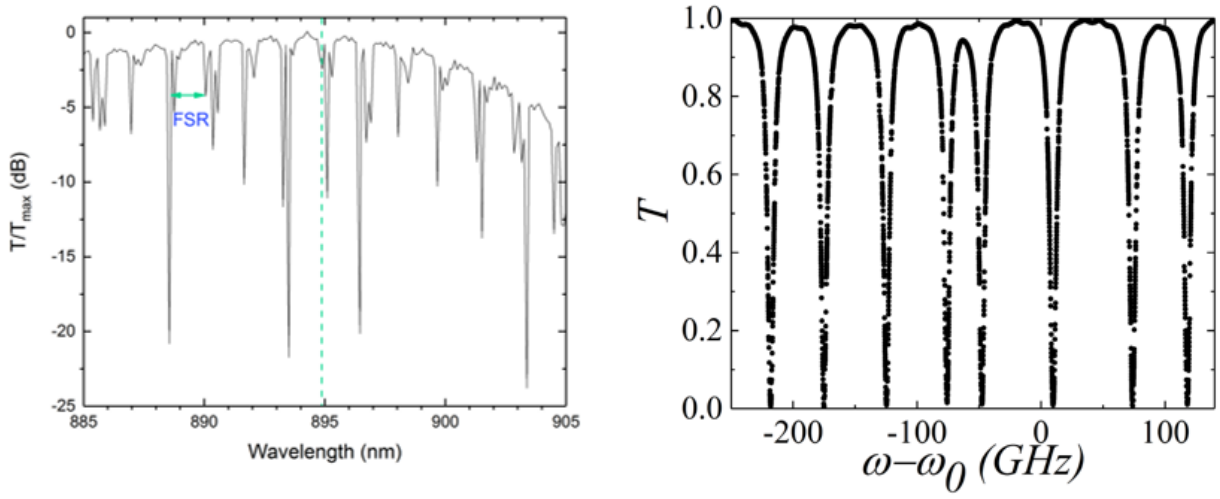

Figure 6.2. Micro-ring transmission scans for our first generation (left) and current generation (right) photonic chips. Out first generation chip had not yet achieved critical coupling of the bus waveguide to the ring and as can be seen transmission does not drop to zero on resonance unlike our current generation. The two scans are taken over different frequency ranges, with the broad scan of the old device demonstrating a few closely packed peaks arising from each micro-ring at a slightly difference resonance, repeated every FSR (about 500 GHz). The current generation chip, beyond achieving critical coupling with near zero transmission on resonance, supports additional resonance series to simultaneously allow resonant modes at Cesium's D1 (894nm) and D2 (852nm) transitions, as well as Cesium's red (935) and blue (793nm) 'magic' wavelengths for use in evanescent trapping schemes

The detector connected to the photonic-chip output port monitors the transmission as a function of frequency, while the second detector connected to the 1% pick-off port monitors the relative power of the beam as changing the temperature can effect the overall output power of the DBR.

To begin a measurement, the polarization of the probe laser is tuned to the waveguides TM mode via previously mentioned HWP QWP pair by minimizing the transmitted light detected using a photo-detector. After polarization alignment, the scan is performed and the scaled transmittance vs frequency is calculated allowing us to see broadly how far away from atomic resonance the target micro-ring resonance is. Once we are within a few GHz of the target frequency, the DBR input beam is shuttered and the D1 probe beam locked to atomic resonance is unshuttered. The probe beams lock point is set to atomic resonance which can be measured by performing an experiment using the PGC cloud where atoms are pumped into cesium's F=3 ground state prior to turning off the PGC beams followed by absorption imaging. A weak pulse (P<1mW) from the D1 probe beam is sent into the micro-ring prior to the imaging pulse which utilizes Cesium D2, F=4-5 light. When the D1 probe is off resonance the cloud remains in the dark state and no atoms are detected, when the probe beam is on atomic resonance, leakage light from the fiber-Bus wave guide mating U-grove emits out in a cone pumping atoms from F=3 to F=4, allowing them to be detected during the absorption imaging process.

With the D1 probe set to atomic resonance, an electronic variable optical attenuator is then used to attenuate the beam by up to 30dB allowing for single photon probing of the atom-microring system. The photonic chip output fiber is then disconnected from the Newport detector and connected to the SPCM stage. Using the MCS6A and SPCM, the micro-ring is fine tuned to resonance with the heating beam by minimizing the photon transmission rate of the locked probe beam. The attenuated probe beam with the SPCM is used for this final calibration as the higher probe power required for the Newport photo-diode

measurement may heat the micro-ring and shift the resonance during probing, potentially leaving the ring up to a GHz off resonance during the actual experiment at low power.

6.1 Probing atom-waveguide coupling

Now with the probing scheme prepared, we must first know what signal to look for which indicates atom-resonator coupling, we begin by presenting a model of how an input mode couples to a WGM in the resonator. For the case of a micro-ring resonator with only two counter propagating resonant modes (ignoring all modes separated by integer FSRs), the field can be described by a clockwise(CW) mode ($\vec{E_-}(\vec{r},t)$) with amplitude (a_-) and a counter clockwise propagating mode ($\vec{E_+}(\vec{r},t)$) with amplitude (a_+), where ($\Delta\omega = \omega - \omega_0$) is the detuning from resonance, β is the coherent back-scattering rate, ξ is the scattering phase shift, and $\kappa = \kappa_\mathrm{i} + \kappa_c$ is the total loss rate of the resonator due to the resonators intrinsic loss rate κ_i and the coupling loss rate to the bus wave guide κ_c

$$\vec{E}(\vec{r},t) = a_+(t)\vec{E_+}(\vec{r},t) + a_-(t)\vec{E_-}(\vec{r},t) \tag{6.1}$$

$$\frac{da_+}{dt} = -(\kappa/2 + \mathrm{i}\Delta\omega)a_+(t) + \mathrm{i}\beta\mathrm{e}^{\mathrm{i}\xi}a_-(t) \tag{6.2}$$

$$\frac{da_-}{dt} = -(\kappa/2 + \mathrm{i}\Delta\omega)a_-(t) + \mathrm{i}\beta\mathrm{e}^{-\mathrm{i}\xi}a_+(t) \tag{6.3}$$

Even though the bus waveguide coupling will only seed the CW or CCW mode, coherent back-scattering causes mode mixing resulting in two standing wave modes separated in frequency by the back-scattering rate β given by

$$\vec{E_1}(\vec{r},t) = \sqrt{2}\mathrm{e}^{-\mathrm{i}\xi/2}\left[(E_\rho\hat{\rho} + E_z\hat{z})cos(m\phi + \xi/2) - E_\phi sin(m\phi + \xi/2)\hat{\phi}\right]\mathrm{e}^{-\mathrm{i}\omega t} \tag{6.4}$$

$$\vec{E_1}(\vec{r},t) = \mathrm{i}\sqrt{2}\mathrm{e}^{-\mathrm{i}\xi/2}\left[(E_\rho\hat{\rho} + E_z\hat{z})sin(m\phi + \xi/2) + E_\phi cos(m\phi + \xi/2)\hat{\phi}\right]\mathrm{e}^{-\mathrm{i}\omega t} \tag{6.5}$$

When an atom is trapped above the micro-ring resonator, it couples to the device with strength g, where d is the reduced dipole moment, $V_m = A_m L$ is the mode volume, A_m is the mode area for an atom trapped height z above the ring, L is the length of the resonator, and (ρ_a, z_b) represent the location of the atom relative to the waveguide. For our system with an atom trapped 100nm above the surface of the micro-ring, the mode volume is approximately $V_m \approx 500\mu m^3$ giving a coupling strength of $g = 2\pi \cdot 178$ MHz.

$$g = d\sqrt{\frac{\omega}{2\hbar\epsilon_0 V_m}} \tag{6.6}$$

$$V_m = A_m(\rho_a, z_a)L \tag{6.7}$$

$$A_m(\rho_a, z_a) = \int \frac{\epsilon(\rho, z)\left|\vec{E}(\rho z)\right|^2}{\epsilon(\rho, z)\left|\vec{E}(\rho, z)\right|} d\rho dz \tag{6.8}$$

$$g = \sqrt{\frac{3\lambda^3\omega\gamma}{16\pi^2 V_m}} \tag{6.9}$$

When an atom is coupled the transmission dip of the spectrum when the cavity is on resonance is modified with a narrow peak on atomic resonance, (Fig 6.2-black). As mentioned before this peak arises as the cavity-atom system couples forming a pair of dressed states with resonances separated by the coupling strength g, causing destructive interference for photons coupling to the cavity from the bus waveguide at the bare atomic resonance, removing the dip in transmission at that frequency

$$T(\delta) = \left|\frac{g^2 + (\mathrm{i}\delta + \Gamma/2)(\mathrm{i}\delta + (\kappa_\mathrm{i} - \kappa_c)/2)}{g^2 + (\mathrm{i}\delta + \Gamma/2)(\mathrm{i}\delta + \kappa/2)}\right|^2 \tag{6.10}$$

$$T(0) \sim 1 - \frac{\kappa\Gamma}{2g^2} \tag{6.11}$$

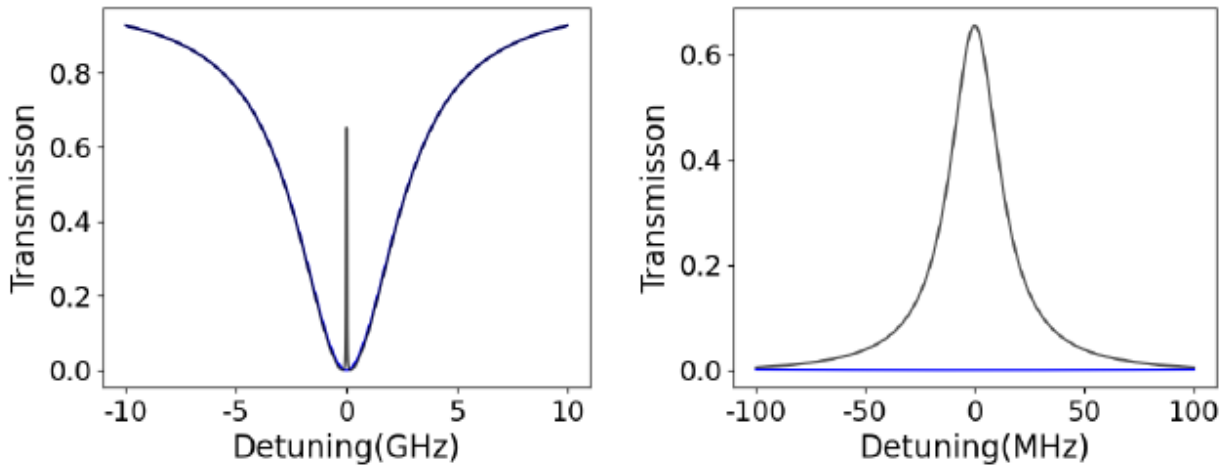

Figure 6.3. Waveguide transmission spectrum for a bus waveguide critically coupled ($\kappa_c = \kappa_\mathrm{i} = 2\pi \cdot 2.6GHz$) to a micro-ring resonator with (black) and without (blue) an trapped 100 nm above the surface coupled with strength $g = 2\pi \cdot 178MHz$, right is a zoom in of the atomic resonance feature leading to greatly increased transmission

To probe whether an atom is coupled to the cavity we have performed two experiments; one where the PGC beams are simply turned off, allowing the cloud to simply fall onto the target ring with atoms probabilistically passing into the region of space close enough to the micro-ring and couple to the cavity modes, the other being the originally intended plan of trapping atoms directly above the surface using the optical tweezer. For the cloud drop method, using the mode volume defined by an atom 100nm above the rail, with our estimates of the atom density above the surface we predict 1-2 atoms to transit through this region per ms, with $10 - 20\mu K$ atoms having approximately $2\mu s$ of interaction time with the ring before leaving the interaction region or being absorbed onto the surface. With an excited state lifetime of about 200ns, a transiting cesium atom can scatter about ten photons during that time. For the case of an atom trapped in a tweezer, it allows for an atom to interact for a much longer time period but only has a small probability of loading into the bottom-most site to be coupled strongly enough to the ring for detection.

Using these parameters the probe photon input rate is set to between 10 to 20 per microsecond. Unfortunately our system has various loss sources from probe input to detection. The bus waveguide U groove where the lensed fiber is docked transmits only approximately 25% of the incident light at both ends with the rest lost, the free-space to free-space fiber connection with the D1 bandpass filters has a fiber coupling efficiency of 80%, and the SPCM has a detection efficiency of only 40% at cesium's D1 wavelength. All of this together yields an $\eta = 2\%$, so the D1 probe beam is attenuated via the VOA such that the MCS6A observes 0.2-0.4 counts per microsecond.

The experiments begin with the same atomic cloud preparation as prior. Next, as we intended to probe the atom coupling using cesium's D1 $F = 3 \rightarrow F = 4$ transition, atoms are pumped into the F=3 state before the cooling beams are turned off by turning off the F=3 repumper seed light to the TA for about 2ms prior to turning off the cooling light. With no light to pump out of the F=3 dark state atoms rapidly accumulate there. Subsequently the probe sequence is started. To prevent power noise from thermal drift in the AOM controlling the probe beam, the AOM is left on for the bulk of the experiments duty cycle with a mechanical shutter being used to block the light. The shutter has an open/close time of approximately 10ms and is not opened until directly before the probe sequence.

The probing sequence is started by a trigger pulse sent to the MCS6A. The MCS6A is programmed to perform counting measurements using approximately $1\mu s$ time bins and a total number of bins set by the probing sequence time. For the cloud drop experiment, the PGC beams are turned off at the edge of the MCS6A start trigger, allowing the atoms to free fall towards the surface. The probe beam is left on for 2ms while the MCS6A counts detection pulses from the SPCM. During this time The PGC beams are re-enabled at very low power and tuned into resonance with cesium's 4-4 transition for repumping into the F=3 ground stats as after absorbing a cavity photon the atom has a chance to decay to the F=4 ground state which is dark to the probe beam so it must have a repumping element to continue scattering photons. The probe is then shut off for 2ms while the background counts

are measured. All beams are then disabled for a 15 ms period to allow atoms to fully escape the trapping region and fall to the surface. The PGC and probe beams are then re-enabled for 15-30 ms to prevent thermal drift of the resonator, followed by a repeat probe cycle with the PGC beams tuned to low power for re-pumping and a 2ms probe cycle followed by a second 2ms background measurement.

The integrated counts in the two 2ms probing sequences are then used to calculate the ratio of transmitted photons for when atoms are present vs the no atom case for each experimental repetition. For the case of an atom trapped via tweezer, the ratio can be very large as a perfect critically coupled micro-ring would transmit zero photons when an atom is not present, in our system we observe the waveguide transmission decrease to about 3% when the probe beam is on resonance and calculate a transmission increase to 65% when on resonance with an atom trapped 100nm above the surface. For a photon input rate of $10/\mu$ s, we expect approximately 50 detection's with a shot noise level of 15%, when an atom is trapped, we would expect the number of detections to rise to about 1000 providing a very large signal to noise ratio. For the cloud drop method, the probability of probing when an atom is present drops the signal by a factor of a thousand, putting us below the shot noise level.

Using a Poisson distribution for a mean counts of 50 photons per 2000 $1\mu s$ predicts a single photon detection per time bin probability of 2.43%, 2 photon/bin $P = 0.03\%$, and only a 0.00026% probability of observing 3 or more photons, but when an atom transits through the interactions range of the resonator there is a 1.78% of seeing 3 or more photons per event, a nearly 7000 fold increase. With about 4 atom transits per experiment and performing 50 measurements, the probability of seeing three or more photons is still almost zero for the no atom case, so even a single event per experiment can be correlated to having an atom present. Using this, we decided to switch to a discriminator method for observing signal by measuring the ratio of 3 or more photons per bin events for when atoms are present vs the no atom case.

7. CURRENT AND FUTURE WORKS

7.1 Current Work Probing Atom-Cavity Coupling

To date we have not observed signal indicating atom-cavity coupling for a resonator. Our first attempt to observe coupling was implemented using the top tweezer lattice only to trap atoms above the resonator, we have recently reintroduced the back beam to allow for conveyoring of the atoms towards the surfaces during the probing pulses. In our original work with the conveyor belt we utilized an AOM controlling the back beam to redshift it's frequency relative to the top tweezer lattice. While we did successfully conveyor atoms towards the surface, we also observed phase noise between the top tweezer and bottom beam on the order of 2π radians at 200 Hz.

Both beams originate from a TiSaph laser in a separate room with the light brought onto our optical table using two separate 10m fibers, along with multiple other fiber-fiber connections, we believe this is the source of the phase noise. To remove the noise we implemented a phase lock between the beams using a fiber phase shifter capable of ($> 50\pi$) total shift and a bandwidth greater than 10kHz. Using the fiber phase shifter we are able to remove the phase noise as well as directly modulate the beam to red detune for conveyoring atoms coherently, this may remove possible heating that occurs during shuttling due to the noise. Since we cannot optically determine which lattice site the atom is loaded into we implement a shuttling scheme moving a distance of N-1 lattice sites where site N is the most probable lattice site for an atom to load as predicted by the monte-carlo simulations and site 1 is the bottom most lattice site coupled to the micro-ring.

Additionally we are looking at trapping techniques not involving the top tweezer lattice, including novel evanescent trapping schemes, discussed below, as well as improvements for our atom cloud drop method. The easiest way to increase the atomic flux towards the micro-ring and improve the probability of probing during an atom transit event is by simply using the higher power back beam focused on the micro-ring creating an attractive potential near

the surface. While this setup does not create a stable trap above the surface, the beam is much stronger than our optical tweezer and less tightly focused so it will provide a large potential well which can pull atoms downwards towards the ring increasing are likelihood of probing the while an atom is in transit near the evanescent interaction range.

7.2 Evanescent Trapping Scheme

Our recent generation photonic chips were engineered to facilitate resonances near Cesium's D1 and D2 resonance, as well as two additional wavelengths; cesium's previously mentioned magic wavelength at 935.3 nm and a second blue detuned magic wavelength at 793.5 nm. The D1/D2 modes will be used for probing atom coupling and other processes in future experiments, while the two modes near cesium's magic wavelengths will be used to implement a 2 color evanescent wave trap allowing for an improved method of trapping atoms in close proximity to the surface of our nanophotonic structures.

To understand how the evanescent trap works, we will begin with a description of the field inside the micro-ring resonator when it is being excited by light coupled to the bus waveguide. Injecting light into the bus waveguide from the right(left) side $|s_{\pm}|^2$ couples to the CCW(CW) mode only. For a lossless coupler, the coupling constant $K = \mathrm{i}\sqrt{\kappa_c}$ yields steady state mode amplitudes $a_+(a_-)$,

$$\begin{aligned} a_+ &= K\frac{\alpha s_+ + \mathrm{i}\beta s_-}{\alpha^2+\beta^2} \\ a_- &= K\frac{\mathrm{i}\beta^* s_+ \alpha s_-}{\alpha^2+\beta^2} \end{aligned} \tag{7.1}$$

where $\alpha = \kappa/2 + \mathrm{i}\Delta\omega$ andβ is the coherent back-scattering rate. Exciting the resonator from one direction leads to an intra-resonator electric field $\vec{E}^{\pm}$, where the sign indicates the direction of the input light $s_+(s_-)$

$$\vec{E}^{\pm} = \frac{\alpha K s_{\pm}}{\alpha^2+\beta^2}\left[\vec{E}_{\pm}(\vec{r}) + \frac{\mathrm{i}\beta \mathrm{e}^{\mp \mathrm{i}\eta}}{\alpha}\vec{E}_{\mp}(\vec{r})\right] \tag{7.2}$$

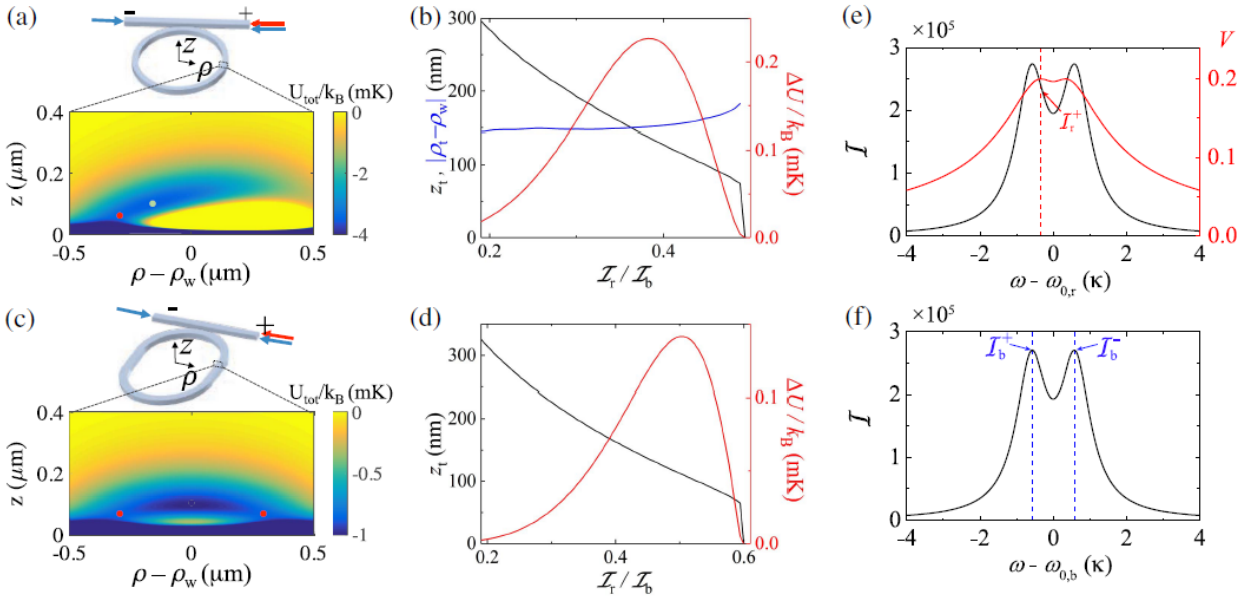

Figure 7.1. Two color evanescent trapping scheme for a micro-ring (a,b) and a racetrack resonator (c,d). For both, red light is injected from a single side (+), producing a standing wave potential, while blue light is injected from either end (+/-) producing a uniform evanescent field. (a,c) transverse cross section of evanescent trapping potential with z=0 corresponding to surface of resonator, red dots depict saddle points of potential where trap is no longer stable. (b,d) black represents trap center height above wave-guide as a function of the ratio of the build up factor ratio for red to blue injection light, red is the trap depth of the resultant potential well, blue depicts the radial shift of the trap center for the micro-ring resonator demonstrating near uniform trap position. (e,f) black depicts the build-up factor for red/blue light verses detuning from single mode resonance. Red light detuning is chosen to maximize visibility of intensity corrugation and eliminate vector light shift. Blue light detuning is chosen symmetrically about center to eliminate vector light shift as well as visibility of intensity corrugation resulting in smooth evanescent field

The coherent back-scattering leads to cross coupling between the CW and CWW mode, resulting in a standing wave pattern with intensity

$$\left|\vec{E}^{\pm}(\vec{r})\right|^2 = \mathcal{I}|\mathcal{E}(\rho,z)|^2[1 \pm V(\rho,z)sin(2m\phi + \xi_{\pm})] \tag{7.3}$$

where $\mathcal{I}$ is the frequency dependent build up factor,

$$\mathcal{I} = \mathcal{I}_0 \frac{|\alpha|^2 + \beta^2}{|\alpha + \beta|^2} \tag{7.4}$$

$$\mathcal{I}_0 = \frac{\kappa_c \mathcal{P}_w}{\hbar\omega} \tag{7.5}$$

V is the visibility of the standing wave describing the contrast of the standing wave peaks and troughs, and v is a visibility amplitude factor (v≈0.2 for TM mode used in our experiment)

$$V(\rho, z) = \frac{2|\alpha|\beta}{|\alpha|^2 + \beta^2}\, v(\rho, z) \tag{7.6}$$

$$v(\rho, z) = 1 - \frac{2|\mathcal{E}_\phi|^2}{\mathcal{E}^2} \tag{7.7}$$

The standing wave pattern for the single side injection of red light creates a desirable confining longitudinal lattice along the resonator with lattice constant (d=290nm) but does not provide transverse confinement, hence the need for a blue detuned repulsive dipole beam as well to cap the potential wells and prevent the atom from being pulled into the surface. However a single side injection of blue light would generate a second repulsive longitudinal lattice that with nodes/anti-nodes out of phase with the red lattice. To solve this problem, blue light is injected from both sides of the resonator with symmetric detuning from the resonator mode $\omega_{0,b}$ the resultant field cancels out the intensity corrugation providing a smooth longitudinally invariant potential which in combination with the red detuned light can form a stable evanescent trapping lattice. Adjusting the ratio of the build of factors $\mathcal{I}_r/\mathcal{I}_b$ allows for tuning of the trap height (z_{trap}) above the surface of the structure that the lattice potential minimas form, with the ability to create a trap 100nm above the structures surface with a trap depth on the order of 100-200μK which should suffice for loading from our atom cloud which is cooled to approximately 20μK prior to trapping.

Evanescent wave trapping will immediately offer several advantages over the tweezer lattice trapping scheme. First and foremost, the longitudinal modes only have a single minima

at the target height above the surface, there are no longer any trapping sites than can shield atoms from entering the interaction region with the resonator. While we have demonstrated our ability to shuttle atoms, the process would severely complicate our loading scheme as we would have to perform a lattice increment of conveyoring, followed by a transmission probe to detect if an atom is coupled, repeated 5-10 times per site until an atom is detected, then an individually addressed optical pumping to place that site into a dark state of the probe beam. This may be feasible for a small number of atoms but extending to larger numbers may prove impractical.

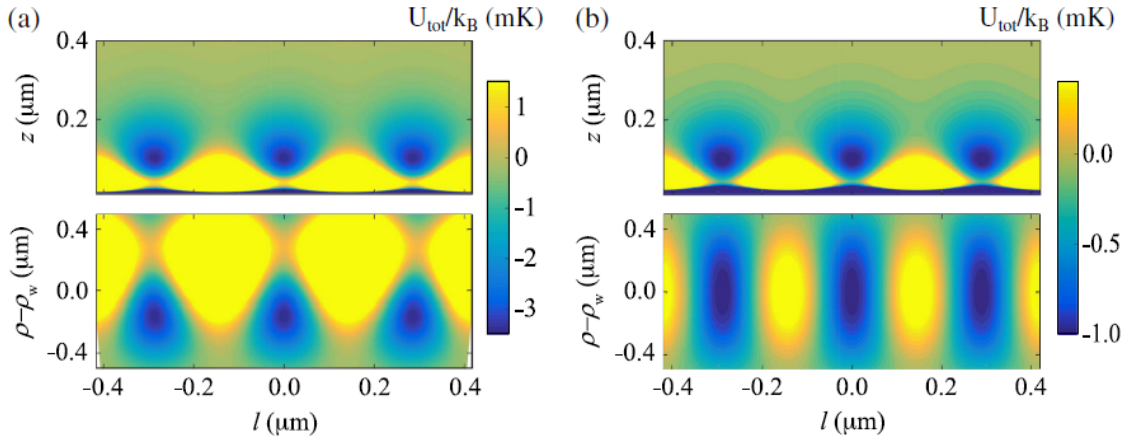

Figure 7.2. Evanescent field lattice potential formed by injection of blue light from both sides, with frequencies symmetrically detuned $\omega_{\pm} = \omega_{0,b} \pm \delta\omega/2$, and injection of red light from a single side for a microring (a) and a racetrack resonator (b).Top, cross section of longitudinal mode a waveguide center, bottom, cross-section through ρ, l plane at fixed $z = z_{trap}$

The collisional blockade effect would also ensure there is only 1 atom per lattice site, so we would not have to worry about an undetected atom trapped nearby that may interfere with a given operation. We will not have to probe the ring for our initial loading step as there is only a single vertical trapping site, so we can use a single round of florescence imaging to determine which sites were populated during loading. We reduce system geometric limitations from localizing atoms via an array produced by two AOD's, as the beam passes through both AOD's shifting a single tones frequency effects all sites interfered with that note preventing

independent control of each trapping location, this may not be an issue for a few atoms but does limit possibilities for tens or more atoms. Also the system no longer requires a user alignment of the trapping beam, so there is less source of error for instance of having the tweezer focused too deep or high above the surface, or not centered on the rail. Lastly, once we do have a working evanescent trap, we have the option of reintroducing the optical tweezer to override a given evanescent lattice sites potential and transport atoms to another site allowing us to deterministically prepare arrangements of atoms about the micro-ring.

7.3 Spin Exchange

Once we have perfected our ability to trap and couple multiple atoms to a resonator, our next major milestone will be the demonstration of spin exchange between two spatially separated atoms coupled to a common mode of a resonator in real time. For this example we will describe the process for the simplest case scenario ignoring propagation phase for exchanged photons, but using tweezers to position atoms it is easily scalable to an arbitrary pair of an ensemble of atoms all coupled to the resonator To begin this experiment we will have to localize two atoms above the ring either via conveyored tweezer lattices or our two color evanescent trapping scheme. Next we will optically pump both atoms into the $|F = 4, mf = 4\rangle$ state via pulsing the repumper ECDL. An initial spin dependent resonance fluorescence imaging scan will be taken via driving the $|F = 4, m_f = 4\rangle \rightarrow |F = 5, m_f = 5\rangle$ transition to verify that we have loaded two atoms prepared in the $|\uparrow\rangle = |F = 4, m_f = 4\rangle$ ground state followed by additional optical pumping.

Next we will have to individually address one of the atoms and prepare it in the $|\downarrow\rangle = |F = 3, m_f = 3\rangle$ ground state. Doing this without perturbing the second atom such that it remains in $|\uparrow\rangle$ will present several challenges due to the atoms close proximity to one another. Driving the mot coils to a peak current of 10A can produce a magnetic field gradient of about 10.6G/cm , for atoms separated by $\sim 30\mu m$ this will result in a differential Zeeman shift, $E_{z,\mathrm{i}} = g_F m_F \mu_B B$ of the F=4 and F=3 ground states at different sites of 77.9kHz. The

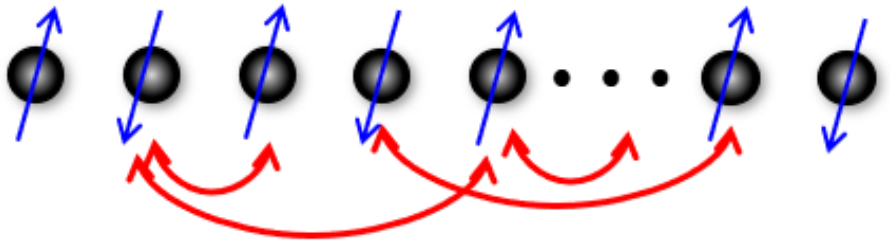

Figure 7.3. Long range spin exchange between arbitrary pairs of atoms coupled to a micro-ring resonator via photon meditated atom-atom interactions. Using a relatively large (1mm) external Raman beam to spatially addressing all atoms coupled to a micro-ring, we can take advantage of the inherent frequency separation of individual tweezer beams from the AOD to spectrally individually address atoms. Using this we can perform PMAAI between any arbitrary pair of atoms connected to a resonator allowing for a rich platform for simulating long range spin models.

differential shift while small is relatively large compared to the linewidth of the 2 photon Raman transition or the microwave magnetic dipole transition from the $F = 4 \rightarrow F - 3$ (< 10 kHz), allowing us to apply a resonant π pulse on one targeted atom.

Alternatively, another way to introduce an effective magnetic field gradient is by modifying the optical tweezer potential. If instead of using perfectly linear polarization, a small circular component is added, the trapping potential (light shift) from the tweezer beam becomes magnetic state dependent[82]

$$U(\vec{r}) = \frac{\pi c^2}{2}\left[\frac{\gamma_2(2 + Pm_f g_f)}{\Delta_2 \omega_2^2} + \frac{\gamma_1(1 - Pm_f g_f)}{\Delta_1 \omega_1^2}\right] I(\vec{r}) \tag{7.8}$$

where g is the Lande' g factor and P represents the dipole beams polarization, P=0 for linearly polarized and $P = \pm 1$ for circularly polarized $\sigma^{\pm}$light. Changing the intensities of the trapping sites will result in a differential shift in the hyperfine ground states, resembling an effective magnetic field gradient[83][49][84]. During which a microwave or Raman π pulse can be used drive the target atom into the F=3 ground state. Following the π pulse transferring atom 1 to the $|\downarrow\rangle$ state, a second fluorescence imaging scan can be taken to ensure

there is one and only one atom in $|\downarrow\rangle$. The polarization can be controlled via introducing a pockels cell in the top tweezer beam beam path before entering the AODs, allowing for rapidly changing form linear to elliptical polarization and back. This method does not require as much space between atoms as the real magnetic field gradient and can scale for more complicated experiments with multiple atoms trapped closer together. In addition, if implementing the AOD tweezer trapping scheme, there is an inherent frequency separation due to the driving tones for each tweezer which can be used to spectrally address individual atoms.

Once prepared in the ground state we can then implement a spin exchange operation $|\downarrow_1\uparrow_2\rangle \rightarrow |\uparrow_1\downarrow_2\rangle$ between the two atoms via use of a single global Raman beam ω_L and the resonator vacuum field g.

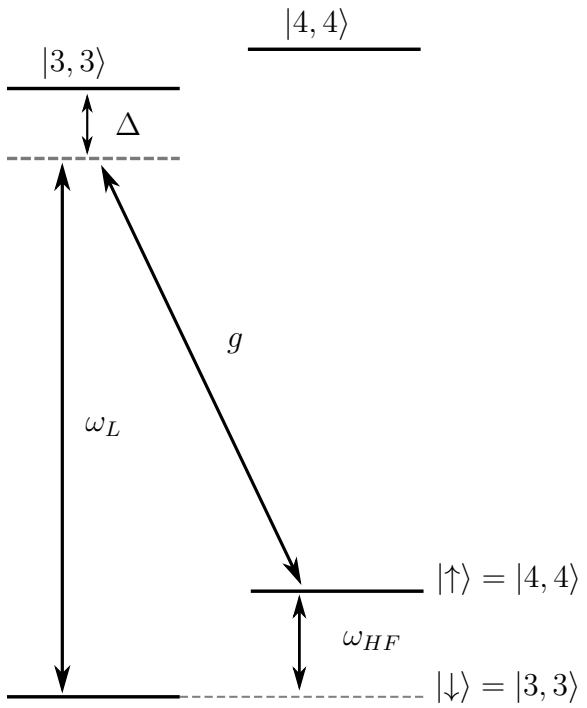

Figure 7.4. Raman scheme for coherent spin exchange operations. $\boldsymbol{\pi}$ polarized Raman beam of frequency ω_L and σ^- cavity mode g drive a coherent Raman resonant (both detuned Δ from excited state $|3,3\rangle$) transition between ground states $|3,3\rangle \leftrightarrow |4,4\rangle$

When the Raman beam is turned on it will address both atoms simultaneously, with the cumulative interaction described by the spin exchange Hamiltonian H_{XY} with interaction strength $J^x_{\mathrm{ij}}y$,

$$H_{XY} = \frac{J^{xy}_{\mathrm{ij}}}{2}\sigma^z_{\mathrm{i}}\sigma^+_{\mathrm{j}} h.c. \tag{7.9}$$

$$J_{\mathrm{i,j}} = \frac{|\Omega|^2 g^2}{2\delta\Delta^2} f(r_{\mathrm{i}}, r_{\mathrm{j}}) \tag{7.10}$$

This interactions describes a four photon process where atom 1 in initial state $|\downarrow\rangle$ undergoes a Raman transition (see chapter 2) flipping spin to state $|\uparrow\rangle$ while emitting a virtual photon into the cavity mode. Atom 2 in initial state $|\uparrow\rangle$ absorbs the virtual cavity photon and emits it into the Raman field completing the reverse process. In the limit that the cavity and Raman laser detuning are both far detuned and 'Raman resonant' ($\Delta_L = \Delta_g = \Delta$) the photonic mode can be adiabatically eliminated. Ω is the Raman laser Rabi rate proportional to the intensity of the beam, and $f(r_{\mathrm{i}}, r_{\mathrm{j}})$ describes the WGM propagation phase in the medium, for a cavity the interactions scale is infinite and it takes the form $f(r_{\mathrm{i}}, r_{\mathrm{j}}) = cos(k_{\mathrm{e}ff} \cdot \delta r)$ where δr is the atom separation along the waveguide path and $k_{\mathrm{e}ff}$ is the effective wave number for D1 light propagating through the resonator. Following the spin exchange interaction we will again perform resonant spin dependent fluorescence allowing us to non-destructively observe spin exchange in real time in situ.

7.4 CNOT Gate

While we are not directly pursuing universal quantum computation, using several of the native operations already developed for our platform will meet many of the required abilities to do so. We can encode a qubit on the hyperfine ground states, again denoting $6^2S_{1/2}\,|F = 4, m_F = 4\rangle$ as $|\uparrow\rangle$ and $6^2S_{1/2}\,|F = 3, m_F = 3\rangle$ as $|\downarrow\rangle$. We have already demon-

Table 7.1. State map for CNOT operation

$\|\Psi_{Input}\rangle$	$R_{2,y}(\pi/2)$	Control Z	$R_{2y}(-\pi/2)$
$\|\uparrow_1\uparrow_2\rangle$	$1/\sqrt{2}\Big(\|\uparrow_1\downarrow_2\rangle + \|\uparrow_1\uparrow_2\rangle\Big)$	$1/\sqrt{2}\Big(\|\uparrow_1\downarrow_2\rangle + \|\uparrow_1\uparrow_2\rangle\Big)$	$\|\uparrow_1\uparrow_2\rangle$
$\|\uparrow_1\downarrow_2\rangle$	$1/\sqrt{2}\Big(\|\uparrow_1\downarrow_2\rangle - \|\uparrow_1\uparrow_2\rangle\Big)$	$1/\sqrt{2}\Big(\|\uparrow_1\downarrow_2\rangle - \|\uparrow_1\uparrow_2\rangle\Big)$	$\|\uparrow_1\downarrow_2\rangle$
$\|\downarrow_1\uparrow_2\rangle$	$1/\sqrt{2}\Big(\|\downarrow_1\downarrow_2\rangle + \|\downarrow_1\uparrow_2\rangle\Big)$	$1/\sqrt{2}\Big(-\|\downarrow_1\downarrow_2\rangle + \|\downarrow_1\uparrow_2\rangle\Big)$	$\|\downarrow_1\downarrow_2\rangle$
$\|\downarrow_1\downarrow_2\rangle$	$1/\sqrt{2}\Big(\|\downarrow_1\downarrow_2\rangle - \|\downarrow_1\uparrow_2\rangle\Big)$	$1/\sqrt{2}\Big(-\|\downarrow_1\downarrow_2\rangle - \|\downarrow_1\uparrow_2\rangle\Big)$	$\|\downarrow_1\uparrow_2\rangle$

strated the means to perform state initialization via optical pumping and state read out using spin dependent florescence imaging. As mentioned before, a universal set of quantum gates can be constructed with only a 2 qubit entangling gate, and arbitrary single qubit rotations.

To implement a 2 qubit entangling CNOT gate we will be implementing a control Z gate acting on both qubit 1 and qubit 2, sandwiched between $\pi/2$ pulses acting only on qubit 2. The action of the control Z gate will be to map $|\downarrow_1\downarrow_2\rangle \rightarrow -|\downarrow_1\downarrow_2\rangle$ and leave all other initial states unchanged except a modulo 2π phase. The net effect of the three pulses is shown in table 7.1, with the end result mapping directly onto the operation of a CNOT gate. To be able to perform this sequence, we will have to demonstrate state initialization, single qubit operations, a two qubit operation, and state detection.

As previously mentioned, for single qubit rotations we can either use microwaves to drive the magnetic dipole transition between $6^2S_{1/2}\,|F=4, m_F=4\rangle$ to $6^2S_{1/2}\,|F=3, m_F=3\rangle$ directly or via coherent Raman pulses where two external beams. We will use either the method of implementing a magnetic field gradient via the MOT coils or an effective magnetic field gradient via introducing a circular polarization into the tweezer beam.

To construct an entangling CNOT gate, once we have arbitrary unitary operations all we need is the ability to perform a control Z gate. To perform this we essentially need an operation that will have the net effect of applying a pi phase shift to the $|\downarrow\downarrow\rangle$ relative to the other 3 possible states of the two pseudo-spin system. To do this we devised a photon-

mediated ZZ interaction for two atoms both interacting with cavity mode with vacuum Rabi frequency g and an external Raman beam ω_L which uniformly addressee both atoms. Considering the case where both Raman beam and the cavity mode will be Raman resonant and detuned Δ from the $|\downarrow\rangle \rightarrow |\mathrm{e}\rangle$ transition, with σ^+ polarization such that ground state $|\uparrow\rangle$ is decoupled.

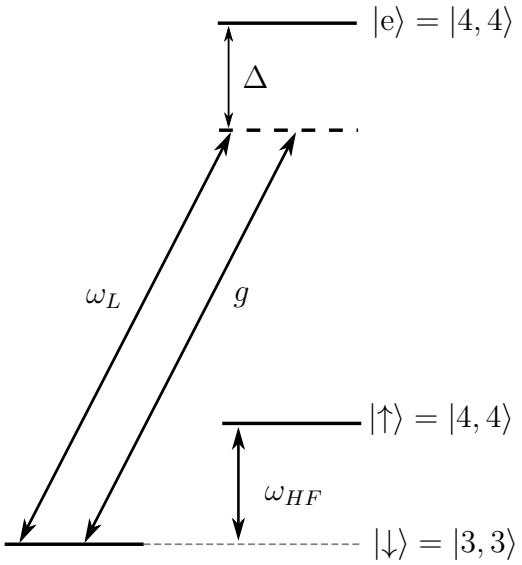

Figure 7.5. Energy Level Diagram for Photon Mediated ZZ interaction. σ^+ polarized Raman beam ω_L and cavity mode g Raman resonantly couple to state $|4,4\rangle$ with common detuning Δ without inducing a spin flip

When the Raman beam is turned on there will be two effects that occur, a light shift (U) due to the off resonant coupling to the $|F = 4, m_f = 4\rangle$ state as will as an interaction between $|\uparrow\rangle \leftrightarrow |\downarrow\rangle$ (V)

$$U = \frac{|\Omega|^2}{4\Delta} \tag{7.11}$$

$$H_{Int}^z = \frac{2|\Omega|^2}{\Delta^2}\frac{|g|^2}{\delta}\cos\left(\vec{k}\cdot\vec{r}\right)\sigma_1^z\sigma_2^z \tag{7.12}$$

Table 7.2. State map for control Z operation

$\|\Psi_{Input}\rangle$	ϕ_U	ϕ_{ZZ}
$\|\uparrow_1\uparrow_2\rangle$	0	0
$\|\uparrow_1\downarrow_2\rangle$	U	-Z
$\|\downarrow_1\uparrow_2\rangle$	U	-Z
$\|\downarrow_1\downarrow_2\rangle$	2U	Z

$$H_{ZZ} = \frac{J^z_{\mathrm{ij}}}{2}\sigma^z_{\mathrm{i}}\sigma^z_{\mathrm{j}} + h.c. \tag{7.13}$$

$$J_{\mathrm{i,j}} = \frac{|\Omega|^2 g^2}{2\delta\Delta^2} f(r_{\mathrm{i}}, r_{\mathrm{j}}) \tag{7.14}$$

where Ω is the Rabi frequency frequency of the Raman laser, Δ is the Raman beam detuning, g is the cavity mode coupling, δ is the cavity detuning from resonance, and $\cos\left(\vec{k}\cdot\vec{r}\right)$ is the phase acquired by the whispering gallery mode traveling distance r inside the cavity. For initial states $|\uparrow_1\downarrow_2\rangle, |\downarrow_1\uparrow_2\rangle$ only one atom is coupled to the Raman beam. H describes a four photon processes where the atom initially in state $|\downarrow\rangle$ may absorb a Raman beam photon, emit a virtual photon into the cavity mode, then perform the reverse process reabsorbing the cavity photon emitting back into the Raman laser field, resulting in a phase denoted $+\phi_V$. For state $|\downarrow_1\downarrow_2\rangle$ an additional process is possible where atom 1(2) absorbs a Raman beam photon and emits a virtual photon into the cavity mode and atom 2(1) performs the reverse process resulting in phase $\phi_V \cos(\vec{k}\cdot\vec{r}) = -\phi_V$ for the case of two atoms separated halfway apart on the resonator. With independent control of Ω, Δ and δ it will be possible to set $\phi_U = \phi_V = n\boldsymbol{\pi}$ where n is an odd integer, resulting in a net phase shift of $\boldsymbol{\pi}$ only for state $|\downarrow_1\downarrow_2\rangle$. In practice I expect this gate to be very challenging to perform as we will have to demonstrate a high degree of control over several degrees of freedom to ensure that the target phases are acquired. We will most likely have to perform Raman sideband cooling to ensure we are in the ground state of motion for sufficient control of the spatial alignment of the atoms on opposite sides of the micro-ring resonator.

7.5 Conclusion

In summary we have made substantial progress in developing an apparatus for interfacing trapped cold cesium atoms with micro-ring resonators. We have developed an optical chip platform with critically coupled micro-ring resonators capable of facilitating modes at multiple cesium resonances. We have demonstrated out ability to trap, cool, and detect atoms withing 5 microns from the surface of our photonic chips as well as the ability to shuttle atoms to and from the surface of the photonic chip. Our trapping scheme has been expanded to trapping arrays of atoms on top of a micro-ring resonator with high probability. We continue to improve and develop more sophisticated trapping schemes and hope to demonstrate atom-cavity coupling in the near future

REFERENCES

[1] FEYNMAN, RICHARD P, "SIMULATING PHYSICS WITH COMPUTERS," *INTERNATIONAL JOURNAL OF THEORETICAL PHYSICS*, vol. 21, no. 6, pp. 467–488, 1982.

[2] LADD THADDEUS D AND JELEZKO FEDOR AND LAFLAMME RAYMOND AND NAKAMURA YASUNOBU AND MONROE CHRISTOPHER AND O'BRIEN JEREMY LLOYD, "QUANTUM COMPUTERS," *NATURE*, vol. 464, no. 7285, p. 45, 2010.

[3] STEANE ANDREW, "QUANTUM COMPUTING," *REPORTS ON PROGRESS IN PHYSICS*, vol. 61, no. 2, p. 117, 1998.

[4] NIELSEN MICHAEL A AND CHUANG ISAAC, *QUANTUM COMPUTATION AND QUANTUM INFORMATION*, 2002.

[5] LADD THADDEUS D AND JELEZKO FEDOR AND LAFLAMME RAYMOND AND NAKAMURA YASUNOBU AND MONROE CHRISTOPHER AND O'BRIEN JEREMY LLOYD, "QUANTUM COMPUTERS," *NATURE*, vol. 464, no. 7285, p. 45, 2010.

[6] LLOYD, SETH AND OTHERS, "UNIVERSAL QUANTUM SIMULATORS," *SCIENCE-NEW YORK THEN WASHINGTON-*, pp. 1073–1077, 1996.

[7] HÄFFNER HARTMUT AND ROOS CHRISTIAN F AND BLATT RAINER, "QUANTUM COMPUTING WITH TRAPPED IONS," *PHYSICS REPORTS*, vol. 469, no. 4, pp. 155–203, 2008.

[8] CIRAC JUAN I AND ZOLLER PETER, "QUANTUM COMPUTATIONS WITH COLD TRAPPED IONS," *PHYSICAL REVIEW LETTERS*, vol. 74, no. 20, p. 4091, 1995.

[9] LOSS DANIEL AND DIVINCENZO DAVID P, "Quantum computation with quantum dots," *PHYSICAL REVIEW A*, vol. 57, no. 1, p. 120, 1998.

[10] LENT CRAIG S AND TOUGAW P DOUGLAS, "A DEVICE ARCHITECTURE FOR COMPUTING WITH QUANTUM DOTS," *PROCEEDINGS OF THE IEEE*, vol. 85, no. 4, pp. 541–557, 1997.

[11] CLARKE JOHN AND WILHELM FRANK K, "SUPERCONDUCTING QUANTUM BITS," *NATURE*, vol. 453, no. 7198, p. 1031, 2008.

[12] YOU JQ AND NORI FRANCO, "SUPERCONDUCTING CIRCUITS AND QUANTUM INFORMATION," *ARXIV PREPRINT QUANT-PH/0601121*, 2006.

[13] DIVINCENZO DAVID P AND OTHERS, "THE PHYSICAL IMPLEMENTATION OF QUANTUM COMPUTATION," *ARXIV PREPRINT QUANT-PH/0002077*, 2000.

[14] WEISS DAVID S AND SAFFMAN MARK, "QUANTUM COMPUTING WITH NEUTRAL ATOMS," *PHYSICS TODAY*, vol. 70, no. 7, p. 44, 2017.

[15] BLOCH IMMANUEL AND DALIBARD JEAN AND NASCIMBENE SYLVAIN, "QUANTUM SIMULATIONS WITH ULTRACOLD QUANTUM GASES," *NATURE PHYSICS*, vol. 8, no. 4, p. 267, 2012.

[16] HOOD JONATHAN D AND GOBAN AKIHISA AND ASENJO-GARCIA ANA AND LU MINGWU AND YU SU-PENG AND CHANG DARRICK E AND KIMBLE HJ, "ATOM–ATOM INTERACTIONS AROUND THE BAND EDGE OF A PHOTONIC CRYSTAL WAVEGUIDE," *PROCEEDINGS OF THE NATIONAL ACADEMY OF SCIENCES*, vol. 113, no. 38, pp. 10 507–10 512, 2016.

[17] HUNG C-L AND GONZÁLEZ-TUDELA ALEJANDRO AND CIRAC J IGNACIO AND KIMBLE HJ, "QUANTUM SPIN DYNAMICS WITH PAIRWISE-TUNABLE, LONG-RANGE INTERACTIONS," *PROCEEDINGS OF THE NATIONAL ACADEMY OF SCIENCES*, vol. 113, no. 34, E4946–E4955, 2016.

[18] THOMPSON JEFFREY DOUGLAS AND TIECKE TG AND DE LEON NATHALIE PULMONES AND FEIST J AND AKIMOV AV AND GULLANS M AND ZIBROV ALEXANDER S AND VULETIĆ V AND LUKIN MIKHAIL D, "COUPLING A SINGLE TRAPPED ATOM TO A NANOSCALE OPTICAL CAVITY," *SCIENCE*, vol. 340, no. 6137, pp. 1202–1205, 2013.

[19] SRINIVASAN KARTIK AND PAINTER OSKAR, "LINEAR AND NONLINEAR OPTICAL SPECTROSCOPY OF A STRONGLY COUPLED MICRODISK–QUANTUM DOT SYSTEM," *NATURE*, vol. 450, no. 7171, p. 862, 2007.

[20] DANIEL JAMES ALTON, "INTERACTING SINGLE ATOMS WITH NANOPHOTONICS FOR CHIP-INTEGRATED QUANTUM NETWORKS," PhD thesis, CALIFORNIA INSTITUTE OF TECHNOLOGY, 2013.

[21] DUAN L-M AND KIMBLE HJ, "SCALABLE PHOTONIC QUANTUM COMPUTATION THROUGH CAVITY-ASSISTED INTERACTIONS," *PHYSICAL REVIEW LETTERS*, vol. 92, no. 12, p. 127 902, 2004.

[22] KIMBLE H JEFF, "THE QUANTUM INTERNET," *NATURE*, vol. 453, no. 7198, p. 1023, 2008.

[23] PEDROTTI FRANK L AND PEDROTTI LENO M AND PEDROTTI LENO S, *INTRODUCTION TO OPTICS*. CAMBRIDGE UNIVERSITY PRESS, 2017.

[24] MATSKO ANDREY B AND ILCHENKO VLADIMIR S, "OPTICAL RESONATORS WITH WHISPERING GALLERY MODES I: BASICS,"

[25] VAHALA KERRY J, "OPTICAL MICROCAVITIES," *NATURE*, vol. 424, no. 6950, p. 839, 2003.

[26] STREKALOV DMITRY V AND MARQUARDT CHRISTOPH AND MATSKO ANDREY B AND SCHWEFEL HARALD GL AND LEUCHS GERD, "NONLINEAR AND QUANTUM OPTICS WITH WHISPERING GALLERY RESONATORS," *JOURNAL OF OPTICS*, vol. 18, no. 12, p. 123 002, 2016.

[27] SAVCHENKOV ANATOLIY A AND MATSKO ANDREY B AND ILCHENKO VLADIMIR S AND MALEKI LUTE, "OPTICAL RESONATORS WITH TEN MILLION FINESSE," *OPTICS EXPRESS*, vol. 15, no. 11, pp. 6768–6773, 2007.

[28] PETER EMMANUELLE AND SENELLART PASCALE AND MARTROU DAVID AND LEMAITRE ARISTIDE AND HOURS J AND GÉRARD JM AND BLOCH JACQUELINE, "EXCITON-PHOTON STRONG-COUPLING REGIME FOR A SINGLE QUANTUM DOT EMBEDDED IN A MICROCAVITY," *PHYSICAL REVIEW LETTERS*, vol. 95, no. 6, p. 067 401, 2005.

[29] KIPPENBERG TOBIAS J AND HOLZWARTH RONALD AND DIDDAMS SCOTT A, "MICRORESONATOR-BASED OPTICAL FREQUENCY COMBS," *SCIENCE*, vol. 332, no. 6029, pp. 555–559, 2011.

[30] VOLLMER FRANK AND ARNOLD STEPHEN, "WHISPERING-GALLERY-MODE BIOSENSING: LABEL-FREE DETECTION DOWN TO SINGLE MOLECULES," *NATURE METHODS*, vol. 5, no. 7, p. 591, 2008.

[31] BRAGINSKY VB AND GORODETSKY ML AND ILCHENKO VS, "QUALITY-FACTOR AND NONLINEAR PROPERTIES OF OPTICAL WHISPERING-GALLERY MODES," *PHYSICS LETTERS A*, vol. 137, no. 7-8, pp. 393–397, 1989.

[32] BOGAERTS WIM AND DE HEYN PETER AND VAN VAERENBERGH THOMAS AND DE VOS KATRIEN AND KUMAR SELVARAJA SHANKAR AND CLAES TOM AND DUMON PIETER AND BIENSTMAN PETER AND VAN THOURHOUT DRIES AND BAETS ROEL, "SILICON MICRORING RESONATORS," *LASER & PHOTONICS REVIEWS*, vol. 6, no. 1, pp. 47–73, 2012.

[33] ELSHAARI ALI W AND ZADEH IMAN ESMAEIL AND JÖNS KLAUS D AND ZWILLER VAL, "THERMO-OPTIC CHARACTERIZATION OF SILICON NITRIDE RESONATORS FOR CRYOGENIC PHOTONIC CIRCUITS," *IEEE PHOTONICS JOURNAL*, vol. 8, no. 3, pp. 1–9, 2016.

[34] SOLOMON GLENN S AND SANTORI CHARLES AND KUHN AXEL, *SINGLE-PHOTON GENERATION AND DETECTION: CHAPTER 13. SINGLE EMITTERS IN ISOLATED QUANTUM SYSTEMS*. ELSEVIER INC. CHAPTERS, 2013, vol. 45.

[35] DANIEL A. STECK, *QUANTUM AND ATOM OPTICS*, REVISION 0.12.0. May 2017, AVAILABLE ONLINE AT HTTP://STECK.US/TEACHING.

[36] FOOT CHRISTOPHER J AND OTHERS, *ATOMIC PHYSICS*. OXFORD UNIVERSITY PRESS, 2005, vol. 7.

[37] METCALF, HAROLD J AND VAN DER STRATEN, PETER, *LASER COOLING AND TRAPPING OF NEUTRAL ATOMS*. WILEY ONLINE LIBRARY, 2007.

[38] LETT PAUL D AND PHILLIPS WILLIAM D AND ROLSTON SL AND TANNER CAROL E AND WATTS RN AND WESTBROOK CI, "OPTICAL MOLASSES," *JOSA B*, vol. 6, no. 11, pp. 2084–2107, 1989.

[39] DALIBARD JEAN AND COHEN-TANNOUDJI CLAUDE, "LASER COOLING BELOW THE DOPPLER LIMIT BY POLARIZATION GRADIENTS: SIMPLE THEORETICAL MODELS," *JOSA B*, vol. 6, no. 11, pp. 2023–2045, 1989.

[40] E. L. Raab, M. Prentiss, A. Cable, S. Chu, and D. E. Pritchard, "TRAPPING OF NEUTRAL SODIUM ATOMS WITH RADIATION PRESSURE," *PHYS. REV. LETT.*, vol. 59, pp. 2631–2634, 23 Dec. 1987. DOI: 10.1103/PhysRevLett.59.2631. [Online]. Available: https://link.aps.org/doi/10.1103/PhysRevLett.59.2631.

[41] ADOLF SMEKAL, "ZUR QUANTENTHEORIE DER DISPERSION," *NATURWISSENSCHAFTEN 11*, pp. 873–875, 1923.

[42] CV RAMAN, "A NEW RADIATION," *INDIAN J. PHYS.*, vol. 2, p. 387, 1927.

[43] GORDON G HAMMES, *SPECTROSCOPY FOR THE BIOLOGICAL SCIENCES*. NY JOHN WILEY & SONS, 2005.

[44] GARDINER D.J, *PRACTICAL RAMAN SPECTROSCOPY*. SPRINGER, 1989.

[45] KERMAN ANDREW J AND VULETIĆ VLADAN AND CHIN CHENG AND CHU STEVEN, "BEYOND OPTICAL MOLASSES: 3D RAMAN SIDEBAND COOLING OF ATOMIC CESIUM TO HIGH PHASE-SPACE DENSITY," *PHYSICAL REVIEW LETTERS*, vol. 84, no. 3, p. 439, 2000.

[46] "PHOTON-MEDIATED INTERACTION BETWEEN TWO DISTANT ATOMS, author=Stefan Rist et al.," *PHYS. REV, A*, vol. 78, p. 013 808, 1 2008.

[47] GONZ'ALEZ-TUDELA A. AND HUNG CL. AND CHANG D. ET AL., "SUBWAVELENGTH VACUUM LATTICES AND ATOM–ATOM INTERACTIONS IN TWO-DIMENSIONAL PHOTONIC CRYSTALS," *NATURE PHOTONICS*, vol. 9, pp. 320–325, 5 2015.

[48] VARUN D. VAIDYA AND BENJAMIN L. LEV AND ET AL., "TUNABLE-RANGE, PHOTON-MEDIATED ATOMIC INTERACTIONS IN MULTIMODE CAVITY QED," *PHYS. REV. X*, vol. 8, p. 011 002, 2018.

[49] ADAM KAUFMAN, "LASER COOLING ATOMS TO INDISTINGUISHABILITY: ATOMIC HONG-OU-MANDEL INTERFERENCE AND ENTANGLEMENT THROUGH SPIN EXCHANGE," PhD thesis, UNIVERSITY OF COLORADO, 2013.

[50] KAZI RAJIBUL ISLAM, "Quantum simulation of interacting spin models with trapped ions," PhD thesis, UNIVERSITY OF MARYLAND, 2012.

[51] MONROE C. AND MEEKHOF D. M. AND KING B. E. AND JEFFERTS S. R. AND ITANO W. M. AND WINELAND D. J. AND GOULD P., "RESOLVED-SIDEBAND RAMAN COOLING OF A BOUND ATOM TO THE 3D ZERO-POINT ENERGY," *PHYS. REV. LETT.*, vol. 75, pp. 4011–4014, 22 Nov. 1995. DOI: 10.1103/PhysRevLett.75.4011. [Online]. Available: https://link.aps.org/doi/10.1103/PhysRevLett.75.4011.

[52] KAUFMAN ADAM M AND LESTER BRIAN J AND REGAL CINDY A, "COOLING A SINGLE ATOM IN AN OPTICAL TWEEZER TO ITS QUANTUM GROUND STATE," *PHYSICAL REVIEW X*, vol. 2, no. 4, p. 041 014, 2012.

[53] A.S. ARNOLD AND J.S. WILSON AND M.G. BOSHIER, "A SIMPLE EXTENDED-CAVITY DIODE LASER," *REVIEW OF SCIENTIFIC INSTRUMENTS*, vol. 69, p. 1236, 1998.

[54] STECK D., "CESIUM D LINE DATA," 2003. [Online]. Available: https://steck.us/alkalidata/cesiumnumbers.pdf.

[55] WIEMAN, C AND HÄNSCH, TH W, "DOPPLER-FREE LASER POLARIZATION SPECTROSCOPY," *PHYSICAL REVIEW LETTERS*, vol. 36, no. 20, p. 1170, 1976.

[56] C. Pearman, C. Adams, S. Cox, P. Griffin, D. Smith, and I. Hughes, "POLARIZATION SPECTROSCOPY OF A CLOSED ATOMIC TRANSITION: APPLICATIONS TO LASER FREQUENCY LOCKING," *JOURNAL OF PHYSICS B: ATOMIC, MOLECULAR AND OPTICAL PHYSICS*, vol. 35, no. 24, p. 5141, 2002.

[57] MCCARRON DJ AND KING SA AND CORNISH SL, "MODULATION TRANSFER SPECTROSCOPY IN ATOMIC RUBIDIUM," *MEASUREMENT SCIENCE AND TECHNOLOGY*, vol. 19, no. 10, p. 105 601, 2008.

[58] A. ASPECT AND E. ARIMONDO AND R. KAISER AND N. VANSTEENKISTE AND C. COHEN-TANNOUDJI, "LASER COOLING BELOW THE ONE-PHOTON RECOIL ENERGY BY VELOCITY-SELECTIVE COHERENT POPULATION TRAPPING," *PHYS. REV LETT.*, vol. 61, p. 826, 1988.

[59] A. ASPECT AND E. ARIMONDO AND R. KAISER AND N. VANSTEENKISTE AND C. COHEN-TANNOUDJI, "LASER COOLING BELOW THE ONE-PHOTON RECOIL ENERGY BY VELOCITY-SELECTIVE COHERENT POPULATION TRAPPING: THEORETICAL ANALYSIS," *J. OPT. SOC. AM. B*, vol. 6, pp. 2112–2124, 1989.

[60] ADU SMITH DAVID AND AIGNER SIMON AND HOFFERBERTH SEBASTIAN AND GRING MICHAEL AND ANDERSSON L MAURITZ AND WILDERMUTH S. AND KRÜGER PETER AND SCHNEIDER STEPHAN AND SCHUMM THORSTEN AND SCHMIEDMAYER JÖRG, "ABSORPTION IMAGING OF ULTRACOLD ATOMS ON ATOM CHIPS," *OPTICS EXPRESS*, vol. 19, pp. 8471–85, Apr. 2011. DOI: 10.1364/OE.19.008471.

[61] ARTHUR EDWARD RUARK AND MELVILLE F. PETERS, "HELMHOLTZ COILS FOR PRODUCING UNIFORM MAGNETIC FIELDS∗," *J. OPT. SOC. AM.*, vol. 13, no. 2, pp. 205–212, Aug. 1926.

[62] WILDERMUTH S. AND KRÜGER P. AND BECKER C. AND BRAJDIC M. AND HAUPT S. AND KASPER A. AND FOLMAN R. AND SCHMIEDMAYER J., "OPTIMIZED MAGNETO-OPTICAL TRAP FOR EXPERIMENTS WITH ULTRACOLD ATOMS NEAR SURFACES," *PHYS. REV. A*, vol. 69, p. 030 901, 3 Mar. 2004. DOI: 10.1103/PhysRevA.69.030901. [Online]. Available: https://link.aps.org/doi/10.1103/PhysRevA.69.030901.

[63] CHANG D. E. AND DOUGLAS J. S. AND GONZÁLEZ-TUDELA A. AND HUNG C.-L. AND KIMBLE H. J., "COLLOQUIUM: QUANTUM MATTER BUILT FROM NANOSCOPIC LATTICES OF ATOMS AND PHOTONS," *REV. MOD. PHYS.*, vol. 90, p. 031 002, 3 Aug. 2018. DOI: 10.1103/RevModPhys.90.031002. [Online]. Available: https://link.aps.org/doi/10.1103/RevModPhys.90.031002.

[64] TIECKE T. AND THOMPSON J. AND DE LEON N. ET AL., "NANOPHOTONIC QUANTUM PHASE SWITCH WITH A SINGLE ATOM," *NATURE*, vol. 508, pp. 241–244, 2014.

[65] CHANG D. E. AND CIRAC J. I. AND KIMBLE H. J., "SELF-ORGANIZATION OF ATOMS ALONG A NANOPHOTONIC WAVEGUIDE," *PHYS. REV. LETT.*, vol. 110, p. 113 606, 11 Mar. 2013. DOI: 10.1103/PhysRevLett.110.113606. [Online]. Available: https://link.aps.org/doi/10.1103/PhysRevLett.110.113606.

[66] SAYRIN CLÉMENT AND JUNGE CHRISTIAN AND MITSCH RUDOLF AND ALBRECHT BERNHARD AND O'SHEA DANNY AND SCHNEEWEISS PHILIPP AND VOLZ JÜRGEN AND RAUSCHENBEUTEL ARNO, "NANOPHOTONIC OPTICAL ISOLATOR CONTROLLED BY THE INTERNAL STATE OF COLD ATOMS," *PHYS. REV. X*, vol. 5, p. 041 036, 4 Dec. 2015. DOI: 10.1103/PhysRevX.5.041036. [Online]. Available: https://link.aps.org/doi/10.1103/PhysRevX.5.041036.

[67] TZU-HAN CHANG AND XINCHAO ZHOU AND MING ZHU AND BRIAN M. FIELDS AND CHEN-LUNG HUNG, "EFFICIENTLY COUPLED MICRORING CIRCUIT FOR ON-CHIP CAVITY QED WITH TRAPPED ATOMS," *APPL. PHYS. LETT.*, vol. 117, p. 174 001, 2020.

[68] CASIMIR H. B. G. AND POLDER D., "THE INFLUENCE OF RETARDATION ON THE LONDON-VAN DER WAALS FORCES," *PHYS. REV.*, vol. 73, pp. 360–372, 4 Feb. 1948. DOI: 10.1103/PhysRev.73.360. [Online]. Available: https://link.aps.org/doi/10.1103/PhysRev.73.360.

[69] VENKATARAM PRASHANTH S. AND MOLESKY SEAN AND CHAO PENGNING AND RODRIGUEZ ALEJANDRO W., "FUNDAMENTAL LIMITS TO ATTRACTIVE AND REPULSIVE CASIMIR-POLDER FORCES," *PHYS. REV. A*, vol. 101, p. 052 115, 5 May 2020. DOI: 10.1103/PhysRevA.101.052115. [Online]. Available: https://link.aps.org/doi/10.1103/PhysRevA.101.052115.

[70] STEHLE C.AND BENDER H. AND ZIMMERMANN C. ET AL., "PLASMONICALLY TAILORED MICROPOTENTIALS FOR ULTRACOLD ATOMS," *NATURE PHOTONICS*, vol. 5, pp. 494–498, 2011.

[71] SCHLOSSER N. AND REYMOND G. AND GRANGIER P., "COLLISIONAL BLOCKADE IN MICROSCOPIC OPTICAL DIPOLE TRAPS," *PHYS. REV. LETT.*, vol. 89, p. 023 005, 2 Jun. 2002. DOI: 10.1103/PhysRevLett.89.023005. [Online]. Available: https://link.aps.org/doi/10.1103/PhysRevLett.89.023005.

[72] SWALLOWS MATTHEW D. AND BISHOF MICHAEL AND LIN YIGE AND BLATT SEBASTIAN AND MARTIN MICHAEL J. AND REY ANA MARIA AND YE, JUN, "SUPPRESSION OF COLLISIONAL SHIFTS IN A STRONGLY INTERACTING LATTICE CLOCK," *SCIENCE*, vol. 331, no. 6020, pp. 1043–1046, 2011.

[73] N P STERN AND D J ALTON AND H J KIMBLE, "SIMULATIONS OF ATOMIC TRAJECTORIES NEAR A DIELECTRIC SURFACE," *IOP PUBLISHING LTD*, vol. 13, p. 085 004, 2011.

[74] KUHR S AND ALT W AND SCHRADER D AND DOTSENKO I AND MIROSHNYCHENKO Y AND ROSENFELD W AND KHUDAVERDYAN M AND GOMER V AND RAUSCHENBEUTEL A AND MESCHEDE D, "COHERENCE PROPERTIES AND QUANTUM STATE TRANSPORTATION IN AN OPTICAL CONVEYOR BELT," *PHYSICAL REVIEW LETTERS*, vol. 91, no. 21, p. 213 002, 2003.

[75] SCHRADER D. AND KUHR S. AND ALT W. ET AL., "AN OPTICAL CONVEYOR BELT FOR SINGLE NEUTRAL ATOMS," *SPRINGER*, vol. 73, pp. 819–824, 2001.

[76] TOMÁŠ ČIŽMÁR, "OPTICAL CONVEYOR BELT FOR DELIVERY OF SUBMICRON OBJECTS," *APPL. PHYS. LETT.*, vol. 86, p. 174 101, 2005.

[77] ARUTE F. AND ARYA K. AND BABBUSH R. ET AL, "QUANTUM SUPREMACY USING A PROGRAMMABLE SUPERCONDUCTING PROCESSOR," *NATURE*, vol. 574, pp. 505–510, 2019.

[78] LANDSMAN K. A. AND WU Y. AND LEUNG P. H. AND ZHU D. AND LINKE N. M. AND BROWN K. R. AND DUAN L. AND MONROE C., "TWO-QUBIT ENTANGLING GATES WITHIN ARBITRARILY LONG CHAINS OF TRAPPED IONS," *PHYS. REV. A*, vol. 100, p. 022 332, 2 Aug. 2019. DOI: 10.1103/PhysRevA.100.022332. [Online]. Available: https://link.aps.org/doi/10.1103/PhysRevA.100.022332.

[79] POPKIN GABRIEL, "QUEST FOR QUBITS," *SCIENCE*, vol. 354, no. 6316, pp. 1090–1093, 2016, ISSN: 0036-8075. DOI: 10.1126/science.354.6316.1090. eprint: https://science.sciencemag.org/content/354/6316/1090.full.pdf. [Online]. Available: https://science.sciencemag.org/content/354/6316/1090.

[80] ENDRES MANUEL AND BERNIEN HANNES AND KEESLING ALEXANDER AND LEVINE HARRY AND ANSCHUETZ ERIC R. AND KRAJENBRINK ALEXANDRE AND SENKO CRYSTAL AND VULETIC VLADAN AND GREINER MARKUS AND LUKIN MIKHAIL D., "ATOM-BY-ATOM ASSEMBLY OF DEFECT-FREE ONE-DIMENSIONAL COLD ATOM ARRAYS," *SCIENCE*, vol. 354, no. 6315, pp. 1024–1027, 2016.

[81] CRAIN S. AND CAHALL C. AND VRIJSEN G. ET AL., "HIGH-SPEED LOW-CROSSTALK DETECTION OF A 171YB+ QUBIT USING SUPERCONDUCTING NANOWIRE SINGLE PHOTON DETECTORS," *COMMUNICATIONS PHYSICS*, vol. 2, no. 97, 2019.

[82] GRIMM RUDOLF AND WEIDEMÜLLER MATTHIAS AND OVCHINNIKOV YURII B, "OPTICAL DIPOLE TRAPS FOR NEUTRAL ATOMS," in *ADVANCES IN ATOMIC, MOLECULAR, AND OPTICAL PHYSICS*, vol. 42, ELSEVIER, 2000, pp. 95–170.

[83] WEITENBERG CHRISTOF AND ENDRES MANUEL AND SHERSON JACOB F AND CHENEAU MARC AND SCHAUß PETER AND FUKUHARA TAKESHI AND BLOCH IMMANUEL AND KUHR STEFAN, "SINGLE-SPIN ADDRESSING IN AN ATOMIC MOTT INSULATOR," *NATURE*, vol. 471, no. 7338, p. 319, 2011.

[84] KAUFMAN AM AND LESTER BJ AND REYNOLDS CM AND WALL ML AND FOSS-FEI, M AND HAZZARD KRA AND REY AM AND REGAL CA, "TWO-PARTICLE QUANTUM INTERFERENCE IN TUNNEL-COUPLED OPTICAL TWEEZERS," *SCIENCE*, vol. 345, no. 6194, pp. 306–309, 2014.